INCORPORATION, DECONTAMINATION PERFORMANCE, AND MATERIAL PROPERTIES OF MOLECULAR POLYOXOMETALATES IN BREATHABLE FIBROUS SUBSTRATES

A Dissertation

Presented to the Faculty of the Graduate School

of Cornell University

In Partial Fulfillment of the Requirements for the

Doctor of Philosophy

by

Nancy Elizabeth Allen

August 2016

INCORPORATION, DECONTAMINATION PERFORMANCE, AND MATERIAL PROPERTIES OF MOLECULAR POLYOXOMETALATES IN BREATHABLE FIBROUS SUBSTRATES

Nancy Elizabeth Allen, Ph.D.

Cornell University 2016

Combining unique fiber morphologies with new self-decontamination technologies can enhance chemical warfare agent and toxin degradation on fibrous substrates. In order for these substrates to be used in chemical protective apparel for defense or agricultural applications, their decontamination performance, breathability, mechanical properties, and laundry durability must be considered. This work investigates these properties in an attempt to further the progress in developing materials that can balance protection with comfort and durability.

First, co-continuous electrospinning was used to fabricate nanofibrous cellulose acetate membranes with unique, grooved fiber morphology due to the selective dissolution of polyethylene oxide. The grooved cellulose acetate membranes were deacetylated to form grooved cellulose membranes. A self-decontaminating Keggin-type polyoxometalate (POM) ($H_5PV_2Mo_{10}O_{40}$) was synthesized and characterized. The catalytic molecular polyoxometalates (POMs) were used to functionalize the grooved nanofibrous membranes as well as non-grooved nanofibrous membranes, 100% cotton, 55/45 cotton/polyester

fabrics, and Tencel® peachskin fabric via two different methodologies – referred to herein as "POM-grafting" and "POM-immobilization". The percent POM add-on of each substrate was measured via thermal gravimetric analysis and related to the substrate properties, morphology, and functionalization method. The POM-treated substrates were exposed to methyl parathion, a simulant of the chemical warfare agent (CWA) VX, to evaluate the decontamination performance. The degradation of methyl parathion by the POM treated substrates was measured using high performance liquid chromatography, and the degradation performance of the substrates was compared and related to their properties, morphology, and functionalization method. Properties such as mechanical strength, porosity, and water vapor permeability were examined for the fibrous substrates, and the laundry durability of the cotton substrates was evaluated.

These experiments revealed that no significant differences in POM loading or decontamination performance were seen between the two POM functionalization techniques. Characterization of the functionalized substrates indicates some possible explanations of POM functionalization, although the exact mechanisms remain to be clarified. Relative to the non-grooved fibers, the creation of the grooved fiber morphology resulted in a significantly larger surface area for which POMs to bind, and the amount of methyl parathion degradation over time was significantly enhanced. The POM-functionalized grooved nanofibrous cellulose acetate and cellulose membranes resulted in the highest amount of self-decontamination of methyl parathion compared to the other substrates owing to increased amount of POM loading as a result of increased surface area. Although their tensile strength was poor, grooved fibers had the smallest mean pore diameter and achieved the highest water vapor permeability compared to the other fibrous

substrates. No significant difference in the laundry durability of the two POM functionalization methods was found.

In order to assess the scale-ability and comfort of POM-treated substrates in simulated end-use conditions, the POM-immobilized 55/45 cotton/polyester and 100% cotton substrates were scaled up and prototypes of protective coveralls were constructed using these materials and tested on the sweating fabric manikin-Walter™. The scaled materials were characterized via Fourier transform infrared spectroscopy, thermal gravimetric analysis, mechanical strength, and water vapor permeability. The thermal insulation and evaporative resistance properties measured by the sweating manikin were compared to scaled non-POM treated analogous coveralls. Results indicate that the POM functionalization of the substrates had no significant impact on the thermal insulation and minimal impact on evaporative resistance. This work contributes to the use of novel fiber morphologies in breathable chemical protective apparel to achieve better CWA and pesticide decontamination, protection, comfort, and durability.

BIOGRAPHICAL SKETCH

Nancy Elizabeth Allen has been a Fiber Science graduate student at Cornell University (Ithaca, NY) since 2010 studying with Dr. S. K. Obendorf for her masters and Dr. Jintu Fan for her Ph.D. She has studied her minor concentrations of Chemistry and Apparel Design, with the guidance of Dr. Geoffrey Coates, Dr. Susan Ashdown, and Dr. Huiju Park.

Originally from Charleston, South Carolina, she received her Bachelor of Science degree in Polymer Fiber Chemistry at Clemson University (Clemson, SC) in 2007 and worked three years as a development chemist on the Performance Colorants & Additives team for Milliken Chemical (Spartanburg, SC). Some of her favorite past work includes research on corrosion resistant materials for the recently excavated C.S.S. Hunley, the development of chemiluminescent markers for Crayola®, and the reduction of hard-thread waste for a weaving mill in Hartwell, Georgia. She has been an active member of the American Association of Textile Chemists and Colorists since 2003 and helped to re-establish the Cornell Student Chapter in 2014. Her experiences at home, in the lab, outdoors, and as an avid participant in sports and ballet have taught her first-hand the importance of innovation, design, quality, comfort, and durability of performance materials in everyday life. She is passionate about using that knowledge to understand problems across many disciplines and develop technologies that better serve real-world needs. Her research interests include textile manufacturing, textile chemistry, color science, consumer products, thermal comfort, performance clothing, protective apparel, and functional design.

To William and Henry, for the time I have missed in watching you grow up.

To Tom, for love and big fish.

To Phil and Kate, for inspiring me to do this.

To Chance and Imogene Louise, for making Ithaca a little bit warmer.

To Ms. Renkas and Dr. Diehl, for teaching me the scientific method.

ACKNOWLEDGEMENTS

First and foremost, I want to thank Dr. Jintu Fan, my doctoral advisor, and Dr. S. Kay Obendorf, my master's advisor, for their efforts in the development of this research, their patience, and their valued guidance and expertise. I am also grateful to Dr. Huiju Park, Dr. Geoffrey Coates, Dr. Susan Ashdown, Dr. C.C. Chu, and Dr. Ruya Ozer, for their contributions to my research and dissertation. Special thanks is extended to Dr. Xia (Sam) Zeng for his years of help with Fourier transform infrared spectroscopy, high performance liquid chromatography, thermal analysis techniques, and the Instron. For their assistance with x-ray diffraction, scanning electron microscopy, and energy dispersive spectroscopy, I would like to thank Maura Weathers, Don Werder, John Hunt, and the CCMR staff of Cornell University. Thank you also, to Dr. Gang Sun of the University of California, Davis for providing the N-halamine treated and non-treated 55/45 cotton/polyester substrates used in decontamination experiments and scaled coverall testing, and Jesse Ruoff and Jiangxia Qin for their help in sewing the coveralls. Thank you to Porous Materials, Inc. (PMI) in Ithaca, NY, who conducted the Brunauer, Emmet, Teller (BET) molecular krypton gas adsorption surface area measurements which were critical to the success of this research. Thank you to the staff at PMI for your help in sample preparation, testing and analysis.

I have been privileged to share in the ideas, insight, and support of my colleagues in Fiber Science as well as Apparel Design, particularly: Dr. Laurie Lange, Dr. Dong Jin Woo, Minji Kim, Paul Soldate, Dr. Yuen Shing (John) Wu, Robert (Sandy) Flint, Dr. Kausik Bal, Thomas Ellingham, Soshana Smith, Marion Schelling, Yingying Wu, Dr. Kristen Morris, Jackie Morreale, and Lauren Goodnow. You all have been invaluable to

me throughout my time at Cornell. I also want to thank Karen Steffy, Judy Wiiki, Michele Draiss, and Tim Snyder in the FSAD Main Office for always being so friendly and helpful. I always look forward to seeing you!

This dissertation research was funded through grants from the North Central Regional Research Project NC 170 federal formula funds, the Cornell University Agricultural Experiment Station (CUAES), the USDA National Institute of Food and Agriculture, HATCH project number NYC-329859 (accession number 1000190, multistate number NC-170], the U.S. Department of Agriculture, the American Association of Textile Chemists and Colorists, the Department of Fiber Science & Apparel Design, and the College of Human Ecology at Cornell University. This work made use of the Cornell Center for Materials Research Shared Facilities, which are supported through the NSF MRSEC program (DMR-1120296).

The completion of this research also owes many thanks to my family and friends in South Carolina, Texas, Virginia, and Indiana for continued love, support, and patience while I have pursued my graduate career further away than y'all preferred and to those of you who bore the long drive and the cold to come pay us a visit. To the Episcopal Church of Cornell and to the friends I have made in Ithaca, thank you for offering compassion, spiritual nourishment, and fellowship that has greatly enriched this experience; I have learned so much from you. Lastly, I want to acknowledge Thomas Daniel, who has made many sacrifices to help me reach this point, - thank you for staying in Ithaca for five additional winters. Thank you for assuring me in moments of self-doubt; your faith in my ability to persevere has helped me overcome challenges in this process that seemed

insurmountable. Thank you for helping me every day to do meaningful work and for enabling me to pursue this opportunity that has meant so much.

TABLE OF CONTENTS

CHAPTER 1

INTRODUCTION

1.1 Protective Materials Background

Ongoing global conflicts and the use of chemical weapons require the advancement of personal protective apparel. Developing technologies in protective apparel aim to reduce exposure to chemical warfare agents (CWAs) in liquid, vaporous, or particulate forms while maintaining personnel thermal comfort, breathability, and human performance. Microfibrous and nanofibrous functionalized, self-decontaminating membranes with engineered pore structures can be applied to protective apparel to prevent CWA penetration while allowing moisture vapor to be transported through the garment. Current garments that protect against CWAs such as distilled mustard, lewisite, tabun, sarin, soman, and *O*-ethyl *S*-[2-(diisopropylamino) ethyl] methylphosphonothioate, a highly toxic nerve agent commonly known as VX, are mostly composed of bulky impermeable barrier materials that do not allow chemicals to penetrate through the garment, nor do they allow moisture, mainly in the form of perspiration, to escape [1]. As a result, these suits lack provisions for thermal comfort in extreme hot and cold environments and cannot be worn for extended periods of time. Their bulkiness reduces dexterity and functionality. After CWA exposure, current military suits that employ activated carbon must be decontaminated before doffing, and they are disposed of as hazardous waste to prevent further contamination. A breathable, self-decontaminating material would improve the functionality, performance, re-usability, and disposal of chemical protective garments.

1.2 Literature Review

1.2.1. Polyoxometalate Structure and Reactivity

Polyoxometalates (POMs) are heteropolyanions, otherwise known as polymeric oxoanions, formed by the condensation of more than two different oxoanions. With a wide range of possible three-dimensional structures, POMs are most commonly composed of MO_6 octahedra with a terminal oxo group and five bridging oxo groups or two terminal oxo groups and four bridging oxo groups. The most widely tested type of POMs are known as Keggin heteropolyanions. These negatively charged nanoclusters of oxide and transition metal ions in their highest oxidation state have the general formula of $X^{n+}(M_{12}O_{40})^{(8-n)}$. The heteroatom X^{n+} can be a wide variety of d-block elements (transition metals) or p-block elements such as Si^{4+} or P^{5+}, and M can be tungsten, molybdenum, vanadium and other metals referred to as addenda ions [2–4]. The substitution of one or more of the addenda ions with another transition metal in the structure creates a mixed addenda POM. Mixed addenda POMs containing vanadium are known to be the most reactive [4,5]. In self-cleaning applications, it is thought that the metal addenda ion(s) (M) act as the self-decontaminating components of the POM, while the X^{n+} (phosphorus, silicon, aluminum, boron, cobalt, zinc, or iron) provides structural integrity [6]. The oxoanions molybdenum (Mo), tungsten (W), vanadium (V), niobium (Nb), and tantalum (Ta) are present as acidic elements in aqueous solutions and polymerize to form polyanions at low pH. In their free acid form, polyoxometalates are referred to as heteropoly or isopoly acids. POM free acids and their salts act as strong acids and have been widely used as acid catalysts and oxidation catalysts that yield better oxidation performance than hydrogen peroxide, ozone, and molecular oxygen when environmental profiles and

efficiency of oxidation are taken into consideration [3]. Vanadates, niobates, tantalates, molybdates, tungstates, and mixed addenda heteropolyanions make up the different classes of polyoxometalates. Mixed addenda polyanions can include molybdovanadates, tungstovanadates, niobotungstates, and molybdotungstates [2].

The majority of polyanions with tetrahedrally-coordinated heteroatoms have structures based on the Keggin anion [2]. Among the many Keggin isomers, there are two main anion isomers classified as α- and β-$XM_{12}O_{40}$. The α-Keggin structure (α-$[XM_{12}O_{40}]^{n-}$) has overall symmetry and is based on a central XO_4 tetrahedron surrounded by twelve MO_6 octahedra arranged in four groups of three edge-shared octahedral, M_3O_{13} [2,7]. One of the most heavily researched mixed addenda POMs, $PMo_{10}V_2O_{40}^{5-}$ is a disubstituted α-Keggin complex with five distinct isomers [4]. Figures 1 and 2 display the particular structure of $H_5PV_2Mo_{10}O_{40}$ [2,8,9]. $H_5PV_2Mo_{10}O_{40}$ is used commonly in homogeneous catalytic oxidation processes since the vanadium acts as the most strongly oxidizing addenda element [4].

Literature suggests that substrate oxidation can occur via one of five possible homogeneous modes. The process of the first and most common mode begins with the direct oxidation of a substrate by the polyoxometalate. The reduced POM is then re-oxidized to its original state by a terminal oxidant in the system as seen in Scheme 1 [4,5,10–15]. This mode applies to the POM $H_5PV_2Mo_{10}O_{40}$ when oxidizing substrates such as aromatic and alkyl aromatic compounds in the liquid homogeneous phase via electron and oxygen transfer in what is known as a Mars-van Krevelen reaction. For example, cyclic dienes, alcohols, amines, and phenols undergo oxidative dehydrogenation, meaning there is an electron and proton transfer from the substrate P-H_2, to the

polyoxometalate [5]. It is important to note that the substrates are not oxygenated, implying there is no oxygen transfer from the metal oxide [5]. Figure 3 represents the rapid, reversible redox changes that classify these nanoparticles as catalytic and self-regenerating [5,10,15]. If the POM undergoes the second homogeneous mode of catalytic oxidation, then the POM can act as a co-catalyst comparable to the path of a Wacker reaction, where terminal alkene substrates are oxidized to form a ketone using a palladium catalyst, a co-catalyst, and water. Expected products of this reaction mechanism would be carbonyls depending on the type of electron-poor alkene substrate. [13,14,16]. In mode three, the POM acts to oxygenate the substrate meaning the POM is catalyzing an oxo transfer oxidation [13,17]. In mode 4, the POM acts as a photocatalyst, meaning that when the POM is in its excited state, it is able to directly oxidize the substrate while enabling the reoxidation of the reduced complex. The last of the possible five modes of substrate oxidation suggests that the cation of the POM oxidizes the substrate directly. The third, fourth, and fifth modes are thought to be less common paths of substrate oxidation [12,13].

In the first mode, literature suggests that the presence of water may play a significant role in POM catalytic oxidation in non-aqueous or non-polar environments. This effect was observed when the POM $H_5PV_2Mo_{10}O_{40}$ was used to oxidize CWA mustard analogs. Due to the rapid capture of thioether radicals by water, the kinetic rate of catalytic oxidation was increased as the amount of water content was increased. While further investigation of this phenomenon is required, these findings suggest that it may be preferable to use $H_5PV_2Mo_{10}O_{40}$ in its hydrated form in order to achieve greater catalytic oxidation of chemical warfare agents and their simulants [13]. It is important to note that

when using this hydrated POM via mode one catalysis, only the vanadiums (not the molybdenums) are reduced when the POM oxidizes a substrate [13].

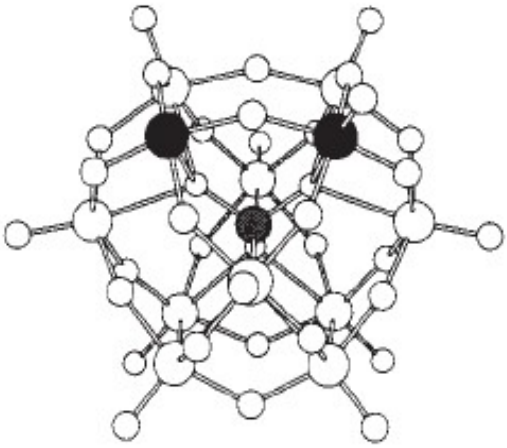

Figure 1: Structure of $H_5PV_2Mo_{10}O_{40}$ with the central phosphorous heteroatom shaded grey and the two vanadium atoms shaded black [8]

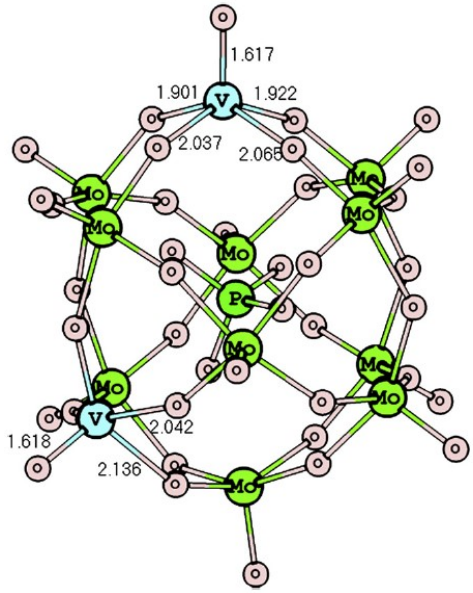

Figure 2: PM6 optimal geometry of Keggin unit containing two vanadium atoms [9]

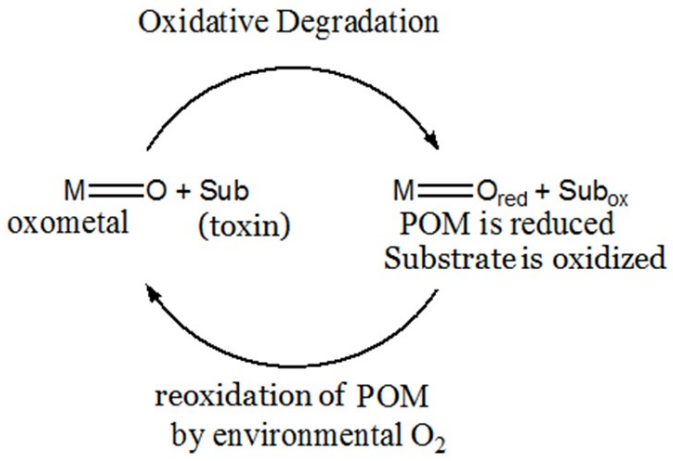

Figure 3: Catalytic cycle of polyoxometalate nanoparticles where the oxidative degradation occurs via the first mode of substrate oxidation [4,14,15]

Scheme 1: The oxidative dehydrogenation of aromatic and alkyl aromatic substrates [5]

$$P\text{-}H_2 + POM_{ox} \longrightarrow P + 2H^+ + POM_{red}$$

$$2H^+ + POM_{red} + 1/2O_2 \longrightarrow POM_{ox} + H_2O$$

A second mechanism of POM degradation is hydrolysis. POMs such as $H_5PV_2Mo_{10}O_{40}$ have strong Brønsted acid strength, akin to that of sulfuric acid. In the presence of water, the protons of the POM can disassociate more readily and become free to interact with the P-O linkage of the organophosphate methyl parathion (O, O-dimethyl O-p-nitrophenyl phosphorothioate), a simulant of CWA VX, [18–20]. This leads to the

cleavage of the aryl ester P-O linkage via nucleophilic displacement at the phosphorus thus resulting in the degradation of methyl parathion into diethylthiophosphate and p-nitrophenol as seen in Scheme 2 [18,21,22]. In an anaerobic environment, the hydrolysis of methyl parathion proceeds as shown in Scheme 3 where the nitro group on the methyl parathion is reduced to an amine [21].

Scheme 2: Hydrolysis of methyl parathion in aerobic conditions [18,21,22]

$$(C_2H_5O)_2P(S)OC_6H_4NO_2 + H_2O \rightarrow HOC_6H_4NO_2 + (C_2H_5O)_2P(S)OH$$

Scheme 3: Hydrolysis of methyl parathion in anaerobic conditions [21]

$$(C_2H_5O)_2P(S)OC_6H_4NO_2 + 6\ H \rightarrow (C_2H_5O)_2P(S)OC_6H_4NH_2 + 2\ H_2O$$

The exact degradation pathways of methyl parathion when exposed to the POM $H_5PV_2Mo_{10}O_{40}$ require further investigation. Both catalytic oxidation and hydrolysis may play a role. Scheme 4 illustrates several possible degradation pathways of methyl parathion with varied mechanisms when the VX simulant is exposed to TiO_2. [23]. In this example, TiO_2 acts as a photocatalyst and requires UV light to degrade the toxin. Unlike this mechanism, POMs require no UV light to degrade methyl parathion. As seen in Scheme 4, the main products that result from TiO_2 degradation of methyl parathion are methyl paraoxon, O,O,O-trimethyl phosphoric thiourate, and p-nitrophenol [23].

Scheme 4: Possible degradation pathway of methyl parathion in coated TiO_2 [23]

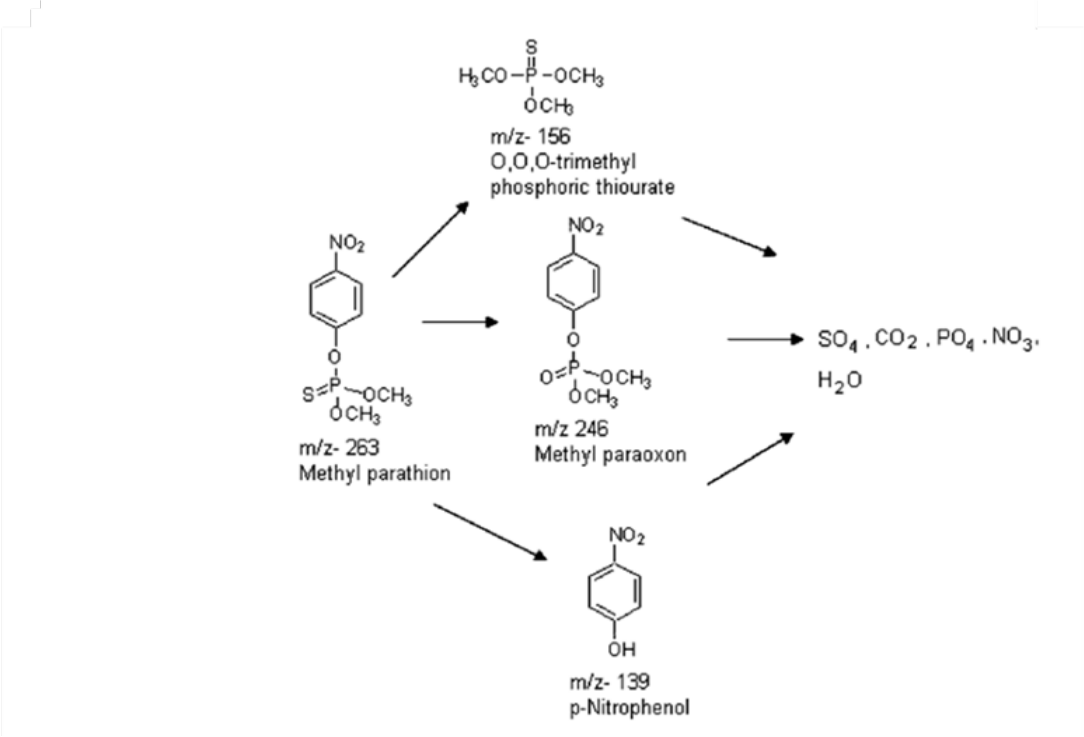

While further examination of degradation mechanisms and degradation products is needed, it has been shown that both in the liquid and gas homogeneous phases, as well as when grafted to the surface of fabrics such as polyacrylic, nylon, cotton, other cellulosic fibers, polyester, polyacrylonitrile, polyvinylidene, polyolefin, polyurethane, polytetrafluoroethylene, carbon cloth, other carbon-based fabrics such as electrospun Estane® microfibers, and combinations thereof, POMs can decontaminate volatile organics and chemical warfare agents such as the thioether mustard analog (HD), the CWA simulant 2-chloroethylethyl sulfide (CEES), and other compounds of varying toxicity [8,13,15,24–

29]. However, no literature has shown definitively that $H_5PV_2Mo_{10}O_{40}$ can degrade an organophosphate such as VX.

1.2.2. POM Functionalized Microporous Fibrous Substrates

POMs have been incorporated into electrospun, microporous, nanofibrous cellulose acetate membranes in order to increase the number of active POM binding sites on fibers. This increase in surface area has enabled increased catalytic decontamination of volatile organics such as acetaldehyde and 1-propanethiol and CWAs such as sulfur mustard due to the large fiber surface area [25,26,28]. The objective of this project includes understanding how to fabricate high surface area cellulose membrane substrates, their characterization, POM synthesis, two different POM-substrate functionalization methods, and the characterization of the POM functionalized substrates.

1.2.3. Fabrication & Characterization of High Surface Area Cellulose Membranes

In order to electrospin, a polymer solution must be agitated at room temperature until full dissolution is achieved. The polymer solution is poured into an electrospinning reservoir. A stainless steel electrode is then placed in the solution and connected to a power supply with a grounded counter electrode connected to an aluminum foil fiber collection plate that can be placed at a specified distance from the electrode. Once the electrode reaches critical voltage, electrostatic forces overcome the surface tension of the solution, and a jet is ejected and accelerated to the upper aluminum foil collection plate due to the electric field generated between the electrode and counter electrode. The jet splits into fiber filaments due to electrostatic instability forming interconnected fibrous membranes. These filaments solidify once the solvent evaporates and can be removed from the aluminum collector and dried under vacuum. [30].

The pore size, pore size distribution, adsorption, penetration, fiber size, fiber morphology, and surface area of these membranes can be measured using a porometer, a scanning electron microscope (SEM), and a gas adsorption technique known as Brunauer–Emmett–Teller (BET). This technique measures the physical adsorption of gas molecules on a solid surface in order to analyze the surface area of a material. The measurement of additional mechanical and thermal properties also helps to characterize the composition of the membranes. Dixit, Tewari, and Obendorf demonstrated that electrospun regenerated cellulose nanofiber membranes can be loaded with self-decontaminating compounds, such as saponin, which show good performance in degrading biological agents with potential applications in protective apparel [31].

1.2.4 Co-continuous Polymer Structures

Woo and Obendorf, used co-continuous electrospun fibers to exhibit that fiber morphology can influence the diffusion of chemical warfare agents and other toxins in order to improve self-decontamination technologies on fiber substrates. Woo showed that fibers that are monoaxially spun with active self-decontaminating compounds can limit the efficiency of decontamination [32]. This is a result of the compounds being contained within the fiber and unavailable to surface reactions that would enhance toxin degradation [33]. Co-continuous electrospinning is a process that employs phase separation of a solution to spin a blend of polymers. An interconnected, microporous structure with deep pores, grooves, and channels in the fiber is created by selective dissolution, where one of the polymers is removed from the co-continuous blend post-electrospinning [34]. These pores, grooves, and channels provide more surface area on the fibers for which a decontaminating agent, such as POMs, can bind and enhance the surface reaction

efficiency of the fibers [34–36]. Tang and his colleagues (2008) showed how acetone could be used to selectively dissolve cellulose acetate from a cellulose acetate / polyurethane co-continuously spun polymer fiber blend in order to create a porous polyurethane fiber.

Following Tang's example, Woo and Obendorf, 2014, blended two polymers (cellulose acetate and polyethylene oxide) in a specific ratio of two solvents (acetone and acetonitrile) and then used this uniform dispersion to co-continuously electrospin a high surface area nanochannelled fibrous cellulosic membrane. The solubility parameters of the polymers were critical to achieving this unique fiber morphology since optimal co-continuous phase formation occurs when the polymer solution is near the interface between a 1-phase-system and 2-phase-system as represented by the solid line in the solubility diagram (Figure 6). Cellulose acetate was chosen as a polymer since it is soluble in both acetone and acetonitrile, and polyethylene oxide was chosen because it is only partially soluble in acetone and fully soluble in water. Partial solubility of polyethylene oxide in acetone was desired to achieve optimal phase formation, and full solubility of polyethylene oxide in water enabled the polymer to be extracted from the co-continuous polymer blend matrix via hot water dissolution. After testing several formulations of these four components, Woo achieved optimal nanochannels and high surface area fibers by electrospinning a solution composed of 15% dual component polymer (60% cellulose acetate [CA], 40% polyethylene oxide [PEO]) and 85% dual component solvent (60% acetonitrile, 40% acetone) and then performing a hot water Soxhlet extraction on the fibers for several hours. The condensed boiling water extracted the polyethylene oxide from the fibers. After extraction, the fibers were vacuum dried. The resulting fibers were

composed of cellulose acetate with grooves or channels created where the polyethylene oxide was originally present. A schematic of this process can be seen in Figure 4, and an SEM of the resulting fiber is shown in Figure 5. This blend is shown on a solubility diagram (Figure 6) which Woo used to determine the optimal solubility for achieving this unique channeled co-continuous fiber morphology.

Figure 4: Co-continuous fiber formation using cellulose acetate (CA) and polyethylene oxide (PEO)

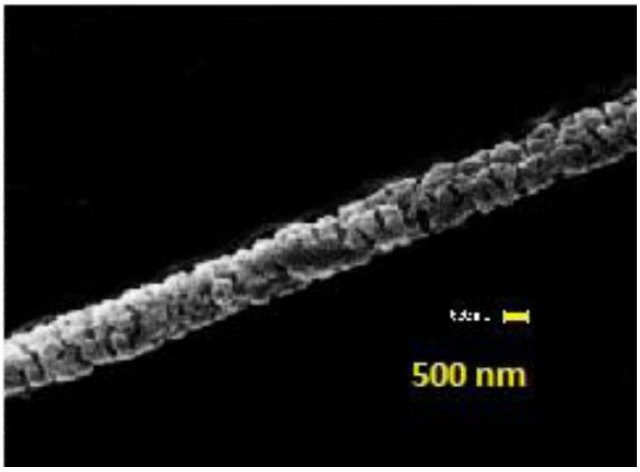

Figure 5: SEM of nanochannelled cellulose acetate / PEO fiber morphology [32]

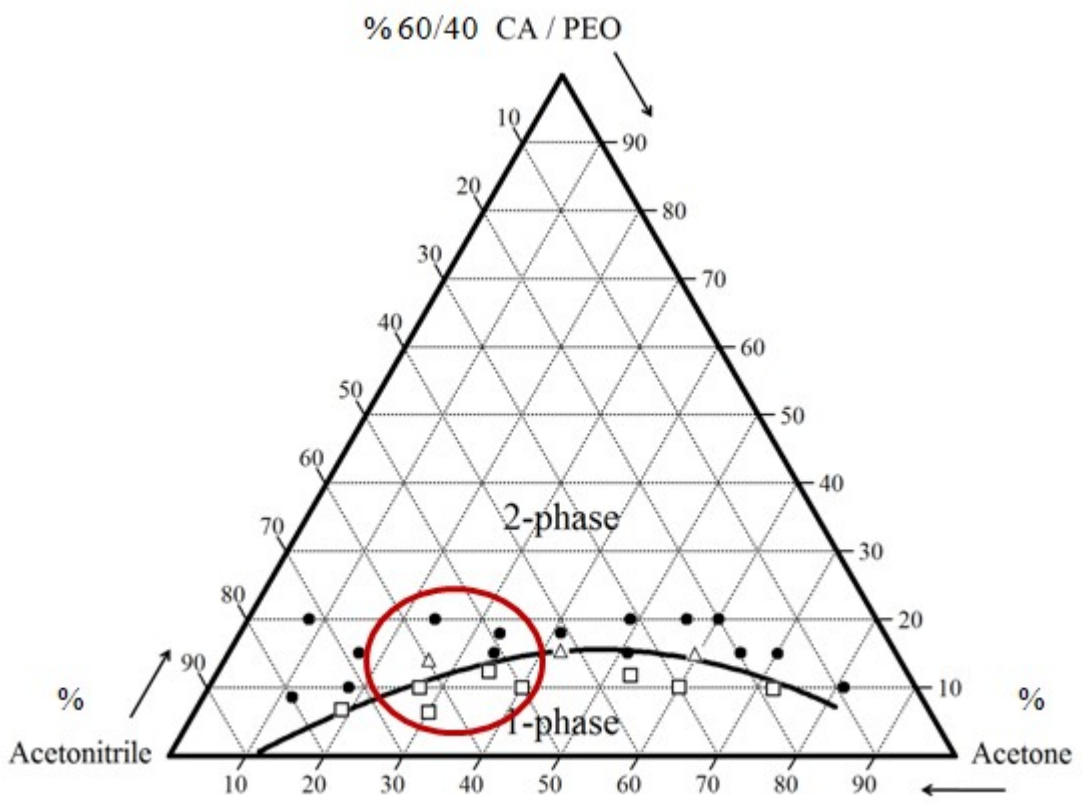

Figure 6: Solubility Diagram of Cellulose Acetate / Polyethylene Oxide blends in Acetone and Acetonitrile. Solid dots, non-shaded squares, and non-shaded triangles represent electrospun fibers prepared by Woo at varying concentrations of polymer and solvent blends. [32]

1.2.5. Solubility Parameters

It is necessary to examine the dissolution properties of the dual polymer / dual solvent electrospinning solution more closely in order to understand the unique fiber morphology this formulation creates. While cellulose acetate is soluble due to its polarity (acetyl content = 39.8%, degree of substitution = 2.45) in both acetone and acetonitrile, polyethylene oxide, which is less polar than cellulose acetate, is not fully soluble in either solvent at ambient conditions [37]. At temperatures above 40°C, polyethylene oxide becomes more soluble in acetone. Neither solvent has a high hydrogen bonding strength.

Additional information regarding the physical properties and solubility of the polymers and solvents can be found in Tables 1 and 2 in Section 2.3.2.3. When combined at certain ratios, the partially immiscible polymer mixture forms a uniform dispersion in the dual component (60/40 acetonitrile to acetone) solvent only after being agitated at high speeds for 1-8 h in a 40°C warm water bath. After electrospinning, one of the polymers can be extracted successfully due to its original partial immiscibility leaving behind a co-continuous fiber composed of the polymer that was not extracted. The partial immiscibility of polyethylene oxide in acetone and acetonitrile due to the lower polarity of PEO is advantageous in the creation of a co-continuous fiber morphology. It enables polyethylene oxide to be extracted after electrospinning leaving behind a co-continuous cellulose acetate fiber. It is essential to understand these solubility parameters in order to achieve co-continuous fiber morphology and fabricate high surface area fibers.

1.2.6. Converting Cellulose Acetate to Cellulose

The moisture regain of co-continuously electrospun cellulose acetate fibers can be improved by converting cellulose acetate into cellulose. Liu and Hsieh, 2002, illustrated that electrospun cellulose acetate nanofibers could be converted to cellulose nanofiber membranes via alkaline hydrolysis in a process known as deacetylation. In this process cellulose acetate fibers are treated with 0.05 M NaOH aqueous and ethanol over a specified period of time, washed, neutralized, and dried under vacuum. FTIR analysis can be performed in order to confirm the removal of the acetate group and the complete conversion of the cellulose acetate to cellulose fibers [31,38].

1.2.7. Polyoxometalate Synthesis

Heteropolymolybdovanadates such as the free acid of the anion $[PMo_{10}V_2O_{40}]^{5-}$ referred to as 10-molybdo-2-vanadophosphoric acid ($H_5PV_2Mo_{10}O_{40}$) can be synthesized via a known process involving the reaction of sodium metavanadate ($NaVO_3$) with disodium phosphate (Na_2HPO_4) and the resulting reaction of the compound with concentrated sulfuric acid and sodium molybdate (Na_2MoO_4) in an oxygen containing solvent such as ethyl ether, ethyl alcohol, methanol, ethyl acetate, dimethyl sulfoxides, or tetrahydrofuran. It is necessary to purify the acids to obtain the correct stoichiometry. After extraction, the resulting compound appears as reddish orange crystals [39]. The microscopically self-assembled cubic crystals are expected to be on the scale of 70 μm and are formed from the aggregation of nano-scale building blocks [9]. The particles can be characterized via x-ray diffraction (XRD), Fourier transform infrared spectroscopy (FTIR), scanning electron microscopy (SEM), and energy dispersive spectroscopy (EDS) [9,40–42]. Figure 7 shows an example of an SEM image of microscale $H_5PV_2Mo_{10}O_{40}$ after synthesis [42].

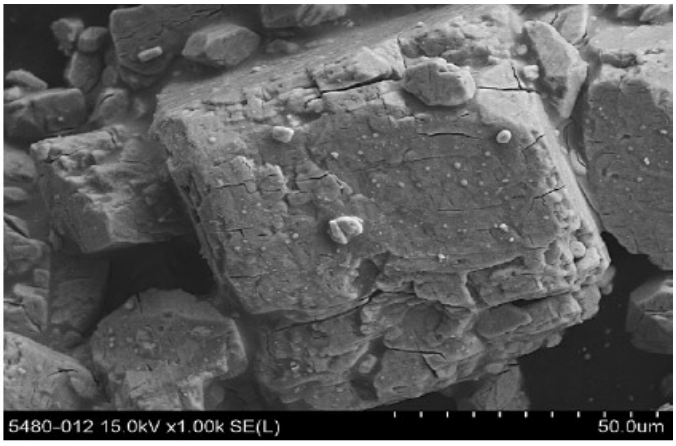

Figure 7: SEM Image of self-organized $H_5PV_2Mo_{10}O_{40}$ material [42]

1.2.8. POM Functionalization Techniques for Substrates

Forming a physical interaction between a POM and substrate, Drechsler et al., 2009 functionalized polymers with reactive species such as polyoxometalates by creating reactive oxygen species (ROS) on a polyurethane sponge via plasma treatment. The ROSs were then reacted with diisocyanate in the presence of argon and toluene creating isocyanate and silyl groups on the surface of the polymer that provided active binding sites for POMs as seen in Scheme 5. The POMs were grafted to the surface of the polymer in the presence of argon and tetrahydrofuran at room temperature for 24 h [28]. A similar procedure was used by Tan and Obendorf, 2006 to create grafting sites on a polyurethane membrane for poly(ethylene glycol). The reaction was performed under a nitrogen purge in the presence of a tin (II) catalyst, a toluene solvent, and a swelling agent [43]. This process can be modified slightly to graft polyoxometalates to cellulose membrane substrates. The limit to the amount of POM grafted to the surface of the membrane is the number of polyurethane functionalized reaction sites on the surface of the cellulosic fibrous surface. A suggested concentration range on cellulosic fibers is 0.1-20% by weight of POM on the fabric surface [26].

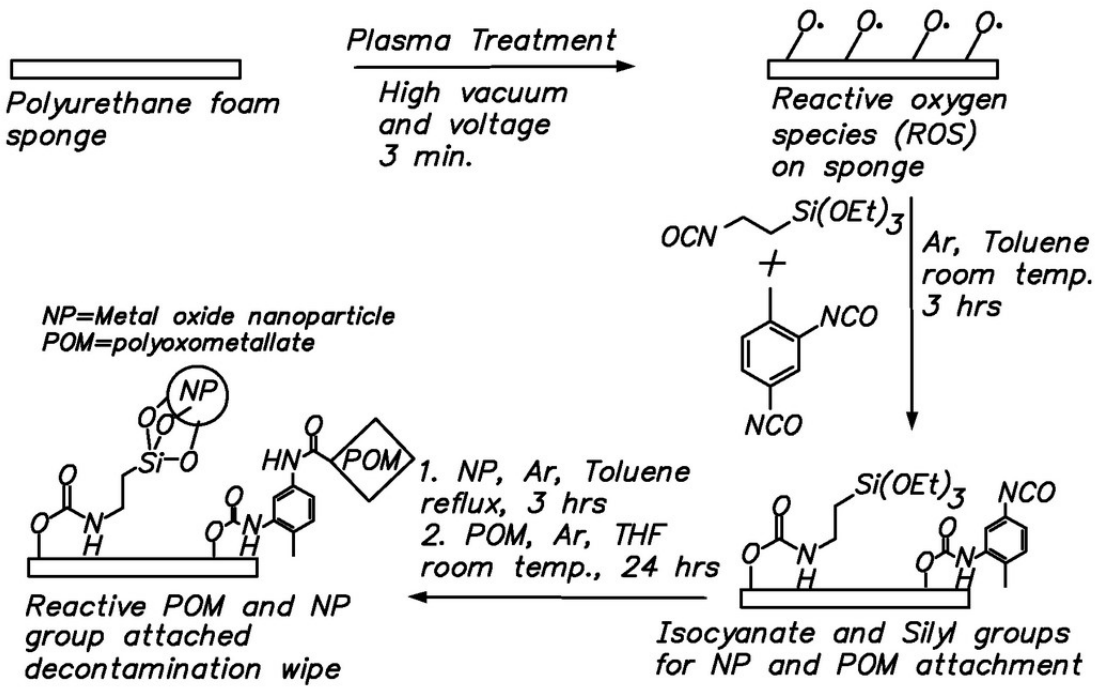

Scheme 5. The POM functionalization of a polyurethane substrate via physical linkages [28]

Other literature demonstrates how a chemical interaction can be formed between a POM and a substrate. A sol-gel technique (pH 1) was employed to prepare a mesoporous silica support. The silica support was functionalized with 3-aminopropyl-triethoxysilane (APTS) which was then dispersed in an aqueous solution of the transition-metal-substituted polyoxometalate (TMSP) for 24 h and held at pH 6-7. It was determined that a coordination bond formed between the silica support and the TMSP as shown in Scheme 6. The amount of APTS functionalized to the surface of the substrates was found to be dependent on the specific surface area of the silica supports [44,45].

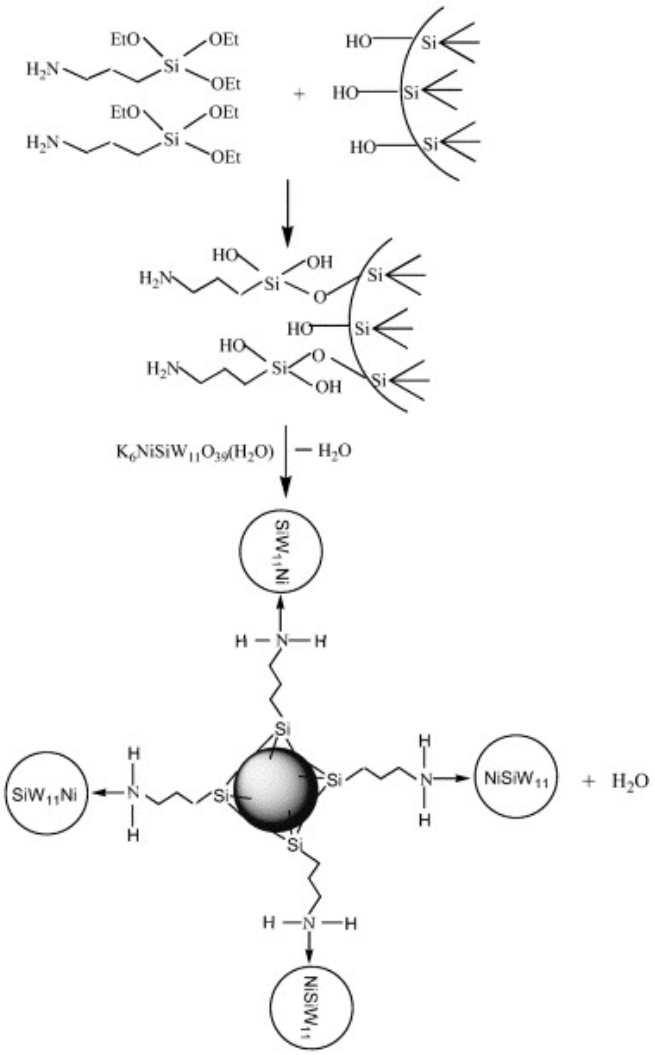

Scheme 6. Pathway of preparation of amine-modified silica attached with $SiW_{11}Ni$, where the black ball represents the silica network. $SiW_{11}Ni$ and silica are bonded by coordination of nickel centers in the cluster with the nitrogen atom of the amine surface groups in modified silica [44]

In Scheme 7 the mechanism of polyoxotungstate immobilization is shown on the surface of a high surface area silica support also modified with APTS [46]. Similar approaches to this technique can be found throughout the literature using POMs similar to

the one examined in this work as well as other types of POMs, making this method of POM substrate functionalization appear to be the most common [44,45,47].

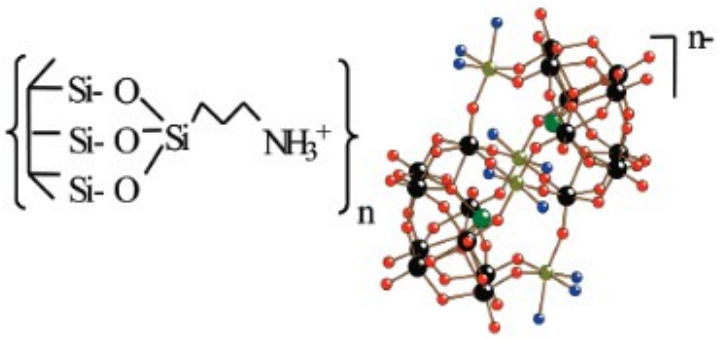

Scheme 7. A high surface area silica support modified with a polyoxotungstate using APTS as a functionalization intermediate - SBA-15-APTS-$Fe_4X_2W_{18}$ (n = 6, X = As^{III}, Sb^{III}; n = 4, X = Se^{IV}, Te^{IV}) [46]

Salon et al. (2007) demonstrated the functionalization of cellulose using APTS as seen in Scheme 8. In these experiments, cellulose fibers were soaked in a 2% silane solution (ethanol / water: 80/20, w/w) for 2 h. In the first step of the cellulose grafting procedure, hydrolysis of the silane occurs yielding a silanol derivative, and molecules of free alcohol are liberated. Hydrogen bonds are formed between the silanol and hydroxyl groups of the cellulose molecule as the hydrolyzed species is adsorbed. Chemical condensation occurring with thermal activation enables the formation of siloxane bridges [48]. Cellulose functionalized with APTS can be used for POM immobilization as was seen in the high surface area silica substrate examples.

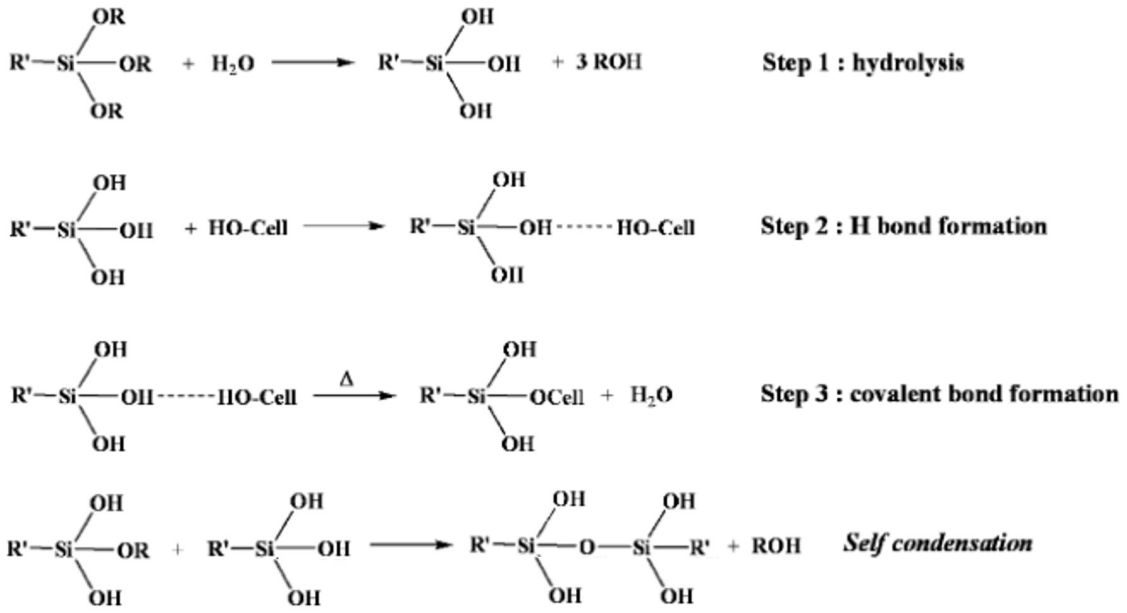

Scheme 8. Possible step-wise mechanism of silane-cellulose grafting [48]

1.2.9. Characterization of POM Functionalized Substrates

Schreuder-Gibson et al. (2003) developed a method for incorporating 10-molybdo-2-vanadophosphoric acid into electrospun fibers by dissolving POMs reacted with activated carbon or nano metal oxides in solutions of polyurethane and tetrahydrofuran (THF) in order to test their ability to destruct and absorb toxic organic compounds such as CEES. The structural effects upon moisture transport, air convection, aerosol filtration, porosity, tensile strength, and enhanced chemical activity of these membranes were measured using a variety of techniques [49]. Figure 8 shows the SEM images of an electrospun fiber mat used to incorporate CWA catalysts for protective clothing [25,27,49].

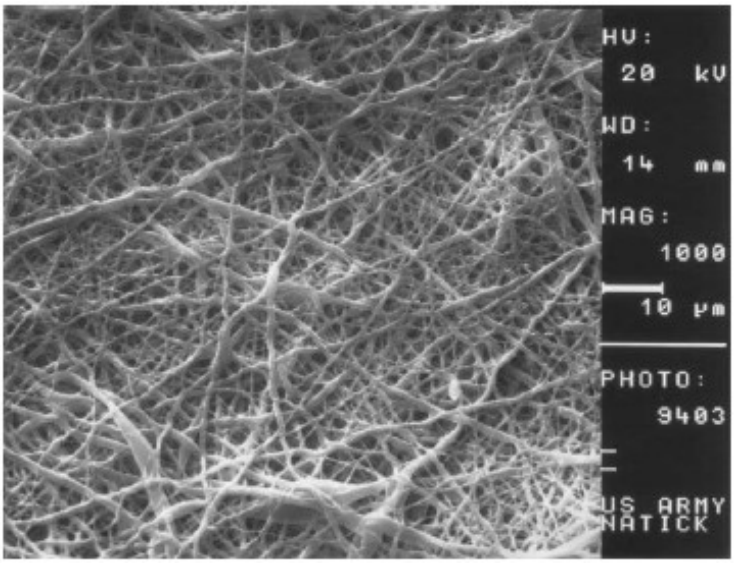

Figure 8: Electrospun fiber mat for incorporating CWA catalysts [27]

FTIR spectral analysis can be used to confirm the elemental composition of the membrane and the presence of the POM. Surface area measurements of the membrane can be made using BET gas adsorption [25]. High Performance Liquid chromatography (HPLC can be used to measure the decomposition of methyl parathion [27]. Pore size and pore size distribution of the membrane can be determined using a porometer and SEM images [49]. Since these membranes would serve as nanofiber layers in laminates within protective clothing, understanding their breathability in a garment is essential [49]. Analysis to assess the breathability of the membranes examining their porosity, water vapor permeability, and additional thermal comfort properties are explored in this work. Statistical analyses can help to determine overall trends resulting from the surface modification of the membrane with POMs and their degradation of methyl parathion.

1.3 Statement of Purpose

The overall objective of this work was to incorporate high loads of self-decontaminating compounds in semi-permeable, breathable, fibrous substrates and achieve self-decontaminating performance. As part of this overall objective, many steps took place. The raw material polyoxometalate (POM) $H_5PV_2Mo_{10}O_{40}$ was synthesized and characterized. A dual component cellulose acetate / polyethylene oxide polymer membrane ("non-grooved") was electrospun and characterized. Polyethylene oxide was selectively dissolved from the fibrous substrate in order to create high surface area grooved fiber morphology, and characterization of this process was performed to confirm the increased surface area. The resulting grooved membranes were deacetylated and characterization of this process was performed to confirm the conversion of the material to cellulose. Two different methodologies – "POM-grafting" and "POM-immobilization" were used to functionalize the non-grooved membranes, the grooved cellulose acetate membranes, the grooved cellulose membranes, 100% cotton, 55/45 cotton/polyester fabrics, and Tencel® peach skin fabrics with the self-decontaminating POM. The amount of POM loading of each substrate was characterized, the self-decontamination performance was measured and analyzed, and the effect of POM functionalization on material properties was related to substrate composition, morphology, and functionalization method. One functionalization method was scaled up and used to fabricate chemical protective coveralls commonly used to prevent agricultural workers from pesticide contamination. The POM loading of the coveralls was assessed, and thermal comfort properties of treated and non-treated coveralls were evaluated using a thermal manikin.

The purpose of this work is to develop new self-decontaminating materials for use in breathable protective clothing.

CHAPTER 2

FABRICATION & CHARACTERIZATION OF SELF-DECONTAMINATING POLYOXOMETALATE-FUNCTIONALIZED FIBROUS SUBSTRATES

2.1 Introduction

Polyoxometalates (POMs) are heteropolyanions, which can be used to oxidize or hydrolyze chemical warfare agents. These reactions can degrade toxins into less harmful byproducts. When the oxidation reaction occurs, the POM is reduced. Oxygen or any oxidant in the system can then re-oxidize the POM to its original state; the self-decontaminating agent is regenerated to be used for multiple decontamination cycles [15].

In order to develop self-decontaminating chemical protective apparel, Hill's group [6,25,27,50] and others [28] have incorporated POMs into fibers and fabrics such as micro-/nanofibers, polyacrylic, nylon and cotton fabrics, and polyurethane sponges to create catalytic self-decontamination of volatile organics, air toxins, and chemical warfare agents [6,25,27,28]. More recently, based on Hill's work, Lange and Obendorf showed that POMs can be incorporated into metal organic frameworks-another oxidization agent, at room temperature and grown on cotton to improve self-decontamination performance in protective clothing [51,52].

Although POMs such as $H_5PV_2Mo_{10}O_{40}$ have been incorporated into cellulose substrates to degrade volatile organics and chemical warfare agents such as CEES[1], it is still unclear how well they effectively degrade organophosphates [6,25,28]. It is also desirable to increase the loads of self-decontaminating compounds in fibrous substrates to

[1] 2-chloroethyl ethyl sulfide (CEES) is a sulfur mustard analog. Sulfur mustard is used as a chemical warfare agent.

enhance the self-decontaminating performance without compromising the breathability and comfort of such materials.

It is therefore the objective of the present work to fabricate grooved nanofibrous membranes and functionalize them with polyoxometalates (POMs), and to evaluate their self-decontaminating performance in degrading toxic organophosphates. The increased surface area of grooved nanofibrous membranes in comparison with non-grooved nanofibrous membranes and conventional textile substrates is expected to increase the loads of POMs grafted on the fiber surfaces, resulting in enhanced self-decontaminating performance.

2.2 Hypotheses

By using channeled cellulose acetate nanofibers, the surface area of traditional microporous nanofibrous cellulose acetate membranes will be increased providing more active sites to which the POMs will bind. This increase in POM active sites will enhance the catalytic degradation performance of methyl parathion, an organophosphate simulant of the chemical warfare agent (CWA) VX. The number of active sites for which POMs to bind is dependent on the fiber substrate and the surface area of the substrate. No statistical difference in the POM loading will be determined between the functionalization methods. Substrates of like fiber content and surface area will result in analogous levels of POM attachment. Decontamination performance of methyl parathion is not dependent on the method of POM functionalization.

2.3 Experimental

2.3.1 Materials

Cellulose acetate (M_n 30,000) in powder form (180955) and poly(ethylene oxide) (M_v 200,000) (181994) were obtained from Sigma-Aldrich (St. Louis, MO) in addition to the solvents acetonitrile HPLC grade (AX0145-1) from EMD Chemicals, Inc. (Gibbstown, NJ) and acetone (2440-16) from Mallinckrodt Chemicals (Phillipsburg, NJ) for electrospinning. BD Sterifill SCF 5-mL plastic syringes (Franklin Lakes, NJ) and a Harvard Apparatus PHD ULTRA electrospinning device (Holliston, MA) in combination with a Gamma High Voltage Research voltage source (Ormond Beach, FL) were used to fabricate the fibrous membranes. A standard solution of 0.1N sodium hydroxide and ethanol (24102), obtained from Sigma-Aldrich (St. Louis, MO), were used for the deacetylation process.

100% Cotton swatches (Style 400U Unbleached desized Cotton Print Cloth) were obtained from Testfabrics, Inc. (USA) and cut into 5 inch by 5 inch swatches. The Tencel® test fabric samples were obtained from Lenzing Corp. (Lafnitztal, Austria), and the 55/45 cotton polyester fabrics treated- and non-treated with N-halamines were obtained from Dr. Gang Sung of the University of California, Davis.

$H_5PV_2Mo_{10}O_{40}$ was synthesized using sodium molybdate dehydrate from EMD Chemicals, Inc. (EM-SX0650-2) (Phillipsburg, NJ), sodium metavanadate from Sigma-Aldrich (72060) (St. Louis, MO), sodium phosphate dibasic from Sigma-Aldrich (S0876) (St. Louis, MO), 0.5 N sulfuric acid (38295) from Sigma-Aldrich Fluka Analytical (St. Louis, MO), and methanol HPLC grade (34860) from Sigma-Aldrich (St. Louis, MO).

In order to functionalize the membranes with the polyoxometalates, Tin (II) 2-ethylhexanoate (S3252), hexamethylene diisocyanate (HMDI) (52649), and 3-aminopropyltriethoxysilane (APTS) (440140) were obtained from Sigma-Aldrich (St. Louis, MO). Toluene (FW-92.14, Lot: B46B20) and hexane (5189-16) were also obtained from Mallinckrodt Chemicals (Phillipsburg, NJ), and 85-87% phosphoric acid (0260) was obtained from J.T. Baker (Center Valley, PA).

The pesticide, methyl parathion (PS-94), and its degradation product, methyl paraoxon otherwise known as dimethyl-p-nitrophenylphosphate (PS-613) were purchased from Chem Service Incorporated (West Chester, PA). The methyl parathion degradation product p-nitrophenol (1048) was purchased from Sigma-Aldrich Fluka Analytical (St. Louis, MO).

Silanization of all glassware was done to reduce the adsorption of methyl parathion and its byproducts onto the surface of the glassware to keep subtle samples protected against the reactive effect of OH sites on the glassware. Silanization was done by coating and rinsing glassware with 5% (v/v) dimethyldichlorosilane in toluene for 10-15 seconds followed by two rinses with pure toluene and three rinses with methanol [53–57]

2.3.2 Methodology

2.3.2.1 Polyoxometalate Synthesis

10-molybdo-2-vanadophosphoric acid ($H_5PV_2Mo_{10}O_{40}$) was synthesized via the known process involving the reaction of sodium metavanadate ($NaVO_3$) with disodium phosphate (Na_2HPO_4) and the resulting reaction of the compound with concentrated sulfuric acid and sodium molybdate (Na_2MoO_4) [39]. The first step in this process was to prepare a sodium metavanadate solution by dissolving 24.4 g of $NaVO_3$ in 100 mL of

boiling deionized water. After complete dissolution, 5 mL of sulfuric acid was added. This solution was then cooled to room temperature. A sodium phosphate dibasic solution was made by slowly adding 7.1 g of Na_2HPO_4 to 100 mL of deionized water stirring at a high speed on a stir plate with a low and high setting to ensure complete dissolution. A sodium molybdate dihydrate solution was then made by dissolving 121 g of $Na_2MoO_4 \cdot 2H_2O$ in 200 mL of deionized water stirring at a high speed. The cooled sodium metavanadate solution was then added to the sodium dibasic solution while stirring at a high speed. These combined solutions were then added to the sodium molybdate dihydrate solution while stirring at a high speed. Then, 200 mL of 50 % sulfuric acid were added very slowly while the solution stirred vigorously. The addition of the acid raised the temperature of the solution significantly making slow addition of the acid imperative. Earlier studies on the synthesis of this compound recommended 85 mL of sulfuric acid or greater in order to achieve a weakly acidic pH. The slow addition of 200 mL of sulfuric acid achieved a pH of 3 which was measured once an hour for 4 h as the solution cooled to ensure pH stability. This cooled solution of 10-molybdo-2-vanadophosphoric acid was extracted with an excess (more than 500 mL) of methanol using a vacuum filter and flask as seen in Figure 9. The resulting precipitate was then dissolved in approximately 300 mL of water while stirring at a high speed. This solution was then placed over 50% sulfuric acid in a vacuum oven held at room temperature to enable the polyoxometalate 10-molybdo-2-vanadophosphoric acid to precipitate.

Extraction of 10-molybdo-2-vanadophosphoric acid with an excess of methanol in a vacuum filter flask

Precipitate that results from the extraction

Dissolved precipitate in deionized water precipitating over 50% sulfuric acid under vacuum

Figure 9: The extraction and precipitation of $H_5PV_2Mo_{10}O_{40}$

2.3.2.2. Polyoxometalate Characterization

After synthesis, the particles were characterized via several of the methods established in the literature including x-ray diffraction (XRD) using a Scintag Theta-Theta Diffractometer with a germanium detector, Fourier transform infrared spectroscopy (FT-IR) using a Nicolet Magna-IR 560 Spectrometer, scanning electron microscopy (SEM) using Tecscan-MIRA scanning electron microscope, and X-ray Microanalysis (EDS – Energy-Dispersive X-ray Spectroscopy & WDS – Wavelength Dispersive X-ray Spectroscopy) using a JEOL JXA-8900R WD/ED Combined Microanalyzer instrument [9, 40, 41, 42].

Procedural details for each of these characterization techniques are as follows: For XRD, the POM powder sample was ground to a small, uniform size and was then mounted on an indented plate, and the powder was smoothed and flattened as much as possible. A line source of 1 x 10 mm was used, and the region hit by the x-ray beam was controlled by using slits at 0.3 mm (diffracted beam slit) and 0.5 mm (scatter slit) on the source. These slits were used to balance the resolution and intensity of the diffraction peaks in order to

achieve high resolution using lower intensities. The theta angle, i.e. the germanium detector position, was at 0° when the mounted sample was horizontally aligned, and the Vernier scale detector angle was noted as 17.5°. The operating conditions of the instrument were set at a voltage of 45 kV and a current of 40 mA. A low to high angle continuous scan was made at a rate of 3° per minute (0.02° step size) within the range of 5° – 60°. The resulting peaks were compared to XRD patterns in the JADE software XRD library as well as the XRD results found in literature [9].

FTIR was conducted using a Nicolet Magna-IR 560 Spectrometer. In this technique infrared radiation is passed through the sample whether it is a solid on the mounting stage or a liquid held on a Teflon® holder. The resulting spectrum represents the molecular absorption and transmission of the sample.

For SEM analysis, POM particles were mounted onto an SEM sample peg using double sided tape and then sputter coated with palladium and gold in order to make the samples conductive. ImageJ analysis was used to determine the size of the particles.

Operating conditions for EDS were set to be at a range of electron beam accelerating voltages from 15 kV to 25 kV with a magnification of 430 at a take-off angle of 40°. The spectra resolution was 100 eV. The operating conditions for performing the WDS scan were set at an accelerating voltage of 25 kV, a magnification of 430, and covered the range of 175 mm to 168 mm in order to decipher the molybdenum peak from the sulfur peak.

2.3.2.3 Fabrication of Grooved Electrospun Fibrous Membranes

A 5-mL 15% w/v polymer solution was prepared by weighing 0.45 g of cellulose acetate (CA) and adding this to a weighed amount (0.3 g) of polyethylene oxide (PEO).

This 60/40 CA:PEO mixture of solids was then added to a vial and a 60/40 volume ratio of acetonitrile to acetone was added to make a 5-mL solution. The solution was sonicated for 30 min and then stirred at room temperature on a high speed for 1 h [32–35]. Tables 1 and 2 provide information on the physical properties and solubility of the polymers and solvents used for co-continuous electrospinning.

Table 1: Properties of Solvents

Solvent	**Acetonitrile**	**Acetone (Ac)**
Molar mass (g/mol)	41.1	58.1
Boiling point (°C)	81.6	56.2
Vapor Pressure (mmHg, 20°C)	73	184
Surface tension (dyn/cm, 20°C)	29.3	23.7
Viscosity(cP, 25 °C)	0.343	0.308
Solubility parameter[a] (δ, MPa)$^{1/2}$		
δ_{total}	24.3	19.9
$\delta_P/\delta_D/\delta_H$	18.0 / 15.4 / 6.1	10.4 / 15.5 / 7.0

a. δ_P: polar interaction, δ_D: dispersion force, δ_H: hydrogen bond

Table 2: Polymer Properties

Polymer	Cellulose acetate (CA)	Polyethylene oxide (PEO)
Molecular weight (g/mol)	30,000 (M_n)	87,000 (M_n)
Transition temperature (°C)	67 (T_g)	65 (T_m)
Solubility parameter[a] (δ, MPa)$^{1/2}$		
δ_{total}	25.1	20
$\delta_P/\delta_D/\delta_H$	12.7 /18.6 / 11.0	3.0 / 17.3 / 9.4

T_g: glass transition temperature, T_m: melting temperature

The solution was immediately loaded into a 5-mL plastic syringe for electrospinning. A syringe pump (PHD Ultra Pump; Harvard Apparatus) infused the polymer solution at speed of 0.05-mL/min through a stainless steel needle (Hamilton) with

a diameter of 0.016 in (0.41 mm) for 1 h. A 15-kV voltage was applied between the needle and an aluminum foil wrapped wire mesh (4 in^2 surface) taped to a Teflon® collection plate that was 15 cm from the syringe needle tip. An electric field was generated by the voltage between the needle tip and the collection surface enabling electrospun fibers to be deposited on the plate forming a nonwoven nanofibrous mat. Experiments were conducted at room temperature. The foil wrapped collection plate with the nanofibrous web composed of 60% cellulose acetate and 40% polyethylene oxide was then removed from the Teflon® plate, placed in the vacuum oven and vacuum dried for a minimum of 8 h at room temperature.

The nanofibrous electrospun fiber mats were carefully peeled from the foil and stored under vacuum until future experiments, where they were referred to as non-grooved/non-extracted fibrous membranes. To fabricate the grooved/extracted fibrous membranes, the electrospinning process detailed previously was performed using a volume of 8.3-mL of the 60/40 CA:PEO polymer solution so that the grooved/extracted membranes would have almost the same weight per unit area as that of the non-grooved/non-extracted membranes after the removal of PEO. The resulting fiber mats were carefully peeled from the foil and stored under vacuum for 24 h before being rolled gently into a loose roll using tweezers and then placed in a thimble filter. The thimble filter was placed in the glassware depository to conduct a Soxhlet extraction at 80 °C using HPLC grade deionized water for 8 days to remove the PEO component from the 60/40 CA/PEO fiber mat. The extracted fibrous membranes were then removed from the thimble filter with tweezers and vacuumed dried at room temperature for 24 h.

A portion of the extracted fibrous cellulose acetate membranes was deacetylated with 0.05 N sodium hydroxide in ethanol for 2.5 h. The resulting membranes were vacuum dried for 24 h, and FTIR analysis was used to confirm complete conversion of cellulose acetate to cellulose [31,38].

2.3.2.4. Additional Fibrous Substrates

As shown in Table 3, all textile substrates used for testing were cut to a dimension of 3 cm x 3 cm; the weights were measured using an analytical balance, and the thicknesses were measured using digital calipers.

Table 3. Properties of fibrous substrates prior to POM functionalization

Samples (3 cm x 3 cm)	n	Mean Weight (g)	g/m^2	Mean Thickness (mm)
non-grooved / non-extracted 60/40 CA:PEO membranes	10	0.05 ± 0.003	59.67	0.23 ± 0.02
grooved / extracted 60/40 CA:PEO membranes	10	0.05 ± 0.004	59.44	0.23 ± 0.02
grooved / extracted & deacetylated cellulose membranes	10	0.05 ± 0.001	57.00	0.22 ± 0.01
100% cotton Testfabrics plain weave	10	0.11 ± 0.008	126.78	0.23 ± 0.01
100% Tencel® Testfabrics twill	10	0.17 ± 0.004	184.33	0.27 ± 0.00
45/55 polycotton control plain weave	10	0.12 ± 0.003	128.89	0.23 ± 0.01
45/55 polycotton N-halamine treated plain weave	10	0.13 ± 0.003	142.22	0.23 ± 0.00

2.3.2.5. Characterization of Grooved Electrospun Fibrous Membranes & Additional Fibrous Substrates

2.3.2.5.1. FTIR-ATR

For the electrospun membranes, the FTIR spectrum was used to indicate the addition or loss of material, functional groups, or whole compounds such as the loss of

polyethylene oxide, which was expected after the membrane underwent a Soxhlet extraction. FTIR spectrums for cellulose acetate and polyethylene oxide polymers were measured separately from each other in powder form and compared to results found in the literature. From the literature a peak at 2891cm^{-1} was determined to be characteristic of the molecular absorption of pure polyethylene oxide (Ramesh et al., 2008). The FTIR spectrum for a cellulose acetate membrane has characteristic peaks around 1032 cm^{-1}, 1225 cm^{-1}, and 1747 cm^{-1}. Conversion from cellulose acetate to cellulose was characterized by analyzing a spectrum similar to that of cellulose acetate, but peaks at 1226 cm^{-1}, 1368 cm^{-1}, and 1740 cm^{-1} were expected to be absent if full conversion occurred [31].

2.3.2.5.2. Capillary Flow Porometry

The mean pore diameter of the membranes and additional substrates was measured using a Porous Materials, Inc. (PMI) Capillary Flow Porometer CFP-1100-AEHXL (Ithaca, NY). The samples were mounted in the test chamber, and the following test parameters were used: Dry up / Wet up, diameter = 20 mm, Silwick®, and 20.1 dynes / cm. First the porosity of the membrane was characterized dry. Then the membrane was wetted with Silwick®, and its porosity was characterized. The mean flow pore diameter and pore size distribution of non-extracted / non-grooved membranes were compared to those of the extracted / grooved membranes as well as the additional fibrous substrates.

2.3.2.5.3. Molecular Gas Adsorption: BET Surface Area Measurement

The surface areas of the membranes, cotton, and Tencel® were determined using the Brunauer, Emmet, Teller method known as BET. The BET technique used to measure the surface area of the fibrous substrates was krypton adsorption at -195°C on a BET Sorptometer at Porous Materials, Inc. in Ithaca, NY. The krypton gas adsorption method

was chosen to accommodate low surface area analysis. Measurement of very low surface areas by nitrogen adsorption can lead to less accurate measurements due to the high detection limits posed by the equipment. At surface areas lower than $1m^2$ the number of nitrogen molecules desorbed in the void volume of the test cell can exceed the number of molecules actually adsorbed by the sample surface. This will contribute to greater instrument uncertainty.

Krypton adsorption is the recommended alternative to overcome this challenge of obtaining accurate measurements since it improves the detection limit significantly and can measure surface areas as low as 0.05 m^2 or less. This is due to the lower vapor pressure of krypton. Its low vapor pressure causes less molecules to accumulate in the void volume of the test cell thus avoiding inaccuracies. At 77.4 K krypton is about 38.5 K below its triple point temperature (T_r = 115.35K). It sublimates (i.e., P_0, solid) at a pressure of approximately 1.6 torr. The saturation pressure of supercooled liquid krypton is 2.63 torr. When plugged into the BET equation, this means that the number of molecules in the free space of the sample cell is significantly reduced to approximately 1/300 that of the nitrogen case making krypton the more accurate choice for surface areas less than 1 m^2, particularly surface areas as low as 0.05 m^2 or below (Quantachrome, 2012).

The surface area of the fibers available to the krypton vapor for the non-extracted / non-grooved membranes was compared to that of the extracted / grooved fibers to see if an increase in surface area had been achieved by extracting PEO from the co-continuous structure. These surface areas were then compared to the surface areas of the cotton plain weave substrate, grooved electrospun cellulose, and the Tencel® substrate .

2.3.2.5.4. Moisture Vapor Permeability

Moisture vapor permeability of each of the fibrous substrates was measured according to the cup-test procedure found in Chapter 3 (3.3.2.4.2.) that utilized Appendix B (Determination of Water Vapour Permeability Index) of the BS 7209: 1990 – the British Standard Specification for Water Vapour Permeable Apparel Fabrics – test method.

2.3.2.5.5. Tensile Strength

The breaking force of the coverall fabrics was measured according to a modified version of ASTM D5034 Breaking Force and Elongation of Textile Fabrics (Grab Test) using an Instron with a static load cell of 100 N. The Instron was fitted with metal clamps (10 mm in width) and set to a gage length of 20±1 mm and crosshead speed of 300 ± 10 mm/min (so that the break occurred in 20±3 seconds). Fibrous substrate samples were cut to the dimensions of 10 mm x 40 mm with the length in the warp direction for woven substrates. Tests were run in triplicate, and each sample was cut from a different area of the respective substrate. The mean breaking force (N) was noted, and the mean percent elongation was calculated from the mean extension at break (mm) and gauge length (mm).

2.3.2.6. POM functionalization of Grooved Electrospun Fibrous Membranes & Additional Fibrous Substrates

2.3.2.6.1. POM Grafting – POM Functionalization Method 1 (M1)

After the specimens had been vacuum dried, each was weighed on the analytical balance (accuracy to 1 mg), and half were used for the POM grafting – POM functionalization method 1 experiments. The other half were set aside for the POM-Immobilization – POM functionalization method 2 (M2) experiments. It is important to note that this grafting procedure is suitable for textile substrates composed of polymers

with one or more pendant hydroxyl functional groups. In the case of the grooved and non-grooved 60/40 CA:PEO fibrous membranes, the one hydroxyl group in the cellulose acetate monomer acts as the reaction site, while the six pendant hydroxyl groups in a cellulose monomer act as the reaction sites for the grafting of the deacetylated cellulose membranes, the 100% cotton Testfabrics, the Tencel® test fabrics, the N-halamine treated 55/45 cotton / polyester, and the 55/45 cotton / polyester control fabric. In the first step of the reaction, a 100-mL grafting bath of 5% v/v hexamethylene diisocyanate (HMDI) and 0.25% v/v tin II catalyst in toluene was prepared and poured into a glass three-neck, 200-mL reaction flask. The specimen and a small stir bar were immediately placed into the flask. The vacuum purged flask was filled with the HMDI solution and held under nitrogen purge for the remainder of the grafting reaction. The temperature of the grafting bath was raised to 70°C while the bath and specimen were stirred for 1 h. The objective of this process was to use the hydroxyl functional groups on the cellulosic substrates to form urethane linkages between the fibrous polymer substrates and the diisocyanate (HMDI) intermediate in order to provide reaction sites for the polyoxometalates in the next step of grafting [43]. The toluene solvent and nitrogen purge process were used to hinder the formation of amines in the grafting bath prior to POM functionalization. After being functionalized with HMDI for 1 h, the specimen was removed from the flask and placed in a toluene bath for 4 h at room temperature (RT), a second toluene bath for 4 h at RT, and then a third toluene bath for 4 h at RT. These subsequent toluene baths were used to remove any unreacted HMDI from the functionalized substrates. The specimen was then vacuum dried overnight at RT, and characterized using FTIR and TGA.

After characterization of the HMDI surface functionalization, the specimen was placed in a 200-mL three neck flask that contained a 1% w/v grafting dispersion of $H_5PV_2Mo_{10}O_{40}$ in toluene under nitrogen purge and rapidly agitated at a temperature of 45°C for 24 h. The objective of this step was to enable any free ends (i.e. the isocyanate functional group) of the di-functional diisocyanate, not bound to the cellulosic substrate functional groups, to form physical linkages with POM pendant oxygen atoms. The literature suggests that it is primarily the pendant oxygens on the molybdenum and vanadium geometries of the polyoxometalate that are responsible for the potential formation of these bonds [2, 58]. After 24 h, 100-mL of deionized water was added to the flask under high speed agitation using a stir bar for 1 h to prevent POM agglomeration on the surface of the fibrous substrates. The reaction continued to be held under nitrogen purge at a temperature of 45°C. The specimen was removed and placed in a toluene bath for 3 h at RT, and three subsequent 24 h baths of deionized water. These baths were used to remove any unreacted POM from the grafted substrates. The specimen was then vacuum dried overnight at RT. This grafting procedure was performed on five of each of the textile substrates listed in Table 1, and these substrates were characterized using FTIR, SEM, TGA, Instron mechanical strength testing, and the porometer. An additional 5 samples of the 100% cotton were prepared in this manner and set aside for laundry durability testing. The functionalization process of the specimen can be seen in Scheme 9.

Scheme 9: POM Grafting of a cellulosic substrate (M1)

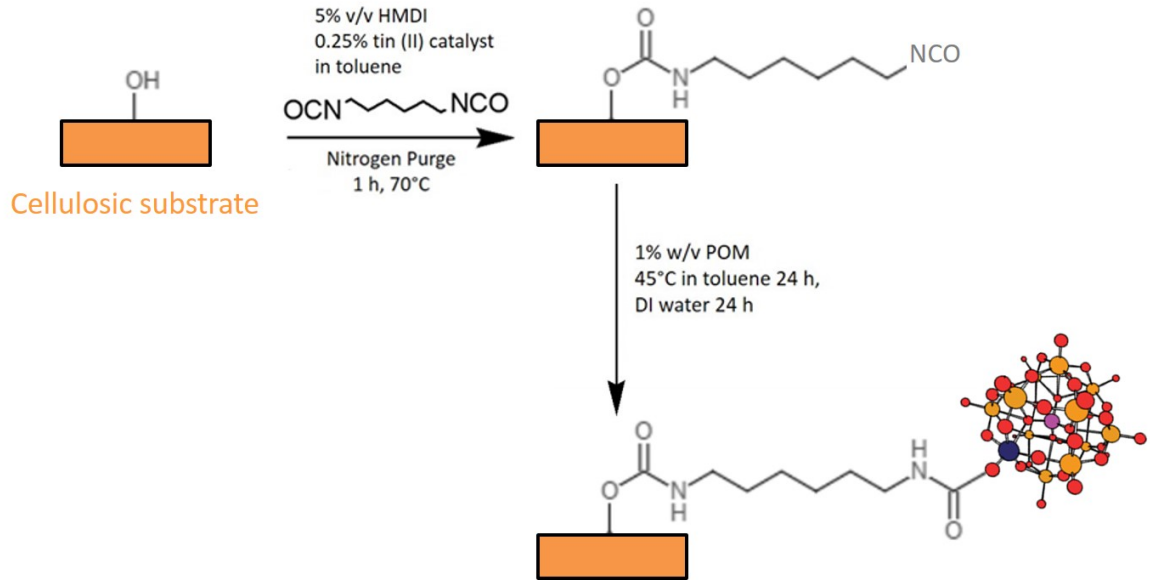

2.3.2.6.2. POM Immobilization – POM Functionalization Method 2 (M2)

After the specimens had been vacuum dried, each was weighed on the analytical balance (accuracy to 1 mg), and half were set aside for use in the POM grafting – POM functionalization method 1 experiments (M1). The other half were used for the following POM-immobilization procedure (a.k.a. electrostatic binding). A mixture of 3-aminopropyltriethoxysilane (APTS) in ethanol was added to an acidic water solution under mechanical stirring at 20°C, and the pH of the solution was lowered to 2 using concentrated phosphoric acid. This mixture was then left to react for 10 min to obtain a sol suspension. The textile substrate was then immersed in 30-mL of the suspension and left to react for 60 min. A 20-mL solution of 0.5g POM particles dissolved in the APTS suspension was then added. The textile substrate was left to react in the 50-mL bath of 5% APTS, 0.5% phosphoric acid, 1% POM in an 80/20 v/v solvent of deionized water with ethanol for 18 h at RT using rapid mechanical stirring to ensure solution uniformity. After

18 h, the specimens were removed and rinsed with mechanical stirring in 3 subsequent 50/50 v/v toluene/ethanol baths for one hour each, a hexane bath for one hour, three water baths for one hour each, and an ethanol bath for one hour in order to ensure the complete removal of any unreacted silane and unreacted POM particles. The textile substrate was then vacuum dried for 24 h. This procedure is summarized in Scheme 10. After being dried, the specimen was weighed and characterized using FTIR, SEM, and TGA. An additional 5 samples of the 100% cotton were prepared in this manner and set aside for laundry durability testing.

Scheme 10: POM immobilization on a cellulosic substrate (M2)

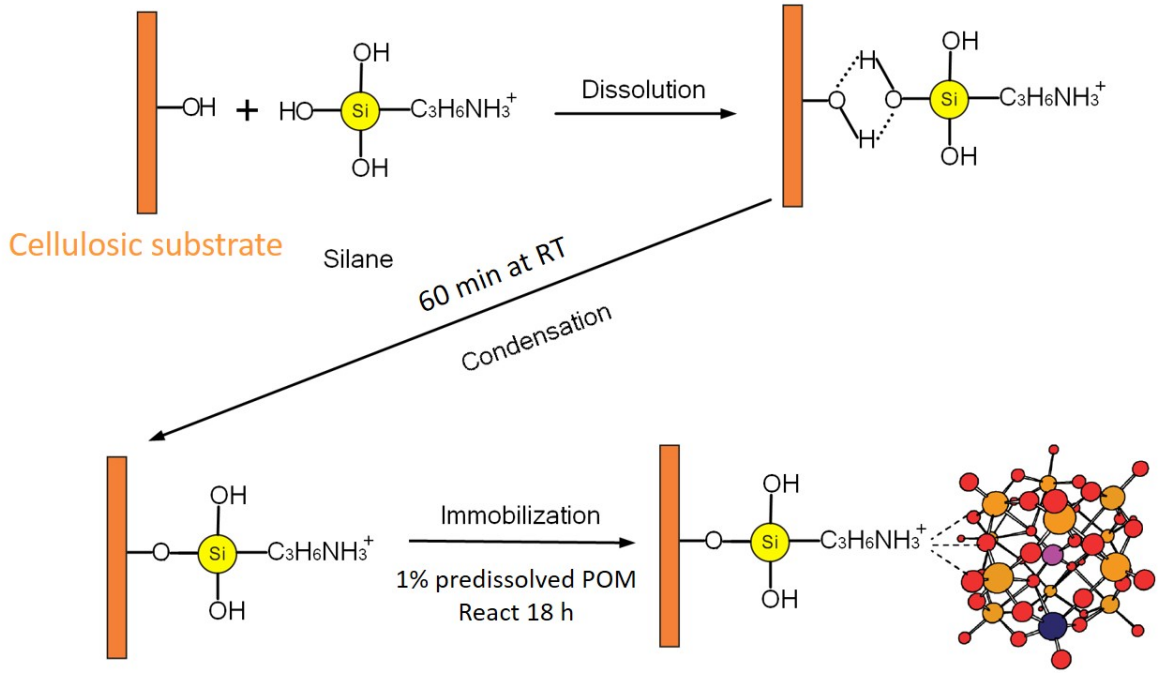

2.3.2.7. Characterization of POM Functionalized Fibrous Substrates

Fibrous samples were characterized via FTIR in order to detect the presence of HMDI or APTS and polyoxometalates (post-functionalization). FTIR spectrums for HMDI and APTS (liquid form) and $H_5PV_2Mo_{10}O_{40}$ POM (powder form) were used as controls in order to interpret FTIR peaks generated by the functionalized specimens.

Samples were also examined via SEM analysis on the Tescan Mira3 FESEM. The glass transition temperature of the grooved and non-grooved membranes was characterized before and after covalent grafting of the HMDI intermediate via DSC to determine if cross-linking was occurring using a Q2000 Differential Scanning Calorimeter. The POM percent add-on was quantified by measuring weight loss of each substrate before and after POM-treatment via TGA using a TA Instruments Q500 Thermogravimetric Analyzer.

The mean pore diameter of the POM-treated membranes and additional POM-treated substrates were measured using a Porous Materials, Inc. (PMI) Capillary Flow Porometer CFP-1100-AEHXL (Ithaca, NY) according to the procedure found in 2.3.2.5.2. The mean flow pore diameter and pore size distribution of non-extracted / non-grooved membranes were compared to those of the extracted / grooved membranes as well as the additional fibrous substrates.

After the fabrics were conditioned for 24 h, the laundry durability of the 5 POM-grafted cotton and 5 POM-immobilized cotton samples were assessed using a Terg-O-Tometer® (American Association of Textile Chemists and Colorists, 1988) [59,60]. Prior to wash testing, their L*, a*, b* CIELAB values were measured on the MacBeth Coloreye Spectrophotometer using Optiview ProPalette 2.0 software. A measurement was taken in four different areas of the fabrics and averaged. Next, a 500 mL wash bath was prepared with a 0.1% solution of AATCC Standard Liquid Laundry Detergent Without Optical Brightener in deionized water, and the bath was allowed to come to room temperature prior to testing. Once room temperature was reached, one of the POM-functionalized specimens was labeled with a tex-pen and placed in the bath. Additional untreated 100% cotton fabric specimens were weighed and added to the bath as ballast until the liquor ratio was 16:1.

The bath was agitated at a speed of 100 cycles per min for 15 min at RT. (Temperature controls on the Terg-O-Tometer® showed inconsistencies when heat was applied to the bath, so a room temperature procedure was selected instead.) When the wash cycle was complete, the goods were removed, an aliquot of the bath was set aside for characterization on the UV-Vis Spectrophotometer. The goods were placed back in the metal bath container and filled with 500 mL of deionized water to perform a rinsing cycle at RT for 5 min. This step was repeated for a second rinse cycle for 5 min. Ballast swatches and the test-fabric were hung to air dry for 24 h before the test was repeated for five additional wash cycles. Once five wash cycles were complete the fabrics were air dried for 48 h and underwent characterization via the TGA to determine the change in POM percent weight add-on and via the MacBeth Coloreye Spectrophotometer to measure the ΔL, Δa, Δb, and ΔE_{CIELAB} values of the respective swatches. The test was run with five replicates with each type of POM-functionalized cotton. Results were analyzed and related to the method of POM functionalization.

2.3.2.8. Decontamination of Methyl Parathion by POM Grafted Fibrous Substrates

A method was developed using HPLC-DAD by Lange and Obendorf [51] to determine the amount of methyl parathion degradation. This same procedure was used to determine the amount of methyl parathion degradation by polyoxometalates. All compounds were measured with a reverse-phase HPLC combined with a diode array UV-vis detector from the Agilent (Santa Clara, CA) HP series 1200. The injection volume was 20 µL. The set-up was run with an Agilent XDB-C18 reversed phase column with 5-µm particle size and 4.6 x150 mm dimension and 25 °C. The mobile phase consisted of 50% acetonitrile and 50% water with 0.5% formic acid and ran for 15 min. The UV-vis detector was set to scan

at 230, 280, and 320 nm. Retention time of methyl parathion was noted, and it was ensured that its peak was separated sufficiently. A calibration curve relating the concentrations of methyl parathion to the peak area given by the HPLC-DAD was replicated from the Lange and Obendorf [51] procedure by making a 100 mg/L stock standard solution of methyl parathion in hexane. Methyl parathion was dissolved in hexane at the following concentrations: 0.25, 0.5, 5, 10, 25 mg/L, and HPLC data from these specimens was used to determine a standard equation for the relationship between methyl parathion concentration and the HPLC-DAD.

$$peak\ area\ (mAu) = 362.5 * methyl\ parathion\ concentration\left(^{mg}/_{L}\right) \quad [1]$$

The result of this equation was then multiplied by the known volume to obtain the mass of methyl parathion. Wavelength scans at 320 nm were used to determine the amount of methyl parathion for each specimen. Standards for the expected degradation products of p-nitrophenol and methyl paraoxon (a.k.a. dimethyl-p-nitrophenyl phosphate) were analyzed using the HPLC-DAD to determine their retention times. A standard solution for p-nitrophenol was made at a concentration of 0.070 g/L in HPLC grade deionized water, and a standard solution for methyl paraoxon was made at a concentration of 0.4 g/L in hexane. These solutions were sonicated for 30 min prior to testing. After achieving complete dissolution, 1 mL of these solutions was taken with a syringe. A syringe filter (nylon Cameo II 25mm) was attached, and the filtered solutions were transferred to the corresponding HPLC vial. These samples were analyzed on the HPLC-DAD using the same method as described above. Each time the degradation performance of the polyoxometalate grafted substrates was measured, these standard solutions of degradation products were made and analyzed on the HPLC-DAD so that degradation products

resulting from the POM decontamination could be recognized by the retention times of the peaks.

A standard solution of 0.016 g /L methyl parathion in hexane was made and sonicated for 30 min. To determine the decontamination performance of the polyoxometalate functionalized substrates, each POM grafted specimen was vacuumed dried for 24 h at RT and then placed in individual sealed containers of 20-mL of the methyl parathion standard solution. 1-mL aliquots were withdrawn from each vial by a syringe, filtered (nylon Cameo II 25mm HPLC syringe filter), and placed in 1.5-mL HPLC vials at varying time intervals between 1 h and 1 week (1 h, 2 h, 5 h, 10 h, 24 h, 48 h, 72 h, 168 h). These solutions as well as hourly aliquots of methyl parathion standard solution were then analyzed on the HPLC-DAD using the method detailed above. After one week (168 h), each specimen was then removed from the 20-mL vial and washed thoroughly in hexane, vacuum dried, and stored in a vacuum desiccator.

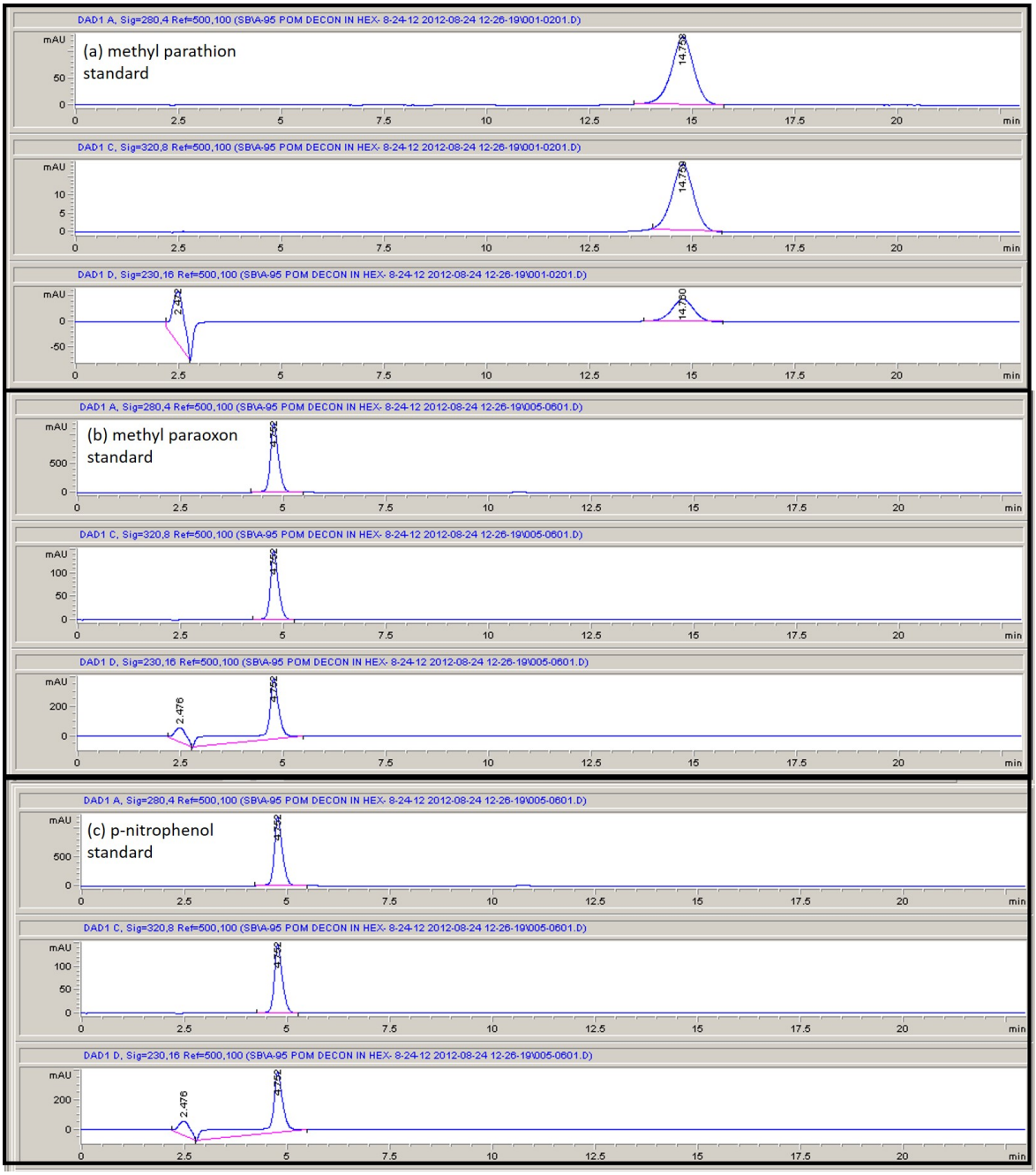

Figure 10: HPLC Chromatographs of standard solutions of (a) methyl parathion in hexane at UV-vis: 280 nm, 320 nm, and 230 nm, (b) methyl paraoxon in hexane at UV-vis: 280 nm, 320 nm, and 230 nm (c) p-nitrophenol in DI water at UV-vis: 280 nm, 320 nm, and 230 nm;

2.3.2.9. Statistical Analysis

Each treatment had five replicate samples tested for methyl parathion degradation. ANOVA tests were used to determine if the mean amount of methyl parathion degradation was statistically significantly different for the various treatments. One-way ANOVA statistical analysis of the BET surface area measurements was performed to determine if the mean surface areas of the substrates were statistically different from each other. A more conservative Wilcoxon / Kruskal-Wallis Test was also performed to examine statistical differences in the means of the grooved and non-grooved membrane BET surface areas.

2.4 Results and Discussion

2.4.1. Characterization of Polyoxometalate $H_5PV_2Mo_{10}O_{40}$ Synthesis

2.4.1.1. FTIR

When considering what functional groups to analyze and identify from the FTIR spectra of specimens containing POM, it is important to consider the structure and geometry of $H_5PV_2Mo_{10}O_{40}$. The heteropoly anion consists of a central phosphate (PO_4^-) tetrahedron encompassed by ten molybdenum oxide (MoO_6) octahedra (square bipyramid of MoO_3). The oxygens, trans to the terminal oxygens on the vanadium centers, are connected to the central tetra-bridging oxygens. These characteristics are found in most Keggin-type heteropoly compounds [2]. As a mixed addenda Keggin unit with some reduced structural symmetry (due to the incorporation of vanadium in addition to the phosphorus and molybdenum heteropolyanions), the chemical structure of this POM can be correlated with five to six characteristic peaks or bands found in the IR spectrum of the

experimental POM synthesis product [2,9,26]. Expected functional groups to examine include P-O, Mo-O, and V-O, singly or doubly bonded with differing bond lengths and angles [9,57,58,61,62]. The bond geometry, stretching, and vibrational modes of the functional groups determine the location of their absorption bands on the spectrum [26,57,63]. For example, the inter-octahedral M-O-M (M: Mo or V) vibrations can occur at the same and/or different wavenumbers than the intra-octahedral M-O-M vibrations depending on the size of the bond angles. Further examination of the IR spectroscopy literature provided correlating band values for compounds such as PO_4^{3-} (phosphate anion), MoO_3 (molybdenum trioxide), HSO_4^- (hydrogen sulfate), Na_2MoO_4 (sodium molybdate), and closely related molybdate, vanadate, and molybdovanadate POM structures [26,53–55,57,64–66].

Figure 11 (a) shows the FTIR spectrum of the synthesized particles with absorption bands at 3462, 1650, 1160, 1060, 858, 775, and 600 cm^{-1}. The strong, broad band at 1160 cm^{-1} correlates well with the central phosphate tetrahedral anion [53,54]. The strong, broad band at 1060 cm^{-1} correlates closely with the Mo=O, P-O functional groups, and the stretching mode of V=O, as well as peaks seen in the literature for PO_4^{3-} and MoO_3 [9,14,53,54,58,62,67]. A strong, broad peak at 858 cm^{-1} correlates closely with MoO_3 compound spectra and also can be attributed to the M-O-M vibrations of a doubly bridging oxygen connecting two contiguous chains in the structure. This broad peak encompasses part of the region (722-840 cm^{-1}) where evidence suggests that these M-O-M vibrations can occur when the bond angles of the complexes are greater than 140° [53,54,61,63].

Although there are similarities, the observed IR peaks of the experimentally synthesized POM have some differences from what has been reported in the literature for

this POM as seen in Figure 11 (b) [9,14,58,61,62]. Arichi et al.[9,62] reported peaks located at 3422, 1618, 1160, 1060, 958, 866, 784, and 590 cm^{-1}. By comparing the spectra in Figure 11 (a) to that from the literature in Figure 11 (b), it is evident that some differences exist, particularly in terms of the peak intensity; some of these differences are likely caused by the residual lattice moisture while others indicate that the synthesized compound may be an isomer of PV_2Mo_{10} or lacunary form of PV_2Mo_9 which would result from the loss of one MO_4^+. These possibilities could result from pH fluctuation during any of the processes such as synthesis or substrate-functionalization. While pH was carefully monitored during these processes to achieve the desired products, it was also observed that these reactions, particularly POM synthesis, are very sensitive to minimal pH changes which may have occurred despite vigilant efforts to control this critical factor [9,62]. Broad bands seen in the following regions of the spectrum (3300-3400 cm^{-1}, 2240 cm^{-1}, and 1610-1650 cm^{-1}) have been correlated with the presence of water in the sphere coordination (secondary structure) and may reflect the stretching [asymmetric, symmetric, and bending] fundamentals of residual lattice moisture [9,26,64]. Because the particles were stored in a vacuum desiccator over the course of testing to help remove residual water, the bands in this region of the spectrum in Figure 11 (a) may have lower intensities than the bands seen in the residual water region of the literature POM spectrum in Figure 11 (b).

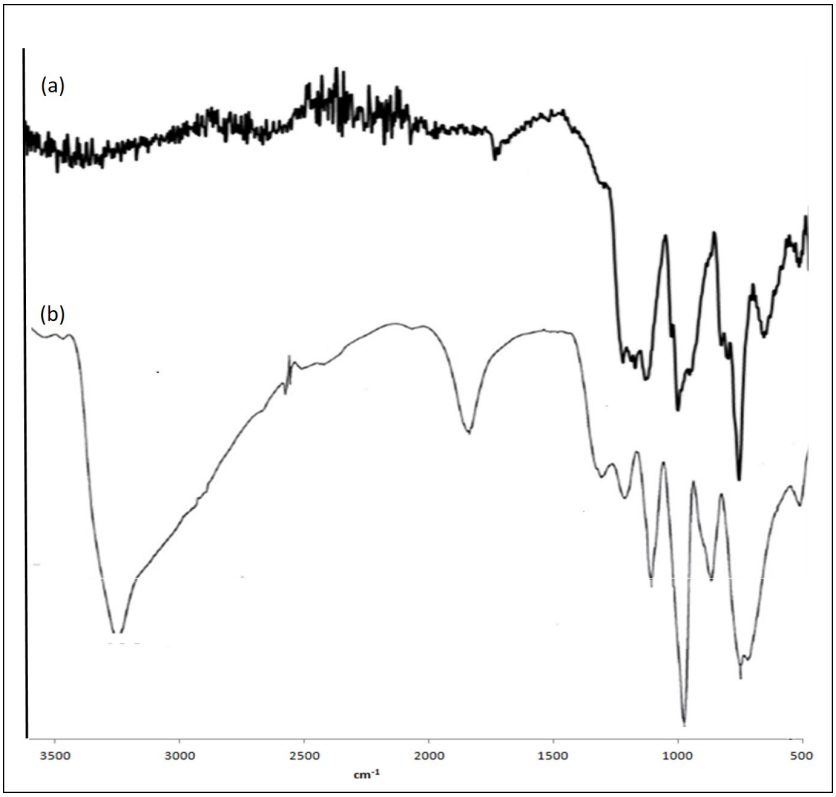

Figure 11: FTIR % Transmittance Spectra of $H_5PV_2Mo_{10}O_{40}$ (a) from experimental synthesis and (b) spectrum from literature [9]

Byproducts of the synthesis, which were identified by later analysis with XRD and EDS, may have been one of the causes of the slight deviation of the synthesized compound from the spectral signature and peak intensities found in the literature. The residual hydrogen sulfate present in the POM resulted from using an excess of sulfuric acid in order to achieve the pH of 3 for synthesis. Therefore, IR bands for this byproduct can be observed at 1060, 856, and 600 cm^{-1} and may have strengthened the intensity of those peaks [53–57]. It is also of interest to note that bands in the range of 2200-1200 cm^{-1} are commonly associated with residual impurities that may be contained in the preparative reagents [68].

While weak bands are present in this spectral region of the experimentally synthesized POM, no additional impurities were examined in this study.

2.4.1.2. X-ray Diffraction (XRD)

The x-ray diffraction peaks for the synthesized $H_5PV_2Mo_{10}O_{40}$ did not correspond to what was seen in the literature as shown in Figure 12 [9]. A reflexion at $2\theta = 9°$ is typical for a molybdovanadate Keggin structure [9,61]. However, most XRD peaks were seen at higher angles between 20°-50° indicating large lattice spacings unlike the XRD peaks found at smaller angles in the literature results. Using the JADE software library matching tool, peak analysis showed the closest matches with the lattice patterns for Na_2SO_4 as seen in Figure 12 (a) and Na_2HSO_4 as seen in Figure 12 (b). Matches were also made for crystalline structures of vanadium oxide and molybdenum oxide with the closest matches achieved in the second try at synthesizing $H_5PV_2Mo_{10}O_{40}$. These results do not confirm the presence of $H_5PV_2Mo_{10}O_{40}$ in its crystalline form. Instead, they indicate that the only crystalline compounds present are Na_2SO_4 and Na_2HSO_4.

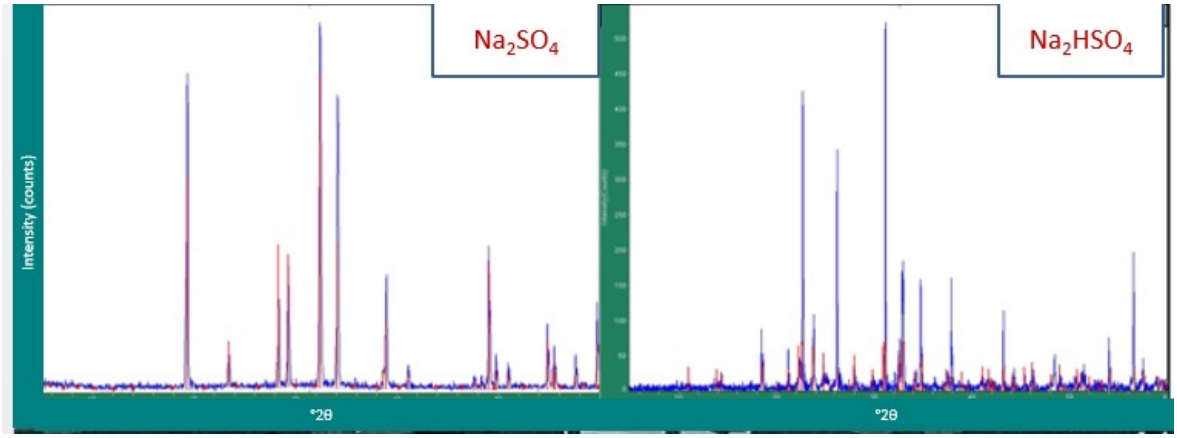

Figure 12: XRD of synthesized particles with Na_2SO_4 synthesis byproduct (a) with Na_2HSO_4 byproduct (b) (Synthesized particles are shown in blue. Byproducts are shown in red.)

2.4.1.3. Scanning Electron Microscopy (SEM)

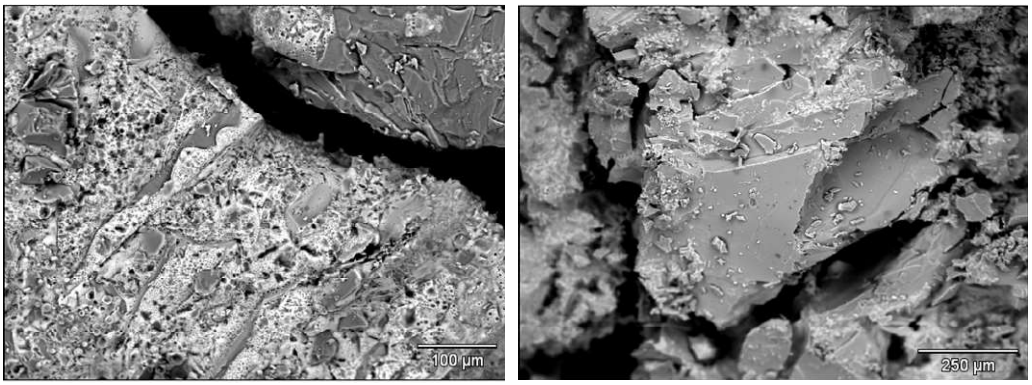

Figure 13: SEM Morphology of synthesized $H_5PV_2Mo_{10}O_{40}$

SEM images and further ImageJ[2] analysis of POM-functionalized substrates showed that POM particle size ranged from 0.5 - 5 µm which corresponded to values reported in the literature [9,62].

[2] ImageJ is an image processing program

2.4.1.4.. X-ray Microanalysis

2.4.1.4.1. Energy Dispersive X-ray Spectroscopy

Energy-dispersive x-ray spectroscopy (EDS) was used to measure the energy of the x-rays and perform elemental analysis of the POM particles. The resulting Figure 14 illustrates the elemental structure of the POM including peaks for the phosphorus, vanadium, molybdenum, and oxygen. Peaks for the Pd and Au sputter coating of the sample, which was necessary to make the sample conductive in preparation for this technique, are also present. The sodium sulfate and hydrogen sodium sulfate byproducts of synthesis that were represented in the XRD pattern mentioned in section 2.4.1.2. are also apparent. The peak height of each elemental peak can be used as a qualitative representation of the amount of that element present in the structure. WDS was performed to measure the wavelengths of the energy and determine whether the strong EDS peak between 2 and 3 KeV could be attributed to sulfur or molybdenum. From this information, it was determined that the elements of the POM were all present in the synthesized particles.

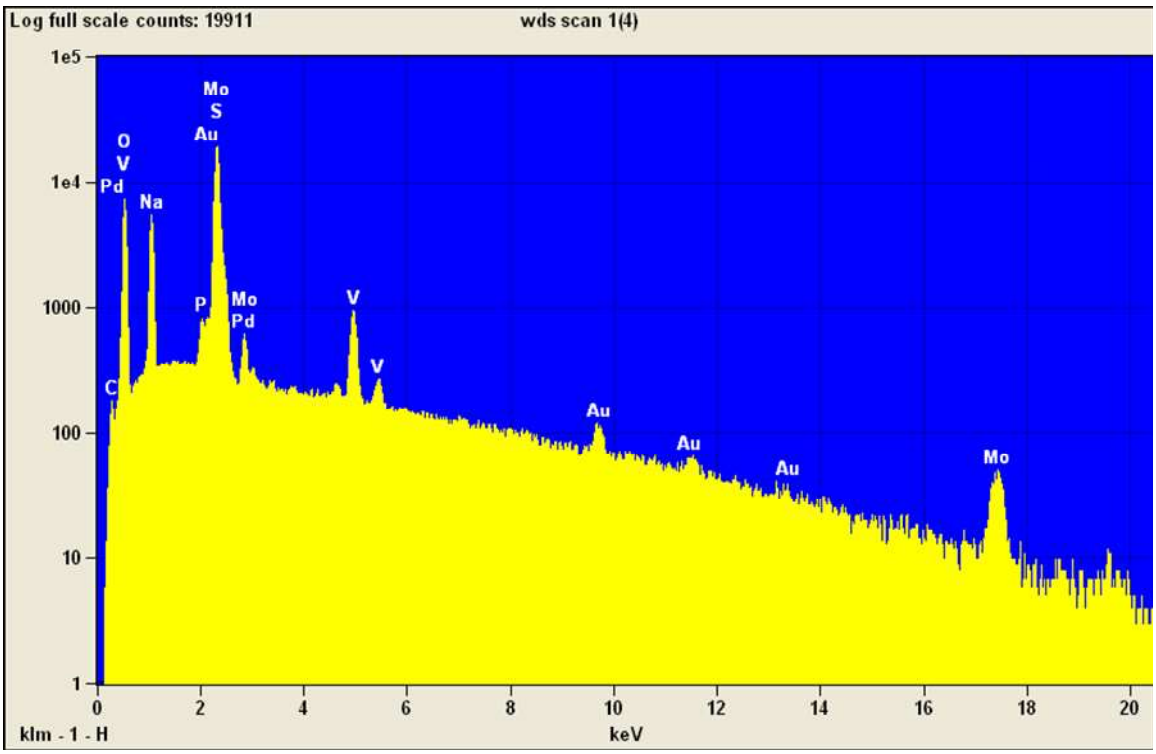

Live Time: 30.0 sec.; Acc.Voltage: 25.0 kV; Take Off Angle: 40.0 deg.

Figure 14: EDS Elemental Analysis of $H_5PV_2Mo_{10}O_{40}$

EDS confirmed that all elements composing the POM structure were present in the precipitate from the synthesis.

2.4.1.4.2. Wavelength Dispersive X-ray Spectroscopy

Wavelength dispersive x-ray spectroscopy (WDS) was used to scan the particles in order to determine the specific elemental identity of strong peaks attributed to two elements as seen in the EDS results (Figure 14). In the WDS results, the x-axis is the l-number (mm) representing the crystal lattice spacing in the spectrometer that is used to diffract the x-rays. Figure 15 shows that the strong peak between 2-3 KeV was due to a greater presence of sulfur than molybdenum. The presence of sulfur can be attributed to the synthesis byproducts of sodium sulfate and hydrogen sodium sulfate.

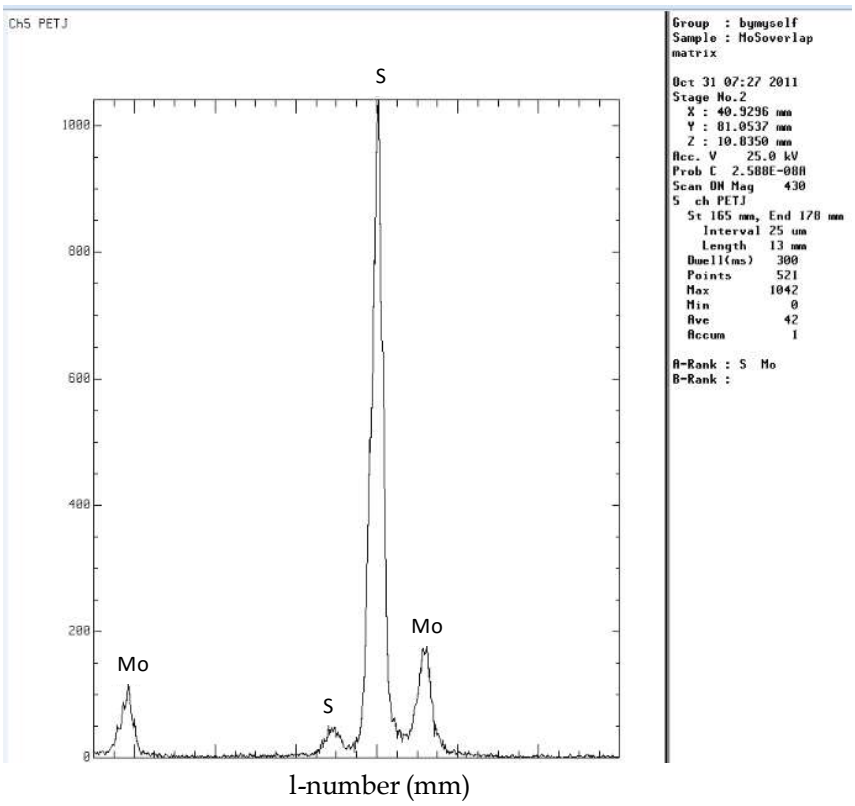

Figure 15: WDS Elemental analysis of the molybdenum and sulfur peak

2.4.2. Characterization of Fibrous Substrates

2.4.2.1. FTIR

When the polymers cellulose acetate and polyethylene oxide were analyzed via FTIR spectroscopy in their solid phase, their absorption signature showed major peaks at 1740 and 1032 cm^{-1} for cellulose acetate and at 2879, 1090, and 841 cm^{-1} for the polyethylene oxide. The strong peak at 1740 cm^{-1} correlated with an aliphatic acetate ester functional group, while the strong, broad peak at 1032 cm^{-1} correlated with the secondary primary alcohol functional groups of cellulose [54,56].

Figure 16 shows the FTIR spectrum of both the (d) grooved/extracted and (c) non-grooved/non-extracted fibers relative to their controls (a) cellulose acetate and (b)

polyethylene oxide. These spectra confirm that almost all PEO was removed from the 60/40 CA:PEO membrane via the Soxhlet extraction using deionized water in the grooved fibers due to the significant decrease in the size of the peaks at 2879, 1090, and 843 cm^{-1}, which are characteristic of PEO. The decrease in the size of the other peaks, specifically at 1740 and 1032 cm^{-1}, represent the loss of some cellulose acetate during the extraction process.

After the cellulose acetate was deacetylated as shown in Figure 17 (b), peaks were not apparent at 1227 cm^{-1}, 1368 cm^{-1}, or 1740 cm^{-1} while a strong peak was still apparent at 1032 cm^{-1} indicating the removal of acetate and conversion to cellulose [31,38].

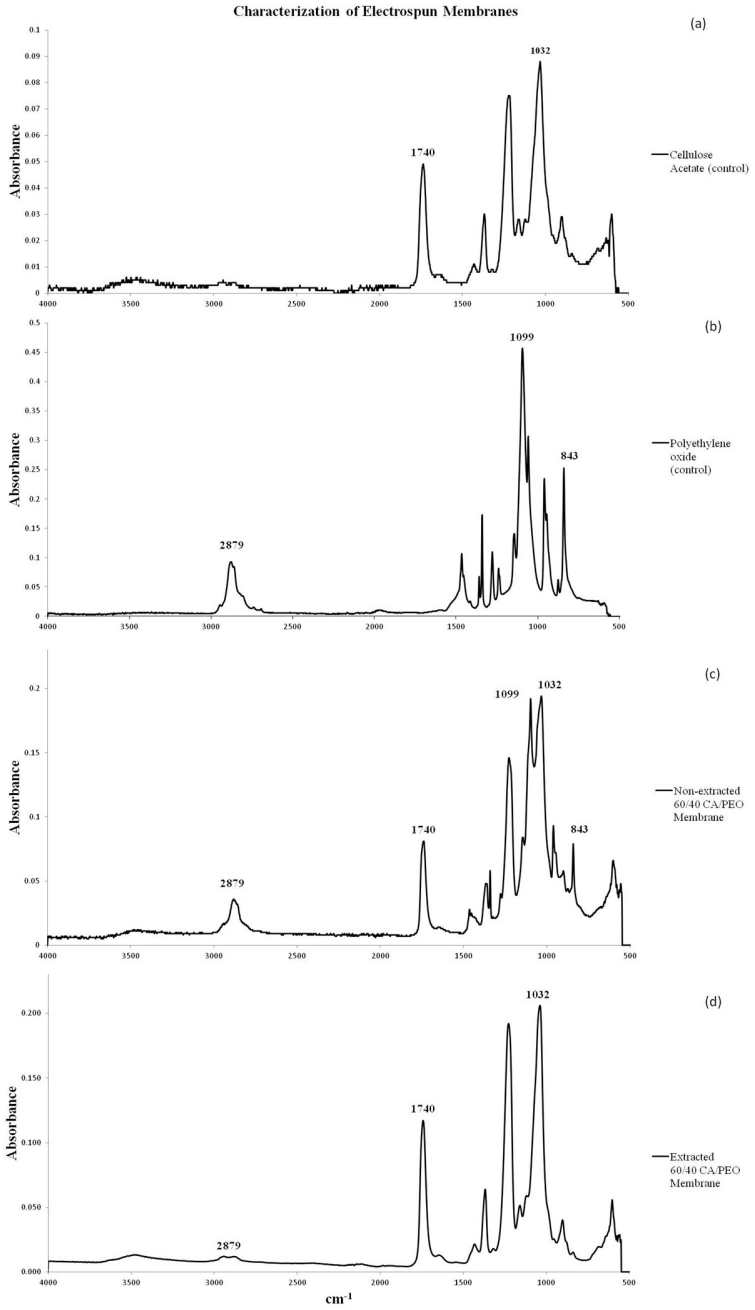

Figure 16: FTIR characterization of cellulose acetate / polyethylene oxide membranes (a) cellulose acetate (control) powder (b) polyethylene oxide (control) powder (c) non-extracted 60/40 CA/40 membrane (d) extracted 60/40 CA/40 membrane [Membranes were made with 60/40 CA/PEO in 60/40 Acn/Ace solvent. Non-extracted membranes are also called "Non-grooved" membranes, while extracted membranes are called "grooved".]

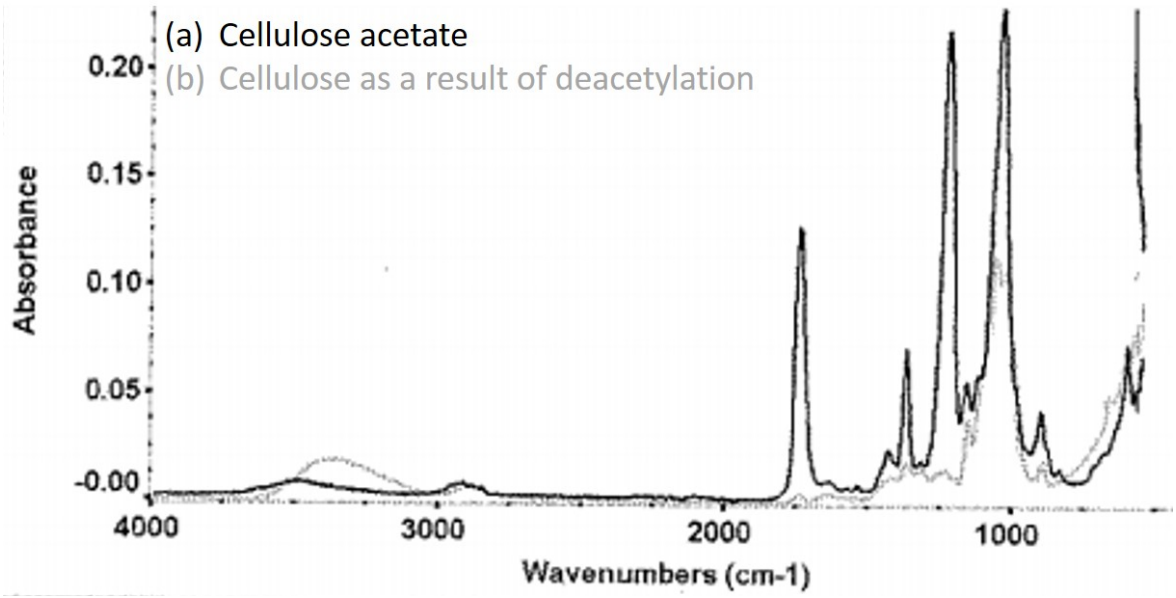

Figure 17: FTIR characterization of (a) grooved cellulose acetate fibrous membranes and (b) deacetylated grooved cellulose fibrous membranes

2.4.2.2. SEM

In comparing Figure 18 (a) of the non-grooved / non-extracted fibers to Figure 18 (b) of the grooved / extracted fibers, it is evident that the extraction of PEO led to the creation of grooved fiber morphology throughout the structure of the membrane. Figure 18 (a) shows that before extraction, the 60/40 CA:PEO fibers surfaces are smooth, while Figure 18 (b) shows more surface roughness. Achieving this grooved fiber morphology was critical to testing the hypotheses. ImageJ analysis of SEM Figure 18 (a) and (b) of the membranes showed that the fibers ranged from 1 to 2 μm in diameter both before and after extraction. Therefore, the grooved membranes had the same fiber diameter but greater surface roughness than the non-grooved fibers.

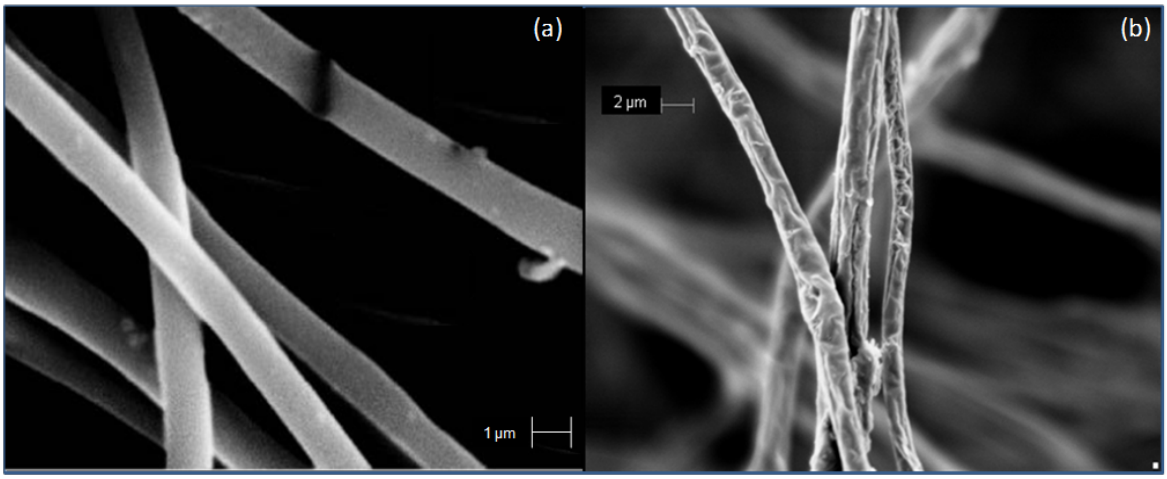

Figure 18: (a) Non-grooved / Non-extracted 15% w/v 60/40 CA:PEO fibrous membranes (b) Grooved / Extracted cellulose acetate fibrous membranes after Soxhlet extraction of polyethylene oxide

2.4.2.3. BET Surface Area Measurement

BET testing determined that the mean surface area of the non-grooved / non-extracted membranes was 0.03 m^2/g with a standard deviation of 0.01, while the mean BET surface area of the grooved / extracted membranes was 1.61 m^2/g with a standard deviation of 0.65 (Figure 19). As expected, the surface area of the grooved membranes was higher than reported values for cellulose acetate fabrics (average nitrogen adsorption BET surface area of 0.38 m^2/g) most likely due to the grooved fiber morphology created by the PEO extraction [69]. The mean multipoint krypton adsorption BET surface area of the grooved and deacetylated cellulose membranes was 1.43 m^2/g with a standard deviation of 0.41 which is comparable to the surface area of the grooved cellulose acetate membranes indicating that the conversion of the cellulose acetate membranes to cellulose did not result in a significant difference in surface area. The surface area of the 100% cotton plain

weave test fabric was 0.06 m^2/g with a standard deviation of 0.01, and the mean surface area of the Tencel® peach skin fabric was 0.17 m^2/g with a standard deviation of 0.02. One-way ANOVA statistical analysis of the BET surface area measurements via krypton gas adsorption of the non-grooved and grooved fibrous membranes showed that the difference in surface area between the grooved and non-grooved treatments was statistically significant with a p-value of 0.0001. A more conservative Wilcoxon / Kruskal-Wallis Test also showed that the increase in surface area for the grooved membranes was statistically significant with a p-value of 0.0197. This increase in surface area for the grooved fibers was critical to testing the hypotheses pertaining to an increased decontamination performance via increased fiber surface area for POM binding.

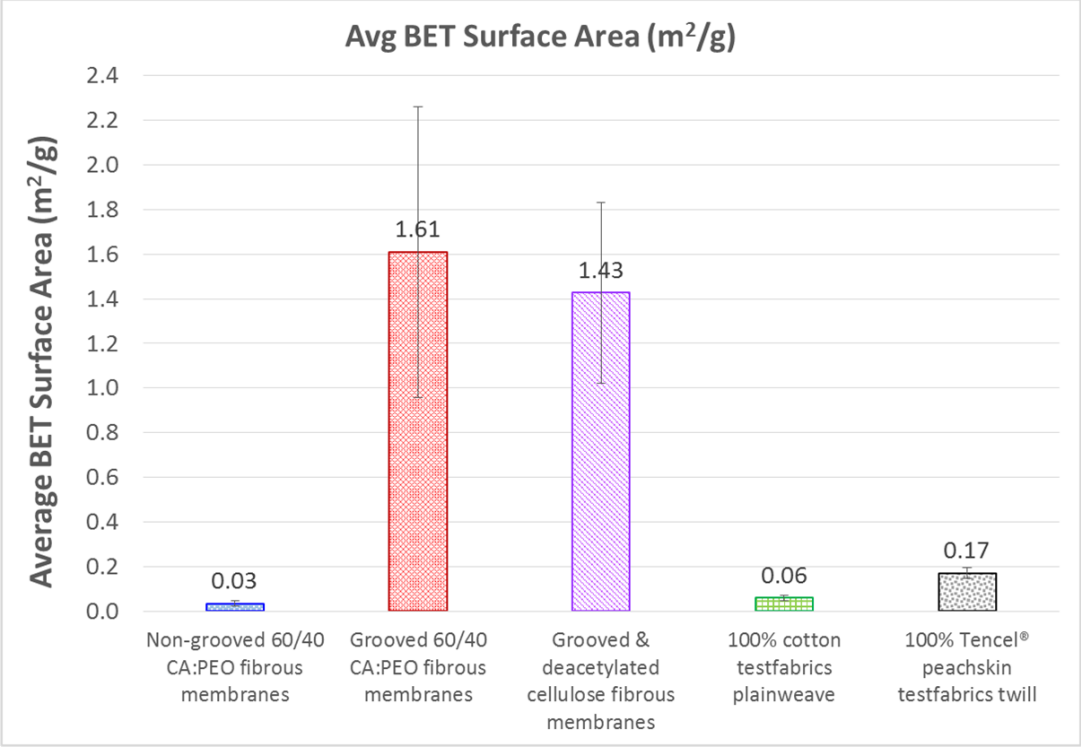

Figure 19: Multipoint krypton adsorption BET surface area (m^2/g) of the fibrous substrates

2.4.2.4. Mechanical Strength

While the fabrication of a grooved fiber morphology enhanced surface area of the fibrous membranes, it decreased the mechanical strength of the substrates. Shown in Figure 20, is the mean load at break and standard deviation for each substrate. The non-grooved fibrous membranes have the highest tensile strength while the tensile strength of grooved cellulose acetate membranes is lower, and the tensile strength of the grooved cellulose membranes is the lowest ($p < 0.05$). Since the thickness and weight of the fibers were controlled in these experiments, these results indicate that the higher surface area grooved fibrous membranes result in poor mechanical strength due to their morphology. This would have implications on the durability of the protective apparel application for which these fibers are designed. In general, though electrospun membranes are mechanically weak, and even the tensile strength of the non-grooved fiber would not be suitable for a durable application unless incorporated into a multilayer matrix that offered mechanical support.

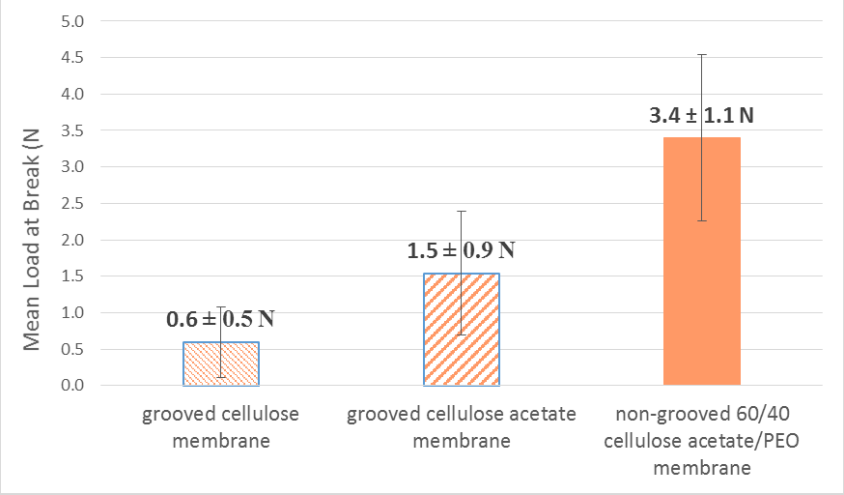

Figure 20: Instron tested mechanical strength of grooved and non-grooved membranes

2.4.2.5. Moisture Vapor Permeability (WVP)

Although the grooved morphology did not exhibit high tensile strength, it did result in achieving the highest moisture vapor permeability (794 ± 24.9 g/m^2/day) of all the fibrous substrates tested (also see results analysis in Chapter 3). A paired t-test comparing the WVP of the grooved and non-grooved fibrous membranes was performed to analyze statistical significance. Due to the high variance in WVP observed for the non-grooved fibrous membranes (775 ± 53.4 g/m^2/day), this result was not statistically significant ($p > 0.05$) relative to the non-grooved morphology. However, it can be stated that the electrospun fibrous membranes both grooved and non-grooved achieved statistically higher water vapor permeabilities than any of the other substrates tested (see Chapter 3) and were statistically higher than that of cotton (729 ± 15.5 g/m^2/day). Relative to cotton ($I = 100$), the water vapor permeability indexes (I) of the grooved cellulose acetate fibers and the non-grooved fibers was 109 and 106 respectively. Since higher water vapor permeability and a higher water vapor permeability index is correlated with higher breathability, it is evident that the electrospun fibrous membranes are the most breathable substrates tested in this work.

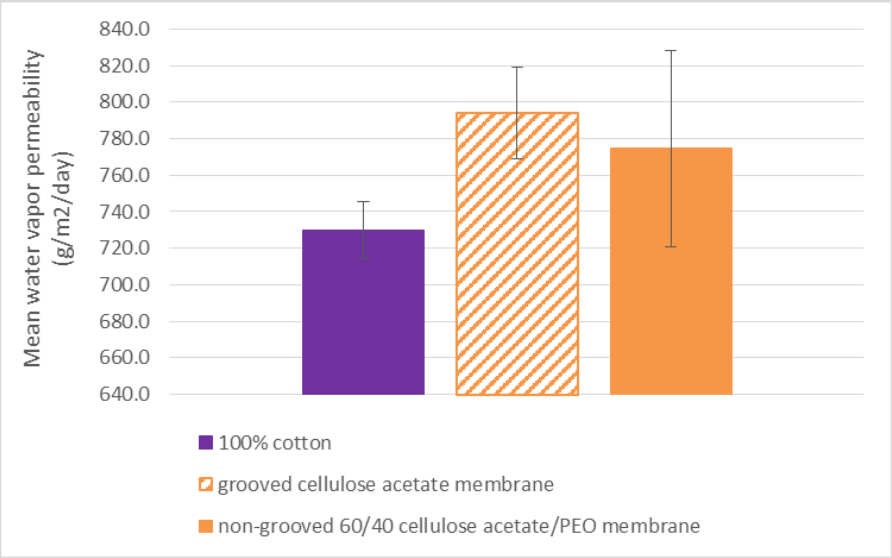

Figure 21: The water vapor permeability of the electrospun membranes relative to cotton

It is unclear why the WVP variance was high for the non-grooved membranes. Figure 22 illustrates how the average percent moisture mass loss of each substrate tested exhibited an almost linear relationship with time as one would expect since the evaporation rate of water from the cup should be constant under standard conditions. It is possible that some of the water in the metal test cup was sloshed when it was lifted to weigh or re-placed on the rotating turntable after weighing. Water vapor permeability will be investigated further in future work.

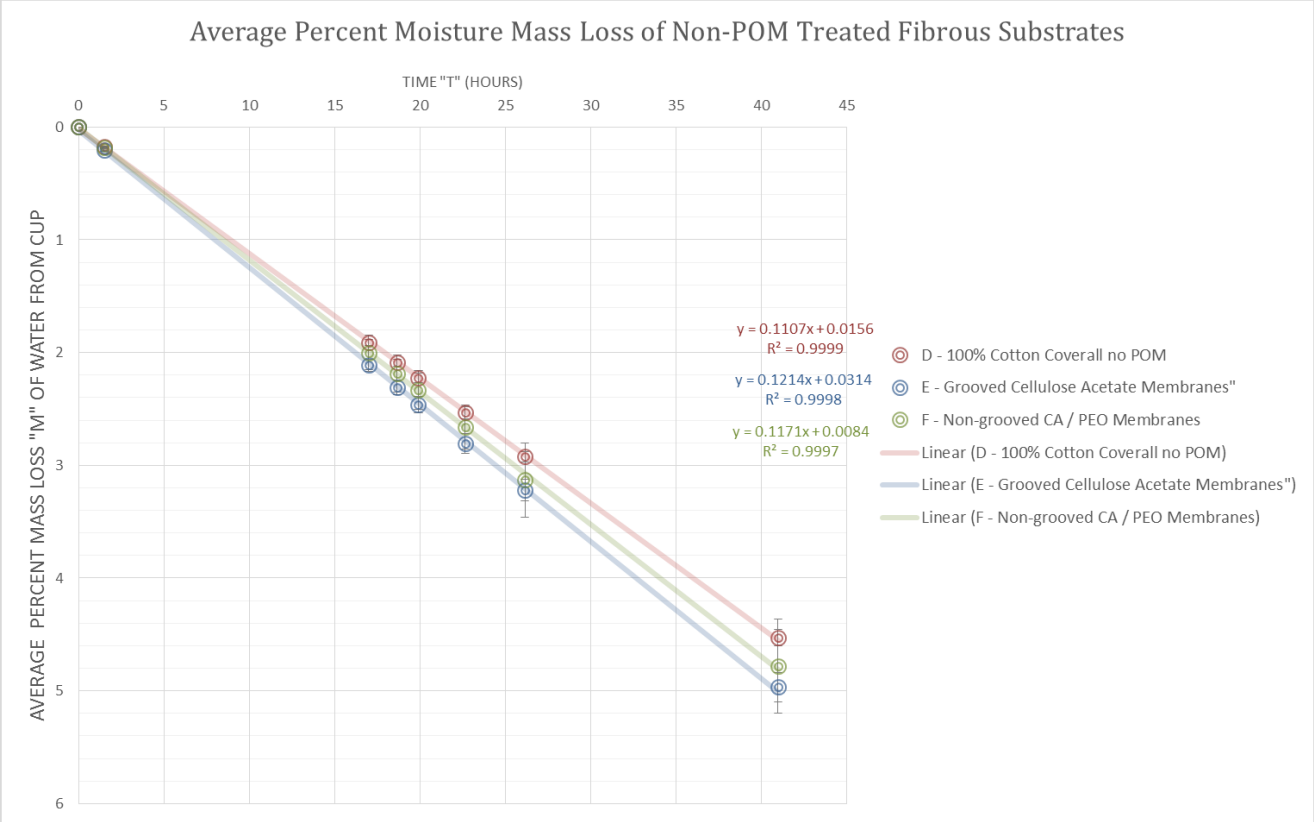

Figure 22: WVP: The Relationship between Mass Loss (M) of water from the cup with time

2.4.3. Characterization of $H_5PV_2Mo_{10}O_{40}$ Treated Fibrous Substrates

2.4.3.1. FTIR

When hexamethylene diisocyanate (HMDI) (liquid) was analyzed via FTIR, major peaks were observed at 2260, 1660, 1160, 1040, 860, and 573 cm^{-1}. The spectrum of HMDI indicated several functional groups that are similar to that of the POM powder; however, it was apparent that a peak at 2260 cm^{-1} was unique only for HMDI as seen in Figure 23 (c). Examining the literature, it was found that nitrile group bond interactions may be identified from the FTIR spectrum in the triple bond region of 2300-2000 cm^{-1}. For isocyanates, a type of alkyl nitrile functional group, FTIR absorption bands are typically seen in the 2275-2240 cm^{-1} region of the spectrum. A peak at 2260 cm^{-1} or 2240

cm^{-1} may correlate to the presence of saturated alkyl nitrile bond interactions [54,56]. This peak at 2260 cm^{-1} was used as the reference peak to indicate the presence of the HMDI, and the resulting spectrum was used as a standard of comparison when analyzing the POM grafted electrospun membranes.

As discussed previously, 1160 and 1060 cm^{-1} were chosen as defining peaks for the molybdovanadate POM since these peaks corresponded well to the P-O and Mo-O, and functional group interactions as well as the M-O-M vibrations [9,14,53,54,58,62,67]. Further evidence that the POM was present on the surface of the membranes included the presence of peaks and bands at 1650, 958, 768, and 600 cm^{-1} [9,14,53,54,56,58,61,62,70].

It was difficult to detect the full reaction of HMDI with POMs for the POM grafted membranes in Figure 23 (d) since the bands that resulted from the presence of the POM in the range of 2200-3600 cm^{-1} appeared to have obscured the HMDI band at 2260 cm^{-1}. The strong, broad bands seen at 1640, 2240, 3200, 3537, and 3590 cm^{-1} in the spectrum of the POM grafted HMDI functionalized membrane are likely due to residual lattice water commonly found in the structure of the POM [70]. This observation can be correlated with the presence of the bands at 1640, 2240, 3200, 3537, and 3590 cm^{-1} in the spectrum of the POM powder control.

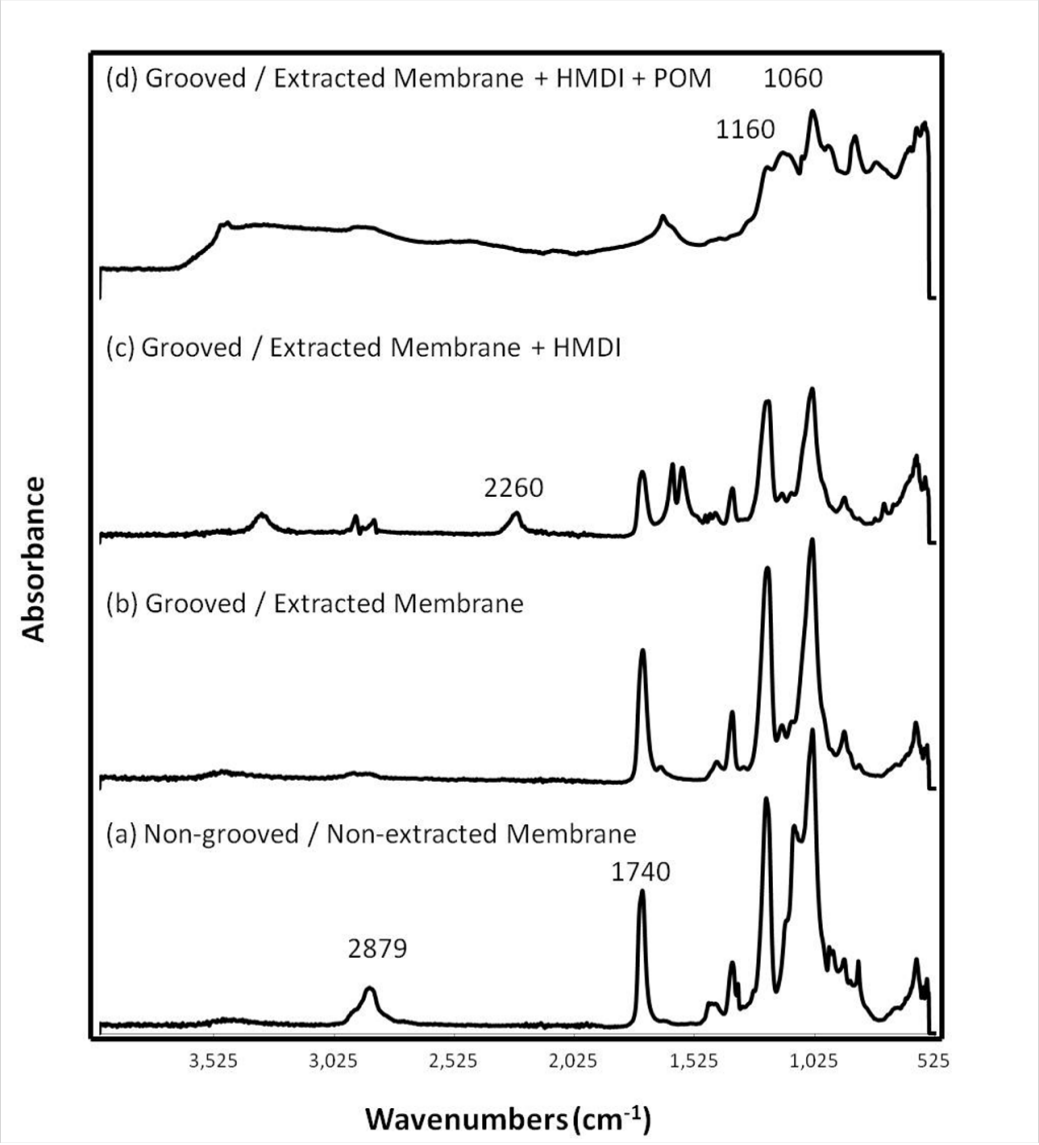

Figure 23: FTIR Absorbance of the (a) Non-grooved / Non-extracted 60/40 CA:PEO fibrous membranes, (b) Grooved / Extracted cellulose acetate fibrous membranes, (c) Grooved / Extracted cellulose acetate fibrous membranes grafted with HMDI, and (d) Grooved / Extracted cellulose acetate fibrous membranes grafted with HMDI and the POM $H_5PV_2Mo_{10}O_{40}$

When POM-immobilized substrates (Functionalization Method – 2) were analyzed using FTIR analysis, they were compared to the control spectrum of APTS (Figure 24) run in its liquid form. Two key peaks at 1092 and 773 cm^{-1} were chosen as APTS identifiers as they correspond well to examples in the literature, which identifies an absorption peak at 1092 cm^{-1} that is characteristic of the methoxy groups Si-O-CH and states that the peak at 773 cm^{-1} is assigned to the silane carbon bonds, Si-CH. While POM-functionalized substrate spectrums made the peak at 773 cm^{-1} difficult to detect due to POM peak overlaps, a distinct peak was present at 1092 cm^{-1} for all samples functionalized with APTS [71,72] .

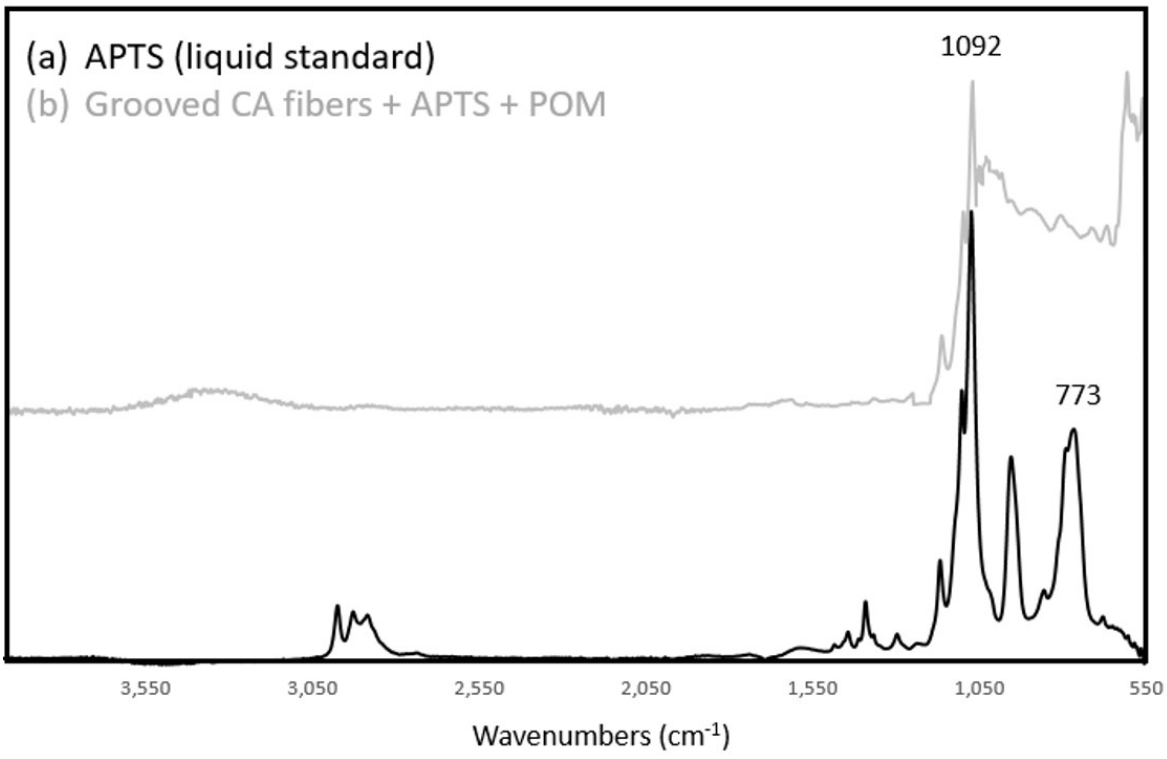

Figure 24: FTIR characterization of (a) (3-Aminopropyl)triethoxysilane (APTS) in liquid form and (b) grooved fibrous membranes functionalized with APTS + POM via POM-immobilization

2.4.3.2. SEM

Figure 25 (a) shows images obtained via scanning electron microscopy of the grooved cellulose acetate fibrous membranes prior to POM grafting, while Figure 25 (b) shows the grooved cellulose acetate fibrous membranes after being grafted via Functionalization Method 1 with POM particles evident on the surface of the fibers forming a mono layer. No seeding was observed. Further investigation of the amount of POM in the monolayer will be addressed in future work.

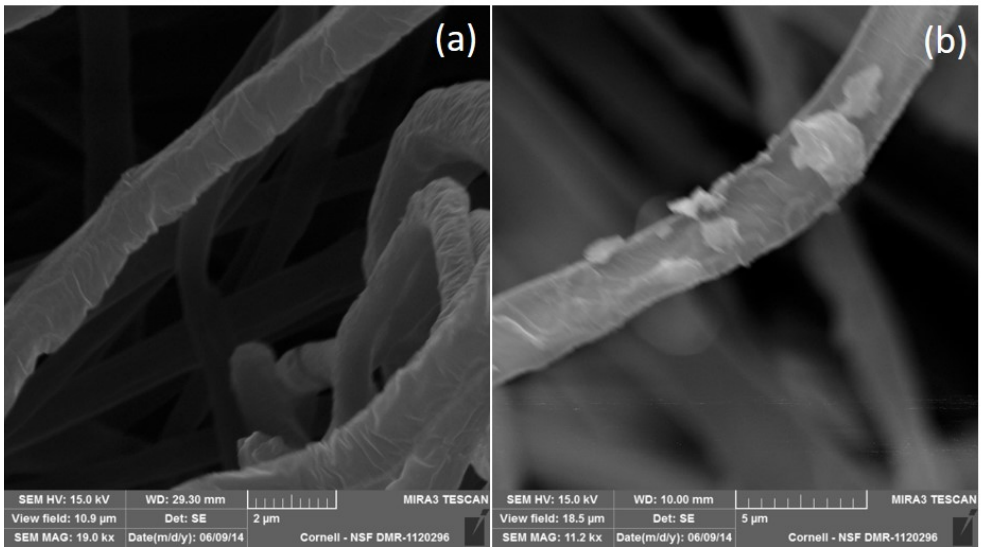

Figure 25: (a) Grooved cellulose acetate fibrous membranes prior to POM grafting (b) Grooved cellulose acetate fibrous membranes after POM grafting (M1)

Figure 26 (a) shows images obtained via scanning electron microscopy of the grooved cellulose acetate fibrous membranes after POM treatment via Functionalization Method 2 (POM-immobilization) (M2), while (b), shows cotton after POM treatment via Functionalization Method 2 (M2). ImageJ analysis indicates that more functionalized POM can be found on the surface of the grooved cellulose acetate fibers than on the cotton offering evidence to the hypothesis that higher surface area substrates are able to achieve

higher POM loadings. A mono layer of POM particles is evident on the surface of the fibers and will be investigated further in future work. No seeding was observed.

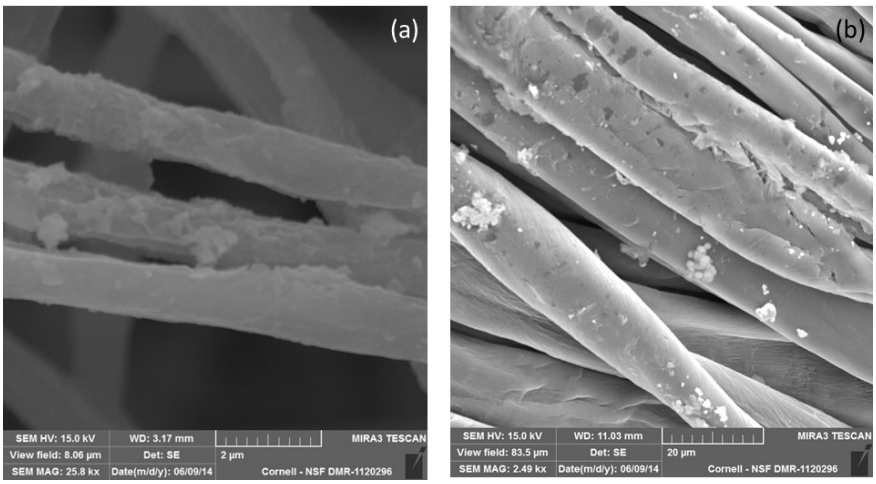

Figure 26: (a) Grooved cellulose acetate fibrous membranes after POM-immobilization (M2) (b) Cotton after POM-immobilization (M2)

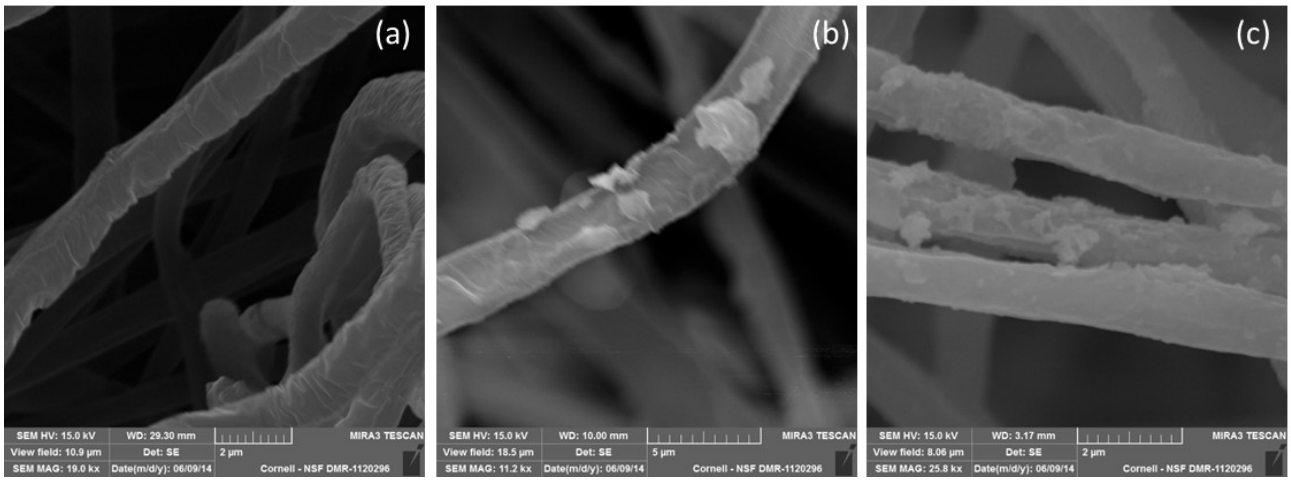

Figure 27: (a) Grooved fibers – No POM functionalization, (b) Grooved fibers – POM grafting (M1), (c) Grooved fibers – POM-immobilization (M2)

By comparing the amount of POM functionalized to the grooved cellulose acetate fibers in Figure 27 (b) via POM-grafting to the amount of POM functionalized to the grooved cellulose acetate fibers via POM-immobilization in Figure 27 (c) using ImageJ analysis, no significant difference in POM loading was detected. This suggests that the two POM functionalization methods may result in analogous amounts of POM loading on fibrous substrates.

2.4.3.3. TGA

Thermogravimetric weight loss analysis was used to measure the amounts of POM attached to the substrates (Figure 28). The greatest POM percent add-on by weight of substrate occurred for the high surface area grooved electrospun cellulose acetate fibers (16.3 ± 3.3 % POM add-on via POM grafting i.e. Functionalization Method 1 "M.1") and grooved electrospun cellulose fibers (13.7 ± 1.4% POM add-on via POM immobilization i.e. Functionalization Method 2 "M.2").

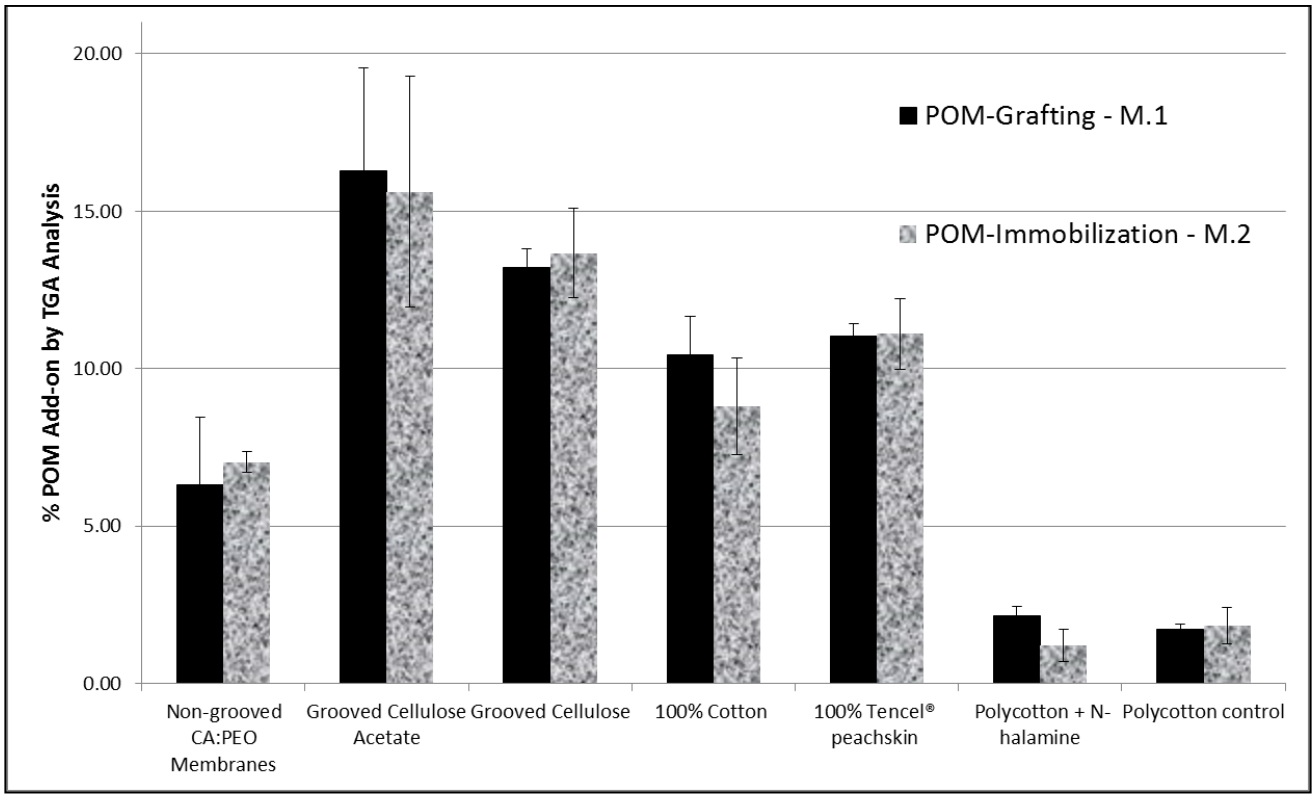

Figure 28: TGA weight loss analysis: amount of POM functionalized to fibrous ssubstrates

These amounts of POM percent add-on for grooved cellulose acetate and cellulose were significantly higher ($p < 0.05$) than those achieved for the lower surface area non-grooved electrospun cellulose acetate / polyethylene oxide fibers (6.3 ± 2.1% POM via M.1 and 7.0 ± 0.3% POM via M.2) and 100% cotton fibers (10.4 ± 1.2% POM via M.1 and 8.8 ± 1.5% POM via M.2). One-way ANOVA statistical analysis of the TGA weight analysis measurements of the non-grooved and grooved fibrous membranes showed that the difference in surface area between the grooved and non-grooved treatments was statistically significant with a p-value of 0.0004. The substrates with the least amount of POM functionalized via either method were the N-halamine-treated polycotton and the polycotton control. These results correlate to the surface areas of the substrates indicating

that increasing the amount of substrate surface area will increase the amount of achievable POM attachment up to a point. This relationship is illustrated in Figure 29.

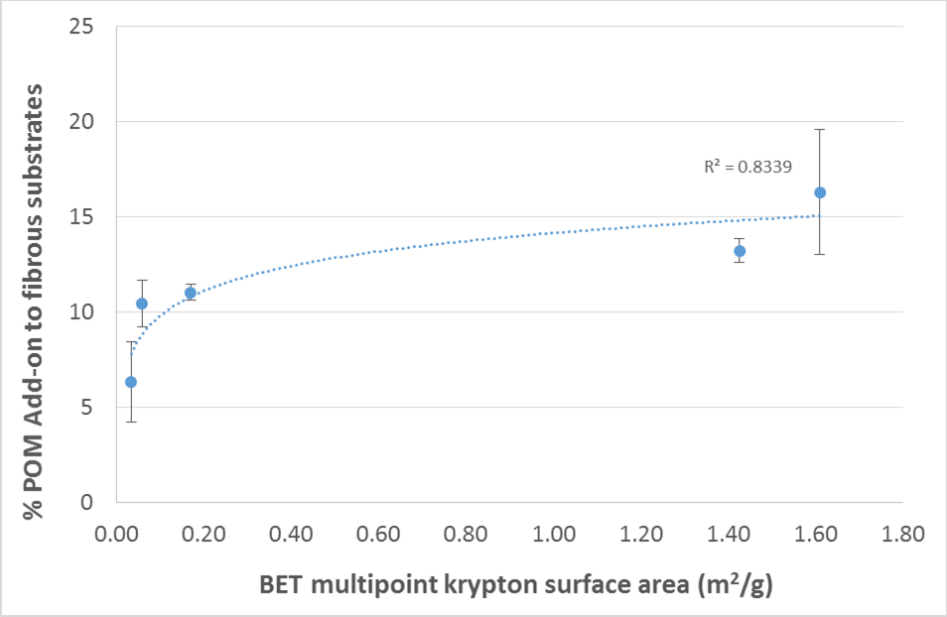

Figure 29: Relationship between substrate surface area and percent POM loading

Paired t-tests were used analyze the means of the M.1 and M.2 treatments of each type of substrate tested. While no statistical evidence discerns between the performance of one functionalization method over another for any of the substrates, these results do exhibit significant differences between fibers of grooved and non-grooved morphologies. In addition to their higher surface areas, the availability of reaction sites may also partially explain why cotton, cellulose, Tencel®, and cellulose acetate achieve high POM loadings than non-grooved cellulose acetate / polyethylene oxide membranes, pre-treated polycotton, or un-treated polycotton fabrics. It is significant to note that from this data one can see that the fabrication of grooved fiber morphology enhanced surface area and thus resulted in higher POM loadings on the substrate up to a point.

2.4.3.4. Capillary Flow Porometry

In Figure 30 the mean flow pore diameter shows no significant difference when POMs are functionalized to the fibrous substrates via either method – POM-grafting (M1) or POM-immobilization (M2). Also of note is that the grooved cellulose acetate membranes have a significantly ($p < 0.05$) smaller mean flow pore diameter (2.1 ± 0.4 microns) than the other substrates. This is likely due to the grooves, co-continuous channels, and through-pores that result from the selective dissolution of polyethylene from the cellulose acetate fiber matrix; and it is most likely this property that contributes to the high value for moisture vapor permeability of the grooved cellulose acetate. It is of note that functionalizing the substrates at their respective loadings using either method does not appear to block the pores of the substrate even for the grooved cellulose acetate substrate.

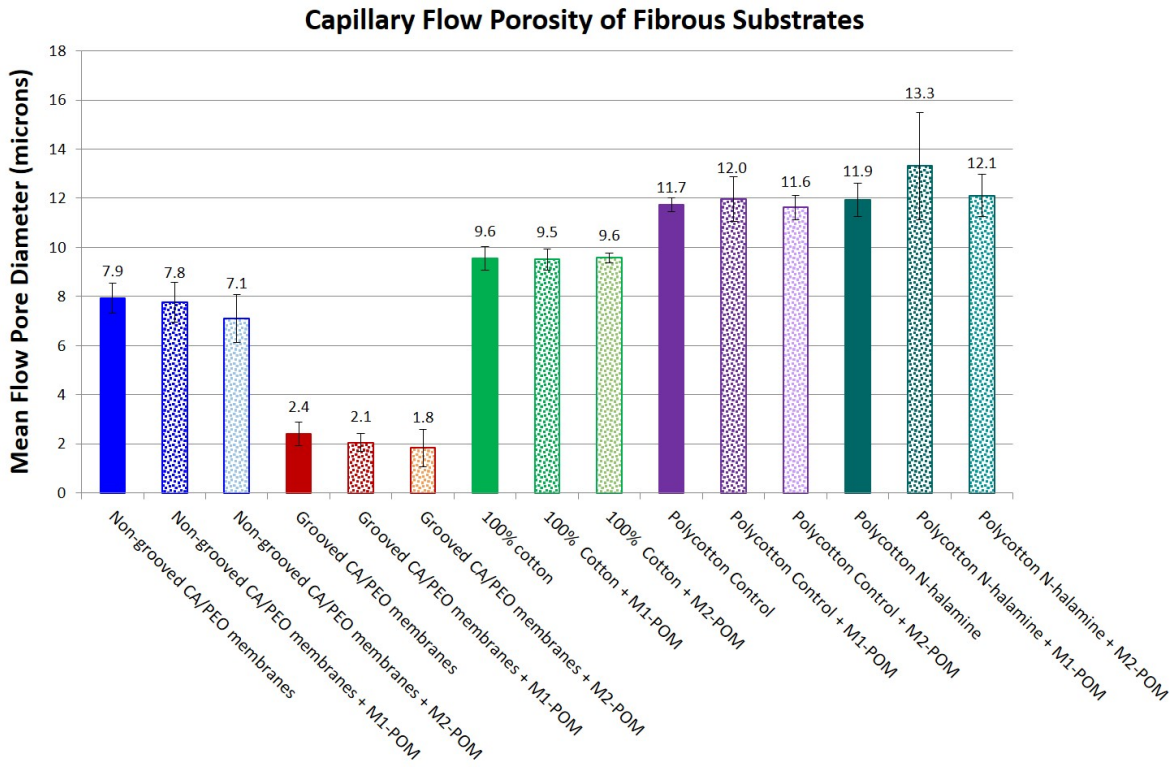

Figure 30: Capillary Flow Porosity of Fibrous Substrates Functionalized with POM-Grafting (M1) and POM-Immobilization (M2)

2.4.3.5. Laundry Durability

The mean change in weight percent POM-add-on for cotton substrates functionalized via POM-grafting (M1) was -2.3% ± 1.8 resulting in a residual mean percent add-on of 8.1% MI-POM on cotton after five wash cycles while the mean change in weight percent POM-add-on for cotton substrates functionalized via POM-immobilization (M2) was -1.7% ±1.8 resulting in a residual mean percent add-on of 7.1% M2-POM on cotton after five wash cycles. A paired t-test comparing the laundry durability of the two treatments M1 and M2 confirmed that these results are not statistically significant ($p = 0.38$) from each other. Furthermore, the difference between

these laundry durability results of the two treatments is well-within the range of error for TGA weight loss analysis. It is important to note that both methods of POM functionalization resulted in similar performance with narrower margins of error after laundering than before laundering. It is also important to note that POM was still consistently and uniformly present on the surface of the test specimens after five wash cycles. The data from the colorimetric analysis did not offer meaningful results. Colorimetric differences were seen on the swatches before and after testing, but it was attributable to the slight discoloration that occurred from using older metal bath test equipment on the Terg-O-Tometer. One swatch from the ballast of each load was selected at random and measured on the TGA to determine if the functionalized POM had disassociated in the wastewater and deposited on the other fabrics in the bath. However, no amount of POM was detected on the ballast swatches. The analysis on the UV-Vis spectrophotometer of waste-water aliquots to determine if POM was released to the bath without redepositing on the fabrics did not produce meaningful results as the absorption peak for the POM in dilute solution was obscured completely by the absorption peak for the detergent-water wash bath. Therefore, no conclusive results were generated from this test except that both methods (M1 and M2) demonstrated similar laundry durability performance with no statistical difference. The similarity in their durability performance implies that the mechanisms of POM functionalization via the two methods may be similar, and that no covalent bond is being formed between the substrates and the POM as was intended by the M1 POM functionalization methodology. However, this data also indicates that the mechanisms M1 and M2 for POM functionalization have some wash

durability even though POMs are readily soluble in water. These mechanisms of POM retention require further investigation in future work.

2.4.3.6. Possible Mechanisms of POM functionalization

The absence of a statistical difference in the TGA weight loss analysis, Capillary Flow Porometry, and Laundry Durability tests due to POM functionalization method suggests that the two mechanisms of functionalization (M1 & M2) may be similar.

Regarding the theory used to devise the POM-grafting (M1) functionalization methodology, hydrolysis-resistant R-O(POM) bonds, in the case of some vanadates, are known. Although M1 attempts to form a covalent bond between the cellulosic substrate and one of the isocyanate functional groups to form a POM(O)-(CO)-NH-(carbamate) unit, this work provides no evidence to confirm the presence of that linkage; nor is there evidence that such a linkage would be hydrolytically stable. If such a chemical linkage were to form, it could easily hydrolyze and reform the parent POM structure.

Several issues exist with the functionalization method M1, namely that the di-functional HMDI may be more prone to form linkages with cotton with both functional ends than to form only one linkage with the cotton and have one end of the isocyanate available for chemical bonding with one of the pendant oxygens of the POM. Since the POM FTIR spectrum obscures peaks that may indicate the presence or absence of this linkage, this method of characterizing M1 is not optimal. The challenge of achieving durable POM attachment to substrate surfaces is evident from the literature where durable POM binding methods are rarely presented. Many examples in the literature incorporate POMs into substrates simply by wetting, which provides no durable POM binding. Most papers that present a more durable linkage take the approach of forming a Si—O—Si

covalent bond between a Keggin POM and a silica substrate[44]. An additional method is to include the POM into a silica matrix via a sol-gel syntheses [73,74] . What may be the most likely mechanism for both of the functionalization methods reported here-in is a Keggin-type POM immobilization (Scheme 7) via the formation of an amine shown in Scheme 12. This could be a plausible mechanism of the M1 functionalization method as isocyanates are frequently used to synthesize primary amines via hydrolysis. Hydrolysis of the carbamate unit would produce an amine, that could be protonated at neutral pH and thus electrostatically retain the $[PV_2Mo_{10}O_{40}]^{5-}$.

Scheme 11: Hydrolysis occurs in a two-stage reaction:

(1) $RNCO + H_2O \rightarrow RNHCO_2H$;

(2) $RNHCO_2^- + H^+ \rightarrow RNH_2 + CO_2$. [72, 75]

This may be what is occurring when the HMDI is in the presence of the POM. If this is the case, then both M1 and M2 are mechanisms of POM-immobilization, and may result in similar characterization performance as demonstrated in this work. Some variance may exist between the two methods if the POM is not remaining intact after immobilization. Kholdeeva notes that mechanisms of catalysis by homogeneous and supported POMs do not tend to differ if the structure of the POM remains intact after immobilization [47]. This proposed mechanism will need to be investigated further in future work.

Given the important role that fiber morphology, surface area, and pore size has played in this research, it is also possible that a mechanism of particle retention is responsible for the performance of the POM-functionalized substrates. This mechanism

can be explored in future work by calculating the amount of POM in the monolayer on the fiber using SEM ImageJ analysis of POM-treated substrates.

2.4.4. Decontamination of Methyl Parathion by POM Functionalized Fibrous Membranes/Textile Substrates

Degradation of methyl parathion was observed when POMs were grafted or immobilized on the fibrous substrates. No methyl parathion degradation was observed on non-POM treated materials. Figure 28 represents the decontamination performance of the POM grafted & POM-immobilized grooved cellulose acetate and non-grooved 60/40 CA:PEO membranes after 24 h. It shows that the grooved membranes with the higher surface area degrade significantly more methyl parathion than the non-grooved fibers. This is the case for both POM-functionalization methods. Controls of grooved and non-grooved fibrous membranes that were not grafted with the POM and exposed to methyl parathion for 24 hours and 1 week showed no degradation. Using the equation derived from the calibration curve of methyl parathion, it was determined that the non-grooved fibrous membranes treated with POMs resulted in a 17% decrease in the concentration of methyl parathion present in the methyl parathion / hexane solution after 24 h while the grooved cellulose acetate fibrous membranes treated with POMs resulted in a 25% decrease in the concentration of methyl parathion present in the methyl parathion / hexane solution after 24 h. In terms of the amount of methyl parathion degraded by the POM, this translates to a decrease from 0.32 mg of methyl parathion in hexane solution to an amount of 0.26 mg of methyl parathion in the hexane solution as a result of POM grafted non-grooved fibers and 0.24 mg of methyl parathion in the hexane solution as a result of POM

grafted grooved fibers after 24 h. No statistical difference exists between the two functional methods ($p > 0.05$).

After 1 week (168 h), differences in the degradation performance between grooved and non-grooved fibers became more distinct. It was determined that the non-grooved fibers covalently treated with POMs resulted in an 89% decrease in the concentration of methyl parathion present in the methyl parathion / hexane solution after 168 h while the grooved fibers treated with POMs resulted in a 100% decrease in the concentration of methyl parathion present in the methyl parathion / hexane solution after only 5 days (120 h). In terms of the amount of methyl parathion degraded by the POM, this translates to a decrease from 0.32 mg of methyl parathion in hexane solution to an amount of 0.04 mg of methyl parathion in the hexane solution as a result of POM-functionalized non-grooved fibers after 7 days and 0.00 mg of methyl parathion in the hexane solution as a result of POM-functionalized grooved fibers after 5 days. Therefore, the grooved fibers achieved a greater amount of methyl parathion degradation than the non-grooved fibers in a shorter amount of time. This difference in performance between electrospun fibers of the same diameter and cross-sectional shape can be attributed to the rougher surface morphology of the grooved fibers. Statistical analysis showed that the amount of degradation of methyl parathion by the grooved membranes was statistically significant with a p-value of 0.001. These results confirm the hypotheses that increasing the surface area of the substrate leads to an increase in POM binding sites that results in improved decontamination performance.

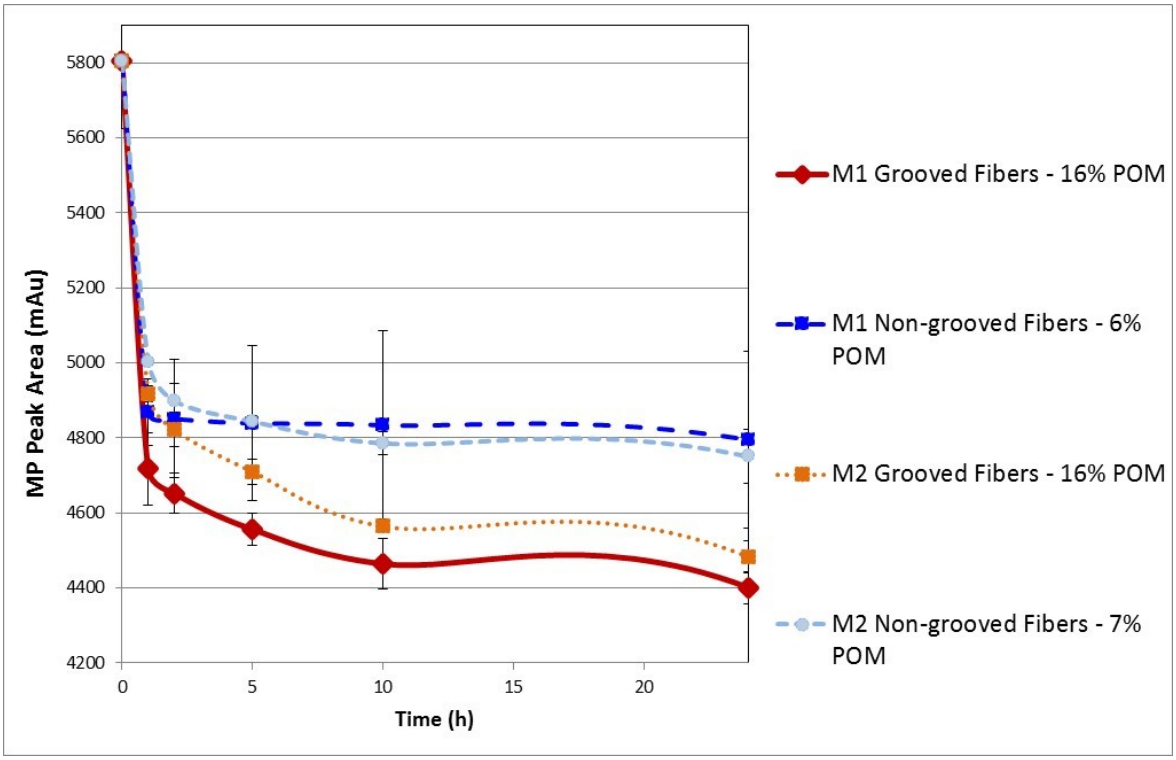

Figure 31: Degradation of methyl parathion by POM grafted (M1) and POM-immobilized (M2) non-grooved 60/40 CA: PEO fibrous membranes and grooved cellulose acetate fibrous membranes after 24 h

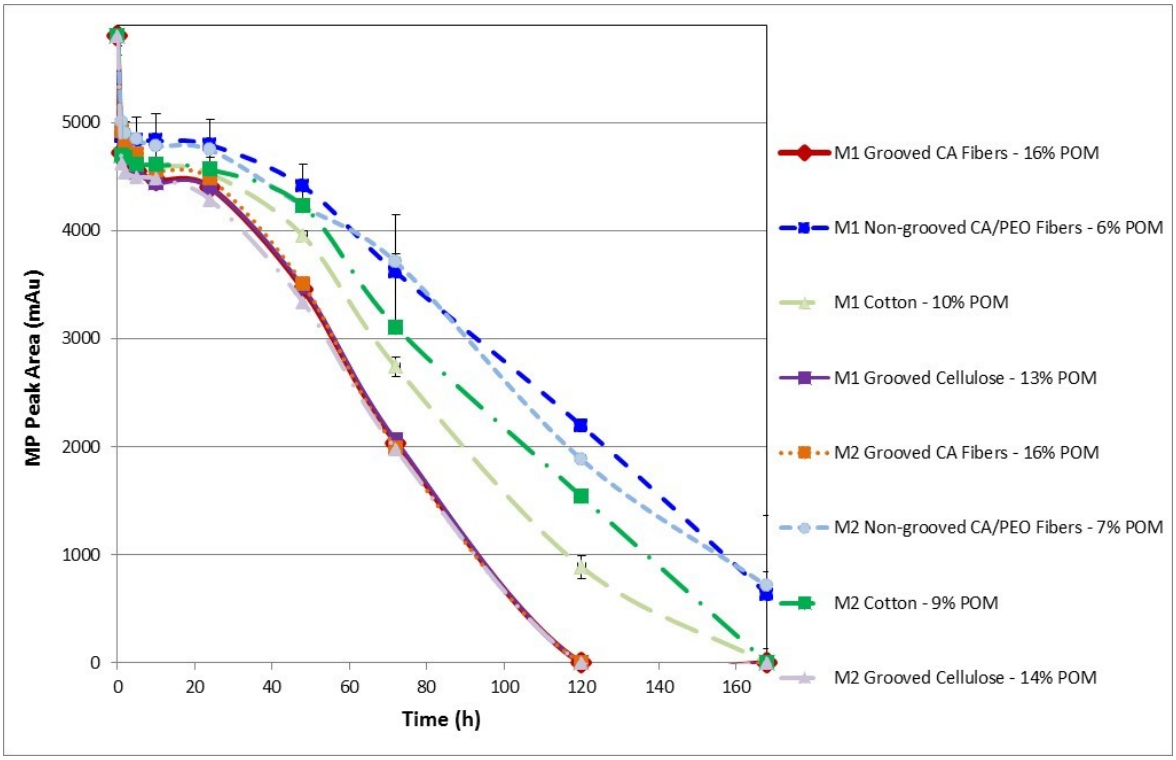

Figure 32 (a): Degradation of methyl parathion by POM grafted (M1) and POM-immobilized (M2) substrates [grooved cellulose acetate (CA) fibrous membranes, non-grooved cellulose acetate / polyethylene oxide (CA/PEO) fibrous membranes, 100% cotton, and grooved cellulose fibrous membranes] after 1 week

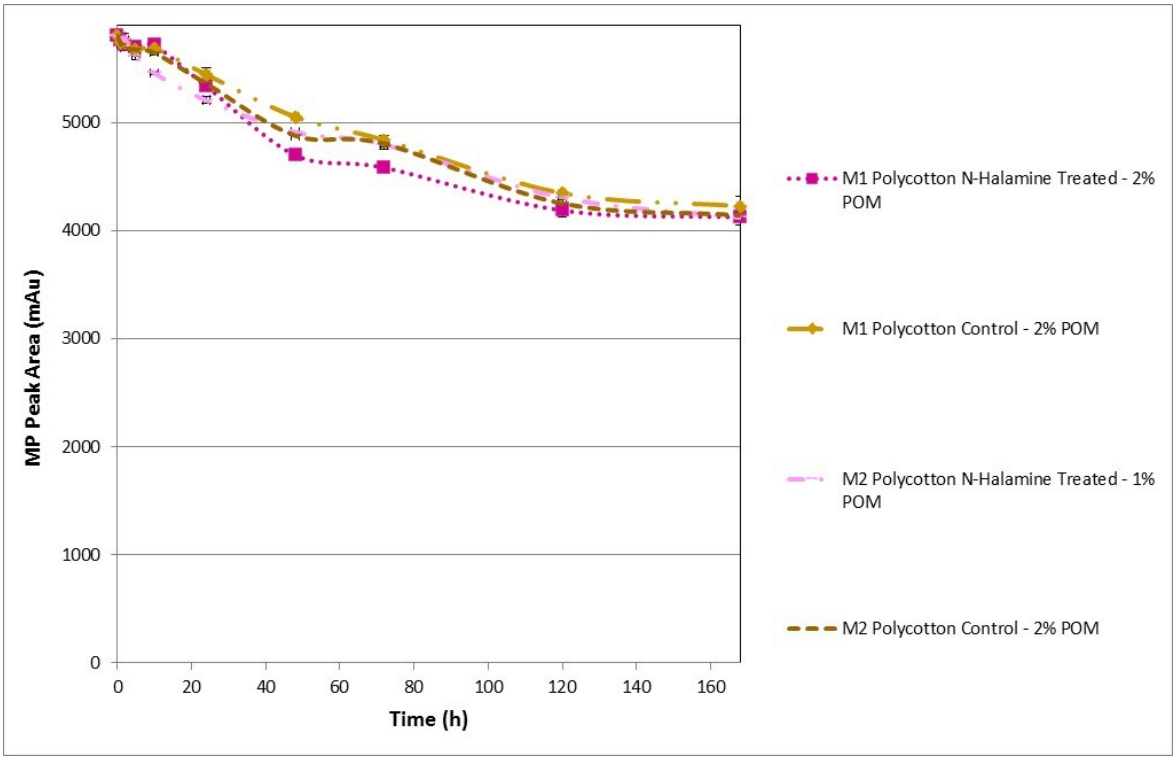

Figure 32 (b): Degradation of methyl parathion by POM grafted (M1) and POM-immobilized (M2) substrates [55/45 cotton polyester + N-halamines and 55/45 cotton polyester control] after 1 week

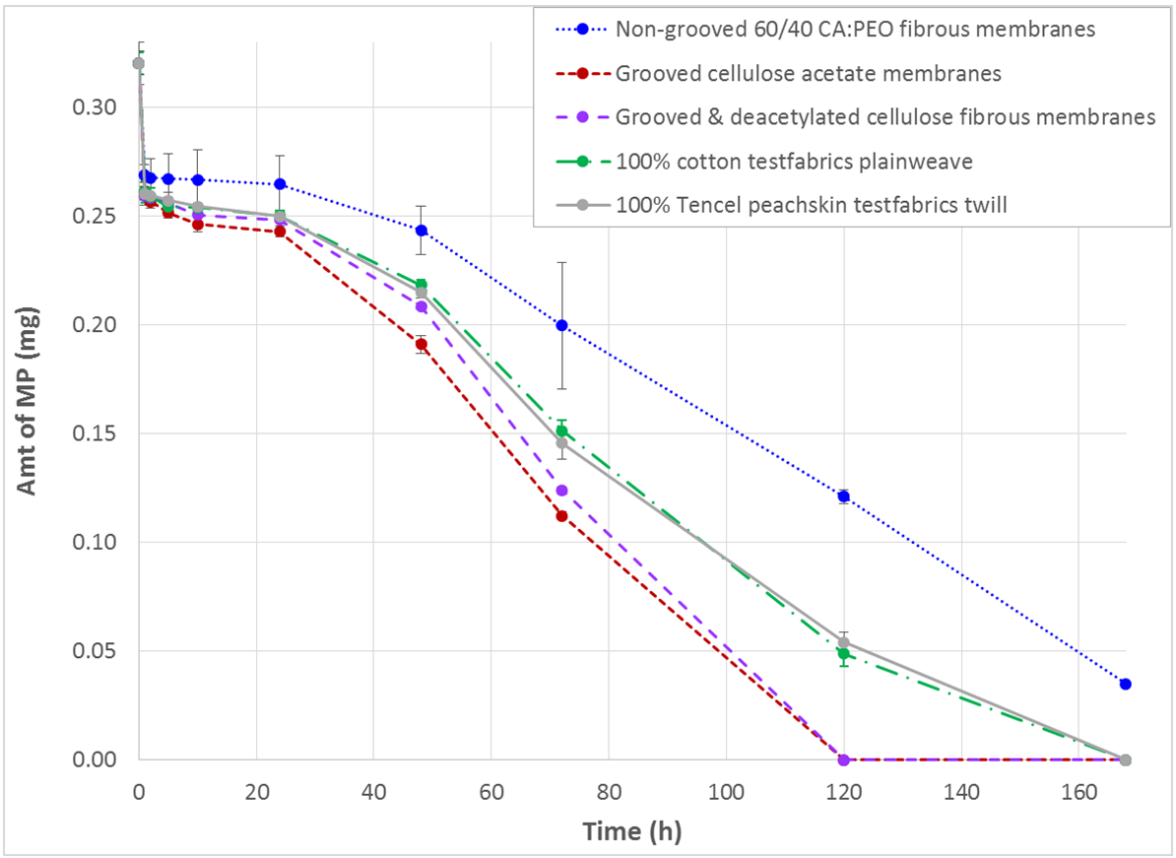

Figure 32(c): Amount in milligrams of methyl parathion degraded by POM grafted (M1) and POM-immobilized (M2) substrates [grooved cellulose acetate (CA) fibrous membranes, non-grooved cellulose acetate / polyethylene oxide (CA/PEO) fibrous membranes, 100% cotton, grooved cellulose fibrous membranes, and Tencel®] after 1 week

Figures 31, 32 (a), and 32 (c) illustrate that the degradation results of methyl parathion by functionalized grooved cellulose membranes were comparable to the performance of the grooved cellulose acetate membranes achieving complete toxin degradation after five days. The fiber diameter of the grooved cellulose fibers was between 1 and 2 microns and thus the same as the grooved cellulose acetate fibers and the non-grooved counterparts, thereby

illustrating that the grooved morphology of the fiber surface was the greater impact factor for increasing the methyl parathion degradation performance. The degradation of methyl parathion by the functionalized cotton fabric and Tencel® fabric was statistically insignificant ($p = 0.61$) from each other, but slightly greater than that by the non-grooved fibers ($p = 0.0002$). Although the fiber diameters of the cotton and Tencel® substrates (both between 10 and 20 microns) were much greater than the fiber diameters of the electrospun membranes, the surface areas of the cotton and Tencel® fabric were not so much greater than that of the non-grooved membrane. Nevertheless, Cotton and Tencel® achieved higher percent POM loadings than the non-grooved membranes due to their complete cellulosic composition with more reaction sites for POM-grafting and POM-immobilization than the non-grooved cellulose acetate / polyethylene oxide blend. Figure 32 (b) shows that the polycotton substrates whether treated with N-halamines or un-treated, resulted in significantly less methyl parathion degradation than all other substrates. N-halamine-treated polycotton did not degrade more methyl parathion than its respective control ($p > 0.05$). This may be due to subsequent steps in the POM-functionalization processes (M1 and M2) that deactivated the N-halamine treatment. These results suggest that chemical composition yielding the most available POM binding sites in combination with the high surface area grooved fiber morphology enables the largest amount of POM loading per gram of fabric and thus the greatest amount of methyl parathion degradation. This relationship that relates higher POM loadings to higher amounts of methyl parathion degradation is illustrated in Figure 33, which shows that at each time interval, substrates with greater POM-loading result in a greater decrease in the HPLC peak area for methyl parathion thus signifying greater methyl parathion degradation.

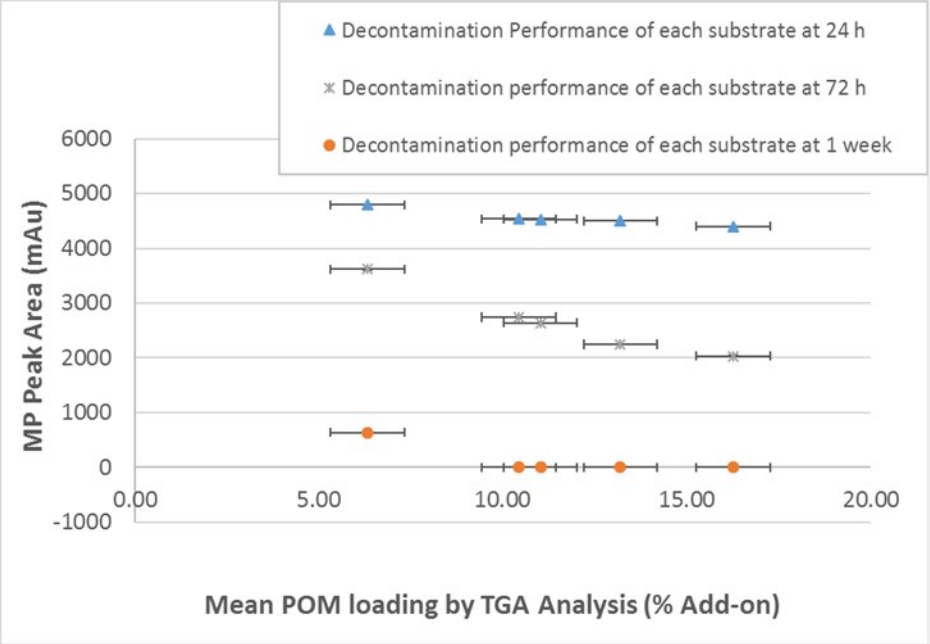

Figure 33: Relationship between substrates with higher POM loadings that results in higher amounts of methyl parathion degradation

In summary, a higher surface area substrate such as the grooved cellulose acetate fibers or the grooved cellulose degraded more methyl parathion than a lower surface area substrate such as the non-grooved 60/40 CA:PEO fibers, cotton, or Tencel®.

Regarding the degradation of methyl parathion and the expected degradation products of p-nitrophenol and methyl paraoxon, no peaks for degradation products were detected in the HPLC-DAD results. For each degradation test, the standard solution of p-nitrophenol in water showed a peak at 320 nm with a 5 min retention time, and the standard solution of methyl paraoxon in hexane showed a peak at 280 nm at a 5 min retention time. The standard solution of methyl parathion showed a peak at 320 nm with a retention time of 16 min. Over the time of degradation testing, the peak area of the methyl parathion decreased at the 16 min retention time; however, no peaks were apparent at 280

nm or 320 nm with 5 min retention times indicating that the expected degradation products were not present as the amount of methyl parathion decreased over time for the POM-treated samples. This may indicate that the POM completely mineralized methyl parathion and its degradation products, although future studies will need to examine this further. No decrease of methyl parathion peak was observed when non-POM-treated control substrates underwent degradation testing. It is possible that methyl parathion was degraded via hydrolysis rather than catalytic oxidation [18,21,22]. However, degradation of methyl parathion by hydrolysis would have also produced the degradation product of p-nitrophenol and a second degradation product, diethylthiophosphate. If the expected degradation products were mineralized, ion chromatography could be used to in future work to further examine and quantify the degradation results of the POM treated substrates.

CHAPTER 3

FABRICATION & CHARACTERIZATION OF POLYOXOMETALATE-FUNCTIONALIZED COVERALLS

3.1 Introduction

3.1.1. Personal Protective Apparel for Agricultural Workers

Often exposed to extreme environmental conditions of heat and humidity and pesticides with adverse health effects, agricultural workers must wear protective clothing that is both breathable and inhibits toxin adsorption. The most protective PPE provides impenetrable barrier protection from pesticides, but this same property that effectively protects the wearer from toxins, prevents moisture vapor, i.e. perspiration, from evaporating through apparel. This contributes to dangerous levels of physiological heat stress for workers, endangering their health and limiting their productivity. The use of semi-permeable barrier materials in protective coveralls could aid in providing protection and comfort, although contamination of surfaces and skin often occurs when protective clothing is doffed or laundered. Therefore, a solution must be developed that provides protection, breathability, *and* self-decontamination. This work attempts to meet that need by developing breathable protective coveralls functionalized with catalytic polyoxometalates. Not only are polyoxometalates self-decontaminating upon exposure to ambient air, but also, their catalytic nature enables them to self-regenerate after each decontaminating cycle, making protective apparel functionalized with POMs re-useable. Clerici and Kholdeeva observed that the catalytic activity of POMs is well retained for at least five cycles [47]. Unlike other protective materials, such as activated carbon, that rely on the finite absorption of toxins, which are then permanently embedded in the clothing,

self-cleaning POM-functionalized ensembles may not require hazardous waste disposal depending on the toxicity of degradation products.

Given the everyday usage of agricultural protective coveralls in outdoor farming environments, the materials must be simple and inexpensive to manufacture, cheap to purchase, and offer good wear and laundry durability. This work is part of a HATCH project funded by the Department of Agriculture, which is designed to improve the well-being of agricultural workers and their families.

3.1.2. Incorporation of Self-decontaminating Materials in Protective Fibrous Substrates

POMs incorporated in fibrous substrates have been examined for applications in wastewater and air filtration as well as protective apparel [25,27,76]. Physical or chemical functionalization of fibrous substrates with POMs can be achieved as was demonstrated in Chapter 2 of this work [25]. Briefly examined in this work, N-halamines are another "self-cleaning" technology, which can be incorporated into protective garment fiber matrices as means to decontaminate fabrics once they're exposed to chemical and biological threat substances [77]. Oxidative organic polymers such as N-halamines, so termed for their chloramines bonds (N-Cl) can be incorporated into nanofibrous web membranes to self-detoxify liquid or vapor CB agents such as HD, GB, Lewisite, and VX on protective garment surfaces [78]. Their detoxification efficiency is due to the disassociation of the chloramines bonds [79] thus oxidizing contaminants and thereby converting alcohols to ketones, sulfides to sulfoxides and sulfones, and cyanides to carbon dioxide and water [80]. There are three forms of chloramines bonds: amides, imides, and amine halamines [79]. Polyacrylamidoxime, known as PANOx or PAAO, contains both an ionizable amide (NH_2) and an oxime (C=NOH) which react readily with organophosphate nerve agents. α-

Nucleophiles such as hydroxylamine, hydrazine, anions of hypochlorite, hydroxamic acids, oximes, iodosobenzoates, and hydroperoxides are known to degrade organophosphates (OPs) with a lone pair of electrons on the atom adjacent to the attacking atom. However, primary amines and imines can also degrade OPs via the S_N2 mechanism of base catalysis [81]. Additional advantages of N-halamines range from their known antimicrobial properties [82], to their ability to be regenerated if treated with halogen releasing agents such as chlorine bleaches, to their ability to decontaminate surfaces over a broad pH range, as well as their ability to be incorporated into multiple types of fabric such as polyester, as seen in this work where an N-halamine-treated 55/45 cotton / polyester fabric was provided by Dr. Gang Sun of the University of California, Davis. This versatility makes them well suited for use in a broad range of applications including an agricultural chemical protective coverall [78]. Since high moisture regain, low evaporative resistance, and high moisture vapor permeability are closely linked to the perceived comfort of fabrics, the use of POMs alone and POMs combined with other protective technologies like N-halamines in cellulose-based protective apparel may help bridge the gap between protection and comfort.

3.1.3. Understanding Thermal Comfort

According to ISO 7730, "thermal comfort" is defined as the "condition of mind which expresses satisfaction with the thermal environment"[83,84]. The human skin is the interface between the human body and the environment, and detects temperature changes and mechanical or chemical attacks, thus it is important to understand its properties when assessing the thermal comfort of breathable chemical protective apparel. The temperature of skin in conditions of thermal comfort is 31 - 36.5°C [85]. Heat is emitted from the

skin's surface in convective currents and is radiated to cooler environments as well as being conducted through air layers; ten percent of that heat is lost to evaporation, and ten percent is lost to respiration. Air around the skin acts as an insulator [84,86]. Thus there are many factors to consider when assessing comfort properties as shown in equation 2 representing Heat Balance where H is the heat production, M is metabolism, W is work, E is evaporation, K is conduction, C is convection, R is radiation, and S is the storage of heat [84].

$$H\left[\mathrm{W_m}^{-2}\right] = M \pm W = H = E\ (\pm K \pm C \pm R) \pm S \quad [2]$$

If heat balance is not achieved, thermo-physiological or sensorial discomfort is experienced meaning the body feels uncomfortable i.e. cold, hot, itchy, tight, wet, or other qualitative descriptors of discomfort [87–89]. Discomfort is related to the heat load a human experiences. Factors such as environmental temperature, relative humidity, wind speed, radiation, metabolic rate, and the thermal insulation and evaporative resistance of clothing all contribute to heat load [90,91]. Heat stress is defined as the net heat load to which a person is able to be exposed. Mild to high heat stress is manifested as the feeling of discomfort and can inhibit human functionality [91–93]. Heat stroke occurs when the heat load exceeds an individual's net load threshold [91,94,95].

Since temperature measurements alone cannot account for the effect of the environment on a body's comfort, particularly radiant and convective heat losses, many integrative methods have been developed in an attempt to quantify human thermal comfort [96]. One of these methods includes the use of a thermal manikin, which was first developed in the 1940's by the Army of the United States [96–99]. In the 1960's and

1970's new sweating thermal manikins with a cotton skin were able to generate a Permeability Index, I_m, and a pumping coefficient, (p), to predict thermophysiological responses of the wearer in certain garments [96,99]. It is important to understand that human perspiration occurs in both liquid and gaseous forms, but it is a significant challenge for a thermal manikin to mimic both of these forms of sweat. "Walter™", a male, hanging-type structure, sweating thermal manikin, developed by Fan and Chen at Hong Kong Polytechnic University in 2002, is able to simulate the gaseous form of sweat. Walter™'s trunk is constructed of fiber glass, and his skin is composed of a PA tabby fabric on the face side, a protective knitting fabric on the inner side, and a microporous polytetrafluoroethylene (PTFE) GORE-TEX® membrane acts as the middle layer. Deionized water substitutes as 'sweat' and is pumped to the body through a water pipe connected to the head of the manikin. Inside the trunk are three heaters to help the manikin achieve the desired temperature of testing, and a dual pipe system circulates water to the trunk and limbs. An additional challenge in simulating human sweat is that certain areas of the body, such as the underarms, perspire more than others. While Walter™ cannot mimic this type of variance in regional perspiration, his unique semi-permeable skin is able to secrete 'sweat' uniformly. The nine silicon rubber PT_{100} thin film patch sensors as seen in Figure 34, which conform to BS 1904 and DIN43760, take accurate measurements of skin temperature; and the change of water level due to 'perspiration' through the fabric surface is recorded in a constant time interval [97]. The water loss of the manikin due to 'perspiration' is measured by a top-loading balance with a tank of ~ 2.5 kg of water placed on it. This water, which allows for approximately three to five hours of 'sweating', is

pumped to the manikin via siphon action through soft tubing and is controlled with a system of valves [100].

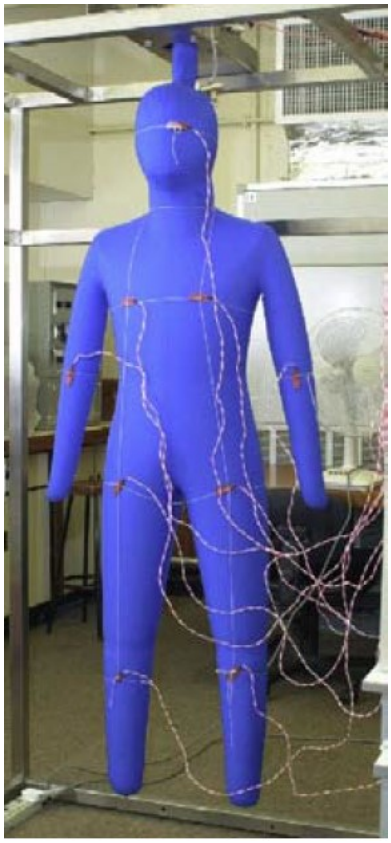

Figure 34: The thermal manikin "Walter™" [97,100]

Walter™ currently resides in the textile testing laboratory at Cornell University in the Department of Fiber Science & Apparel Design, where thermal comfort testing is carried out under standard atmosphere conditions (21° ± 2°C, 65% ± 5% RH) [101]. The two measurements generated by Walter™ that are most relevant to this work are thermal insulation (R_t) and moisture vapor resistance (R_{et}). The greater the thermal insulation of a garment, the greater the warmth of the wearer. The lower the moisture vapor resistance of a garment is, the greater its "breathability" as it allows sweat to evaporate from the skin through the fabric [102]. Measured factors that impact thermal insulation can be found in

Equation 3 where A is the total surface area of the manikin (A_s = 1.66 m^2), T_s is the mean skin temperature, T_a is the mean temperature of the environment, H_s is the heat supplied to the manikin, H_p is the heat generated by the pump (assuming that all energy supplied to pump is converted to heat), H_p is the power supply to the pump (H_p = 23.5 W), and H_e is the evaporative heat loss from the water evaporation. The equation for H_e (Equation 4) accounts for the heat of evaporation of water at the skin temperature (Λ) and the perspiration rate (i.e. water loss per unit time) (Q).

$$R_t = \frac{A_s(\overline{T}_s - T_a)}{H_s + H_p - H_e} \quad [3]$$

$$H_e = \lambda Q \quad [4]$$

Measured factors that impact moisture vapor resistance can be found in Equation 5 where P^*_s is the saturated water vapor pressure at the skin temperature, (i.e. the water vapor pressure of the water film just inside the 'skin'), RH_a is the relative humidity of the surrounding environment, P^*_a is the saturated water vapor pressure of the surrounding environment, and R_{es} (given in Equation 6 is the moisture vapor resistance of the 'skin'.

$$R_{et} = \frac{A_s(P_s^* - RH_a P_a^*)}{H_e} - R_{es} \quad [5]$$

$$R_{es} = \frac{A_s(P_s^* - RH_a P_a^*)}{H_e}. \quad [6]$$

These equations account for the resistance of clothing and the surface air layer. It is important to note that Walter™'s body core temperature is controlled at 37° ± 0.5°C [97].

The need for optimized personal protective clothing ensembles for the U.S. military has largely driven the advancement of thermal comfort measurement systems. In the last fifty years, the progressive development of sweating thermal manikins like Walter™ has significantly improved the simulation and quantification of comfort and are particularly useful in evaluating the thermal properties of clothing design and protective equipment quickly with accurate and repeatable results [96,97,99].

3.1.4. Coverall Design Selection

As part of the HATCH Project NC-170, Ashdown and Coffman conducted studies on optimal agricultural coverall design. Three coverall styles as shown in Figure 35 were tested: a Kleenguard® conventional coverall manufactured by Kimberly Clark (a), a recently developed ProShield® coverall manufactured by DuPont referred to here-in as Pro Style "P" (b), and a recently developed Kleenguard® coverall with elastic panels extending across the back all the way to the wrists underneath the arms (c). Previous to testing, noted disadvantages of the conventional Kleenguard® coverall design included limited ease of movement, a limited size range, and a bulky silhouette. The goal in developing the Pro Style "P" coverall was to increase ease of movement, increase the size range, and slim the silhouette. Previous field test subjects had observed that bulkier silhouettes led to more fabric tears. The design incorporated finely pleated gussets, shown in Figure 36, in the underarm, rear, and knee regions of the garment in order to enable greater mobility with a

slimmer silhouette. The Pro Style "P" design was selected for fabricating POM- and POM-N-halamine functionalized coveralls.

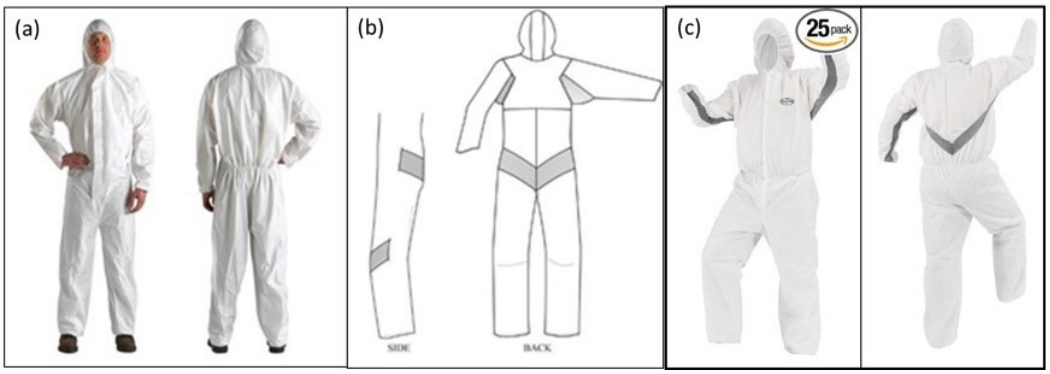

Figure 35: Three coverall styles tested in HATCH Project NC-170 (a) Kleenguard® conventional coverall, (b) ProShield® coverall, i.e. Pro Style "P", (c) Kleenguard® coverall with elastic panels extending across the back all the way to the wrists underneath the arms

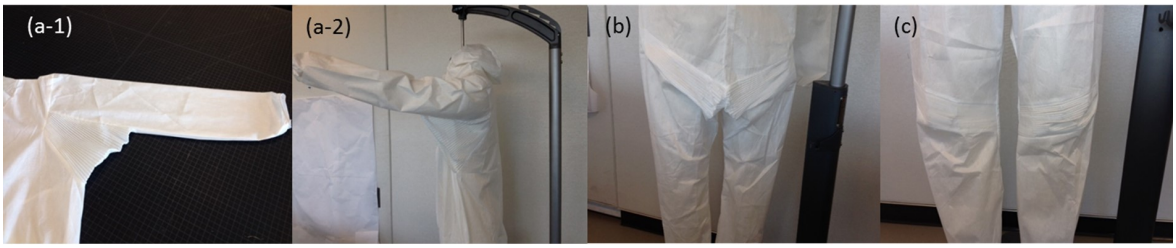

Figure 36: Gussets in (a-1) underarms, (a-2) underarms, (b) rear, (c) knees of the ProShield® coverall, i.e. Pro Style "P" coverall

3.2. Hypotheses

One method of polyoxometalate functionalization can be scaled to yield the same amount of weight percent POM loading on fabric as was observed in small scale sample testing. By fabricating coveralls with POMs immobilized on the surface of the fibrous substrates, a more accurate assessment of the effect of POM functionalization on human

thermal comfort factors will be achieved. Molecular polyoxometalate functionalization on fibrous substrates will not impact thermal comfort properties.

3.3. Experimental

3.3.1. Materials

Two 55/45 cotton / polyester plain weave sheets were prepared by Dr. Gang Sun of the University of California, Davis. One of the sheets was treated with N-halamines, and the other sheet was untreated. Two king-size white 100% premium combed long staple fiber flat-sheets were obtained from Utopia Bedding (South Australia). The properties of the fabrics are found in Table 4. Clorox® bleach was used for N-halamine activation.

Table 4 Properties of fibrous substrates

Samples	g/m²	Mean Thickness (mm)
100% cotton plain weave	130.52	0.23 ± 0.01
45/55 polycotton control plain weave	128.89	0.23 ± 0.01
45/55 polycotton N-halamine treated plain weave	142.22	0.23 ± 0.00

$H_5PV_2Mo_{10}O_{40}$ was synthesized using sodium molybdate dehydrate from EMD Chemicals, Inc. (EM-SX0650-2) (Phillipsburg, NJ), sodium metavanadate from Sigma-Aldrich (72060) (St. Louis, MO), sodium phosphate dibasic from Sigma-Aldrich (S0876) (St. Louis, MO), 0.5 N sulfuric acid (38295) from Sigma-Aldrich Fluka Analytical (St. Louis, MO), and methanol HPLC grade (34860) from Sigma-Aldrich (St. Louis, MO).

In order to functionalize the membranes with the polyoxometalates, 3-aminopropyltriethoxysilane (APTS) (440140) and ethanol (24102) were obtained from Sigma-Aldrich (St. Louis, MO). Toluene (FW-92.14, Lot: B46B20) and hexane (5189-16)

were obtained from Mallinckrodt Chemicals (Phillipsburg, NJ), and 85-87% phosphoric acid (0260) was obtained from J.T. Baker (Center Valley, PA).

3.3.2 Methodology

3.3.2.1. Preparation of the Coverall Pattern Pieces

First the N-halamine treated polycotton sheet was washed in a bath of 5% w/v Clorox / deionized water in order to 'activate' the N-halamines. All fabrics were ironed on a heat setting for cotton with steam. Two yards of each fabric was sent to Stanley Pleating & Stitching (Long Island City, NY) where pleats with a spacing of ¼ inch and a pleat depth of ¼ inch were set in each of the fabrics.

By dressing Walter™, the thermal manikin, in the varying sizes of the Pro Style "P" coverall and assessing best fit, it was determined that the size small pattern should be used for constructing the test coveralls. According to the Pro Style "P" coverall pattern specifications, pieces of fabric were cut in order to construct a 100% cotton control coverall, a 100% cotton POM-functionalized coverall, a 55/45 cotton / polyester control coverall, and a 55/45 cotton / polyester POM-functionalized coverall. Pattern pieces for the underarm, rear, and knee gussets were carefully cut from the corresponding pleated fabrics. All pattern pieces were serged on the edges with 65/35 polycotton thread to prevent fraying during the POM functionalization process.

3.3.2.2. Scaled Polyoxometalate Functionalization

The method used in Chapter 2 to immobilize the POMs on the fibrous substrates via electrostatic attraction (M2) was chosen for the POM-functionalized coverall experiments in Chapter 3 due to its ease of scalability and its relative popularity in the literature. The serged coverall pattern pieces were added piecewise to the gallon bath

consisting of 5% 3-aminopropyltriethoxysilane (APTS) in a mixture of 80/20 v/v deionized water with ethanol, lowered to pH 2 with phosphoric acid according to a liquor ratio of 36:1. The fabrics were left to react for 60 min. Predissolved POM was added yielding a 1% POM w/v bath. The gallon jars were shaken for 5 min and then left to react for 18 h at RT using rapid mechanical stirring to ensure bath uniformity. After 18 h, the specimens were removed and rinsed with mechanical stirring in 3 subsequent 50/50 v/v toluene/ethanol gallon baths for one hour each, a hexane bath for one hour, three water baths for one hour each, and an ethanol bath for one hour in order to ensure the complete removal of any unreacted silane and unreacted POM particles. The specimens were then air dried for 48 h. After drying, the pattern pieces were characterized using FTIR.

3.3.2.3. Coverall Fabrication

After FTIR characterization, the pattern pieces of each fabric type were sewn into their respective coveralls using 65/35 polycotton thread. A 24" nylon coil polyester tape zipper was sewn in the front of the coverall, and ¼ inch thick elastics were sewn at the ends of the sleeves and legs. Figure 37 shows the 100% cotton POM-treated coverall. Not visible in Figure 37 is the hood of the coverall.

Figure 37: Fabricated 100% cotton POM-treated coverall.

3.3.2.4. Coverall Characterization

3.3.2.4.1. Thermal Manikin Assessment of Coverall Thermal Comfort

Once the four coveralls were sewn, each was conditioned at 21° ± 2°C, 65% ± 5% RH for 48 h prior to being weighed and tested on the thermal manikin. The method of testing was derived from the ASTM F2370 standard [103]. For each thermal manikin test, Walter™ was carefully dressed in the coverall ensuring that all temperature sensors on the body remained in their designated testing positions. The water tank was filled, and the

temperature control and measurement systems for the manikin were monitored for 2 h to allow for the stabilization of moisture accumulation in the coverall. Measurements of the temperatures and heat supply were taken if the core temperature varied within ± 0.5ºC, and data was recorded every 40 s. (The display calculated the average of 50 measurements.) The system was checked every 1 h to ensure the stabilization of the perspiration rate. Sweating was simulated by capillary fluid transmission through the pores of the coverall fabric. The measurement period for each coverall post-stabilization was 6 h. After testing, the coverall was removed from the manikin and weighed on a top-loading balance to the nearest 0.01 g. Thermal insulation and evaporative resistance values were averaged, and the change in weight of the ensemble was determined.

3.3.2.4.2. Moisture Vapor Permeability

Moisture vapor permeability is defined as the measure of the passage of water vapor through the material (a.k.a. water vapor transmission rate, a.k.a. water vapor permeability). Following the analysis of thermal manikin testing, three circles 90 mm in diameter were cut from three different areas of each coverall and conditioned for an additional 24 h prior to the water vapor permeability test according to Appendix B (Determination of Water Vapour Permeability Index) of the BS 7209: 1990 – the British Standard Specification for Water Vapour Permeable Apparel Fabrics – test method. For each specimen, a metal cup was filled to a level that allowed for a 10 mm air gap between the fabric and the water in the cup. The internal diameter of the test dish was measured to be 80 mm. A triangular fabric support was placed in the notches on the cup rim. Adhesive glue was applied to the rim of the cup, and the specimen was placed on the support ensuring that the edges were aligned with the rim. Once the glue was dry, impermeable

tape was applied around the cup's rim to ensure no water or air could escape from other areas of the cup except through the exposed area of fabric. All sample cup + fabric assemblies were prepared in this manner. The cups were placed on a rotating turntable for at least 1 h to allow each sample to reach equilibrium. Once equilibrium was achieved, each cup + fabric assembly was weighed on a top-loading balance to the nearest 0.001 g. After weighing, the cups were re-placed on the rotating turntable. The time of the measurement and the weight was noted. Measurements were taken at varied time intervals over a 40 h period. The loss in mass (M) of the assembly over time (t) was calculated as well as the area (A) in m^2 of the exposed test fabric defined in Equation 7 where d is the internal diameter of the test dish. The water vapor permeability (WVP) in $g/m^2/day$ was then calculated using Equation 8. Lastly, the water vapor permeability index (*I*) was calculated using Equation 9, where $(WVP)_f$ is the mean water vapor permeability of the fabric under test and $(WVP)_r$ is the water vapor permeability of the reference fabric. In these tests the reference fabric referred to the respective non-POM treated control sample. Also, *I* was calculated using the 100% cotton plain weave sheeting fabric as the reference fabric for all test specimens.

$$\mathbf{A} = \left(\frac{\pi \mathbf{d}^2}{4}\right) \mathbf{x}\, \mathbf{10^{-6}} \qquad [7]$$

$$\mathbf{WVP} = \frac{\mathbf{24\ M}}{\mathbf{A\ t}} \qquad [8]$$

$$I = \left(\frac{WVP_f}{WVP_r}\right) x\ 100 \qquad [9]$$

3.3.2.4.3. Tensile Strength

The breaking force of the coverall fabrics was measured according to ASTM D5034 Breaking Force and Elongation of Textile Fabrics (Grab Test) using and Instron fitted with rubber faced jaws (25 x 37.5 mm), a gage length of 75±1 mm, and a crosshead speed of 300 ± 10 mm/min (so that the break occurred in 20±3 seconds). Fabric samples were cut lengthwise (100 mm x 150 mm) in the warp direction from each coverall. Tests were run in triplicate, and each sample was cut from a different area of the respective coverall. The mean breaking force (N) was noted, and the mean percent elongation was calculated from the mean extension at break (mm) and gauge length (mm).

3.3.2.4.4. Additional Characterization

Characterization via SEM and TGA weight analysis occurred after the coveralls underwent all thermal manikin testing.

3.3.2.5. Statistical Analysis

Results from thermal comfort and mechanical strength testing were assessed using JMP 10 (SAS, Cary, NC) via one-way analyses of variance (ANOVA). Statistical testing determined if significant differences were evident between the values for thermal insulation of POM-treated coveralls and their respective non-treated control coverall. In the same manner, this examination of statistically significant differences in evaporative resistance, moisture vapor permeability, and tensile strength was performed and respective p-values were calculated. P-values less than 0.05 denoted statistical significance.

3.4. Results & Discussion

3.4.1. Thermal Manikin Assessment of Coverall Thermal Comfort

The mean thermal insulation *(m^2°C/W)* and evaporative resistance (*(Pa m^2/W)* values of each coverall are listed in Tables 5 & 7 and are graphed in Figures 38 & 39. No statistically significant difference ($p > 0.05$) was determined between the 100% cotton control coverall and the POM-treated 100% cotton coverall as seen in Table 6. Likewise, no statistically significant difference ($p > 0.05$) was evident between the polycotton control coverall and the POM-N-halamine treated polycotton coverall as seen in Table 8. These results suggest that POM-functionalization at these respective loadings has no observable effect on thermal insulation of the coverall. However, POM-treated cotton did have a statistically higher ($p < 0.05$) evaporative resistance than its control counterpart. While the difference appears minimal, it suggests that POM-functionalized cotton at this loading would have slightly inhibited breathability. More coveralls would need to be fabricated and tested to determine if this observation could be substantiated. Unlike the cotton samples, the POM-N-halamine treated polycotton showed no evidence of increasing the evaporative resistance of the coverall. Wide variation was seen in the measured values of evaporative resistance for the polycotton control perhaps caused by temperature or humidity fluctuations in the standard conditioning room. More samples must be tested in the future to determine the validity of these results.

Table 5: The Thermal Insulation of the Four Coveralls

Coverall Sample	Thermal Insulation (m^2°C/W)		
	Mean	Stdev	CV %
100% Cotton - no POM (Control)	0.28	0.002	1.2
100% Cotton + POM	0.19	0.002	1.1
Polycotton - no POM (Control)	0.18	0.009	4.9
Polycotton + N-Halamine + POM	0.19	0.002	1.3

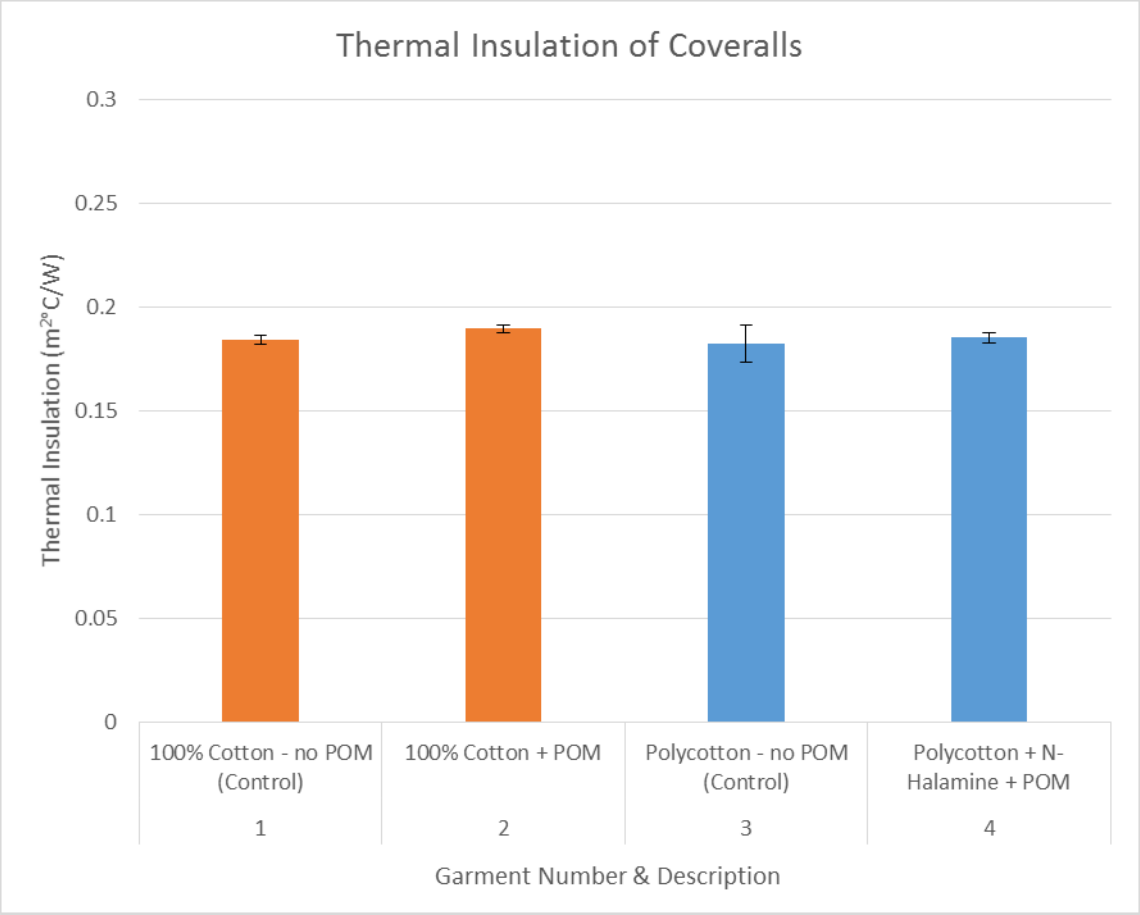

Figure 38: The Thermal Insulation of the Four Coveralls

Table 6: Statistical Analysis of Thermal Insulation of the Four Coveralls

ANOVA

Source of Variation	*SS*	*df*	*MS*	*F*	*P-value*	*F crit*
Between Groups	0.000143	3	0.00005	2.116895	0.135868	3.196777
Within Groups	0.000382	17	0.00002			
Total	0.000525	20				

Table 7: The Evaporative Resistance of the Four Coveralls

Coverall Sample	Evaporative Resistance (Pa m^2/W)		
	Mean	Stdev	CV %
100% Cotton - no POM (Control)	27.7	0.1	0.4
100% Cotton + POM	30.8	0.3	0.9
Polycotton - no POM (Control)	30.7	1.9	6.1
Polycotton + N-Halamine + POM	29.1	0.4	1.3

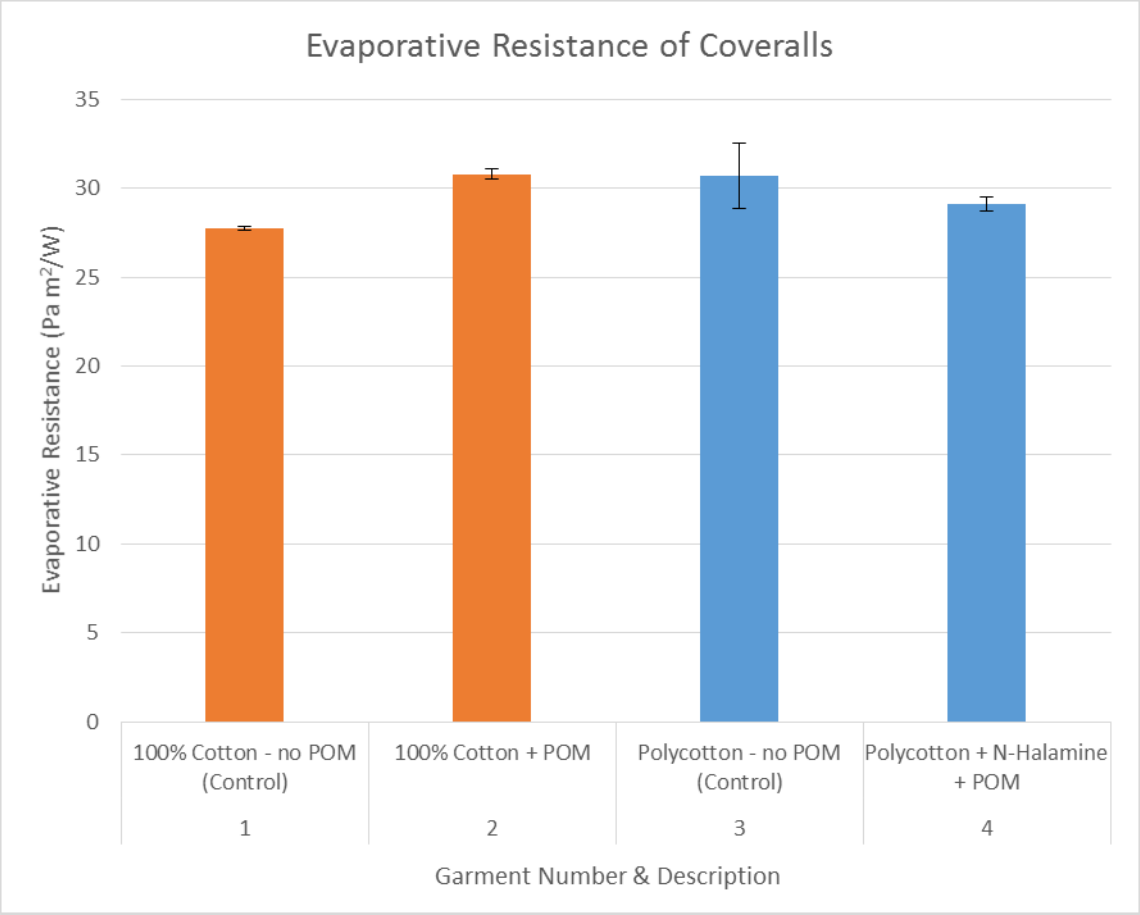

Figure 39: The Evaporative Resistance of the Four Coveralls

Table 8: Statistical Analysis of Evaporative Resistance of the Four Coveralls

ANOVA

Source of Variation	*SS*	*df*	*MS*	*F*	*P-value*	*F crit*
Between Groups	34.77733	3	11.59244	13.16191	0.000108	3.196777
Within Groups	14.97287	17	0.880757			
Total	49.7502	20				

3.4.2. Moisture Vapor Permeability

A higher moisture or water vapor permeability of a substrate indicates higher breathability. The water vapor permeability of the polycotton control was 733 ± 18 g/m^2/day, which was lower than the moisture vapor permeability of the POM-N-halamine treated polycotton (WVP = 750 ± 5 g/m^2/day) although these results were not statistically different from each other ($p = 0.14$). Likewise, the cotton control (WVP = 730 ± 16 g/m^2/day) was not statistically different from its POM-treated counterpart (WVP = 727 ± 19) ($p = 0.27$). These results shown in Figure 40 suggest that moisture vapor permeability is not hindered by POM functionalization via this method (M2) at these loadings on the substrate. The moisture vapor permeability will be analyzed further in future work.

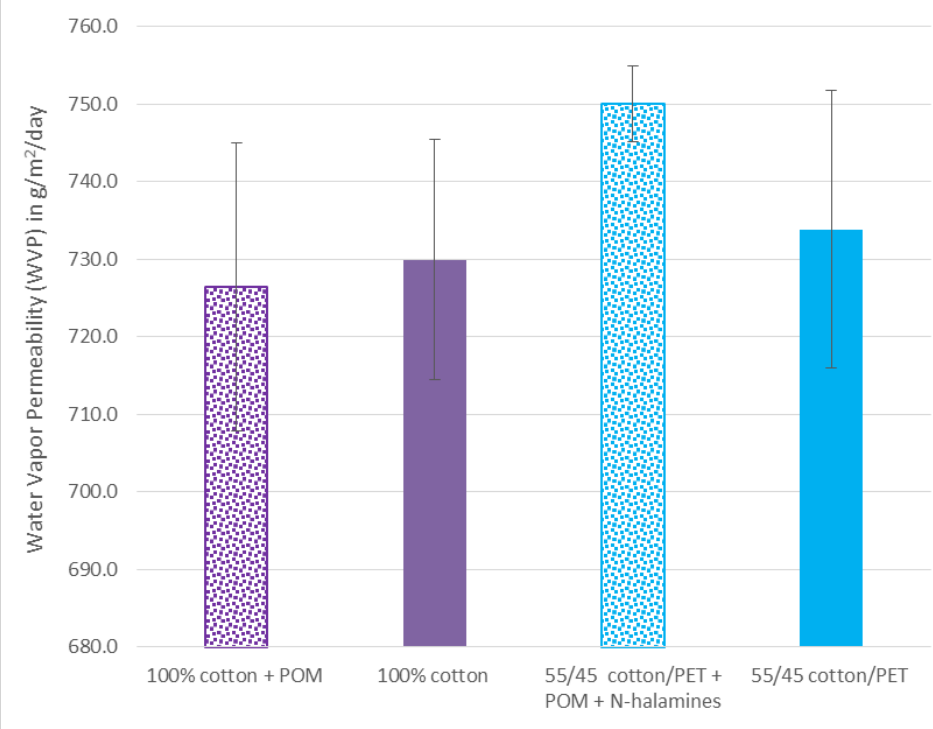

Figure 40: Mean Water Vapor Permeability of POM-treated Coverall fabrics relative to control fabrics

3.4.3. Mechanical Properties

The tensile strength of the POM-treated cotton coverall fabric as shown in Figure 41, was more than twice that of its cotton control counterpart. While this was not expected, a possible explanation may be that the POM functionalization process caused changes to the microstructure, morphology, or conformation of the cellulose chains yielding a stronger fiber. Another possible explanation may be that the POM functionalization on cotton forms linkages in the interstices of the fabric giving it higher strength. Interestingly, the Tencel® fabrics used in Chapter 2 of this work exhibited a similar trend where the tensile strength of the POM-treated Tencel® was twice that of its non-POM treated counterpart. However, this trend was not seen for the polycotton fabrics,

where the POM-treated polycotton had a significantly lower tensile strength compared to its control counterpart.

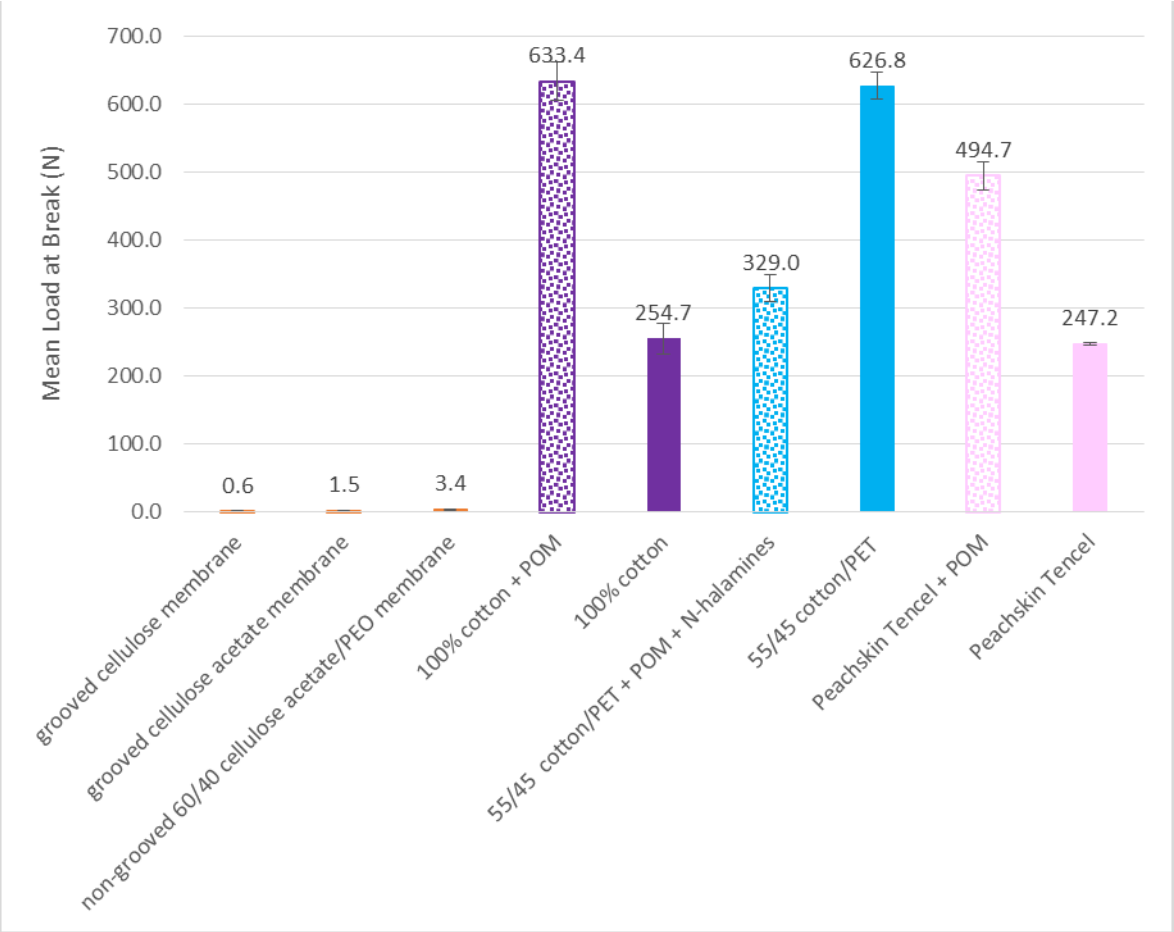

Figure 41: Instron Tensile Strength of Ch. 2 & Ch. 3 Fibrous Substrates

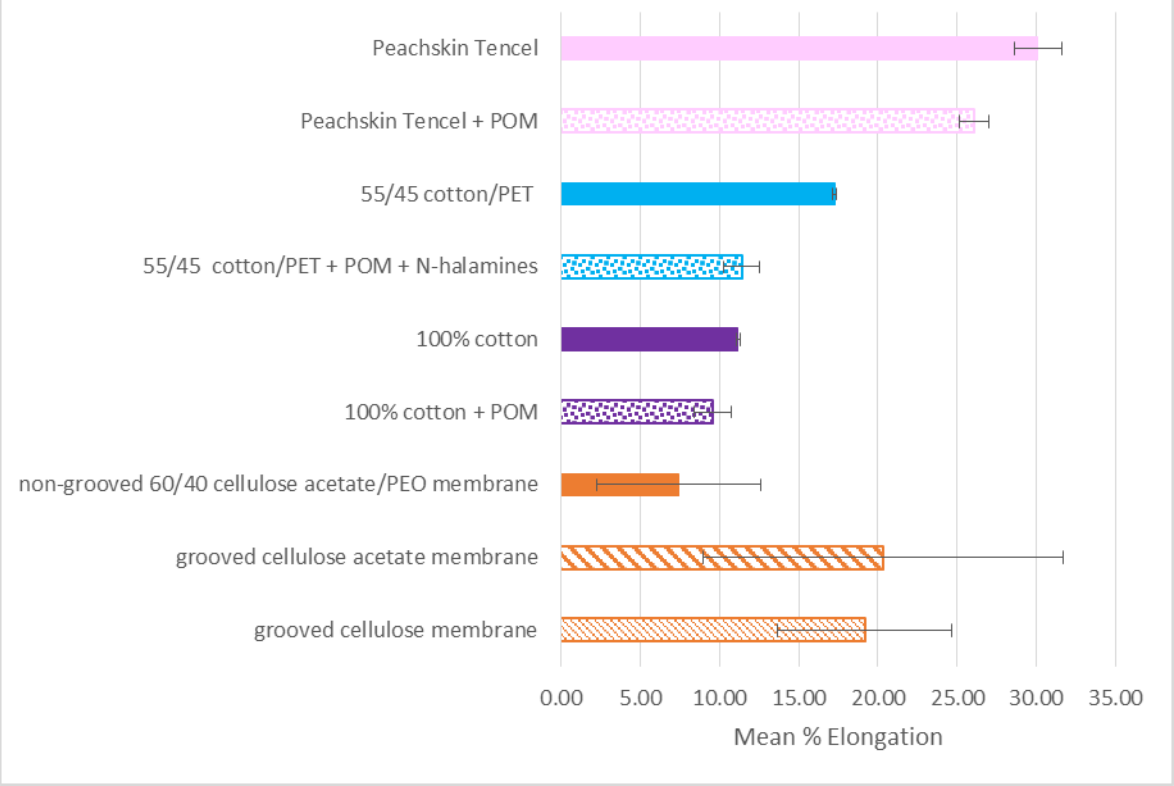

Figure 42: Instron Mean Percent Elongation of Ch. 2 & Ch. 3 Fibrous Substrates

The Tencel® fabrics, both POM-treated and non-POM treated from Chapter 2 exhibited a statistically significant higher percent elongation than the cotton or polycotton substrates. Significantly, the percent elongation decreased when a substrate was functionalized with POMs. This increase in tensile strength and decrease in percent elongation due to POM functionalization can be correlated to the substrates' increases in roughness of hand post-functionalization.

3.4.4. Additional Characterization

TGA weight analysis determined that the POM-treated 100% cotton coveralls achieved a 9.1 ± 1.7 wt.% POM add-on, and the POM-N-halamine treated polycotton achieved a 1.0 ± 0.3 wt.% POM add-on. These values corresponded closely to the

measured wt.% POM add-on of the respective smaller scale POM-treated samples of 100% cotton and N-halamine-treated polycotton functionalized with the same method. Analysis of SEM images of POM-treated substrates (Figure 43) showed no evident difference between the smaller scale samples and the scaled samples of cotton and polycotton. These results convey that the method is repeatable and scalable.

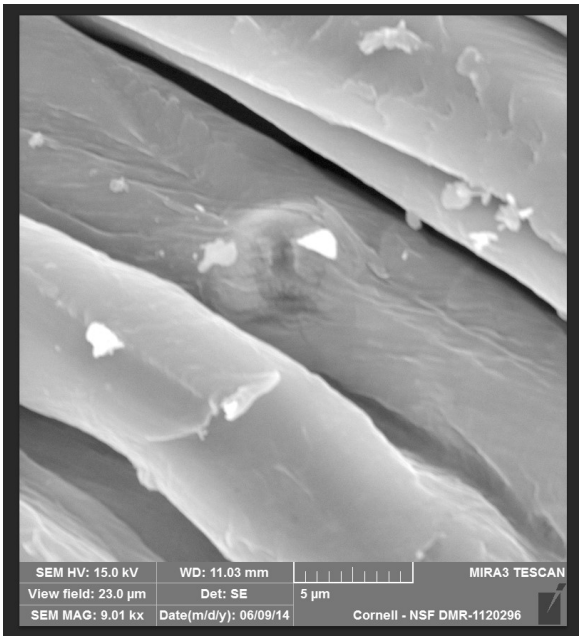

Figure 43: SEM of POM-treated 100% cotton coverall

CHAPTER 4

RESEARCH CONCLUSIONS AND IMPLICATIONS FOR FUTURE WORK

4.1 Overall Conclusions

The POM $H_5PV_2Mo_{10}O_{40}$ was synthesized as a non-crystalline precipitate and used to functionalize fibers to obtain self-decontamination. The electrospinning of a 60/40 CA: PEO co-continuous fibrous membrane created a non-grooved fiber morphology. By extracting the PEO from the membranes, a grooved fiber morphology was created to significantly increase the fiber surface area, which in turn provided greater fiber surface area for POM binding. Consequently, POM grafted grooved nanofibrous membranes exhibited approximately 25% more methyl parathion degradation in comparison with that of POM grafted non-grooved nanofibrous membranes. This study also showed that the POM functionalized grooved nanofibrous membranes outperformed conventional cotton and commercial Tencel® peach skin fabric grafted with POM. No significant statistical differences in decontamination performance were found between the two methods of functionalization. POM-grafting (M1) may employ a similar POM-substrate functionalization mechanism as POM-immobilization (M2).

The novel POM grafted grooved nanofibrous membranes have potential to be used in chemical protective apparel applications in defense or agriculture for enhanced self-decontamination of organophosphates and breathable porous structure. Further work is needed to examine thermal comfort and mechanical properties of such materials before they can be optimally incorporated in end-use products.

Electrostatically binding polyoxometalates (POM-immobilization – M2) to the surface of cellulosic substrates or cellulosic blend substrates such as the 55/45 cotton

polyester is a viable methodology for scalability and results in no significant difference between the POM weight percent add-on of small scale samples versus larger scale samples. The fabrication of POM-treated coveralls enabled a more accurate assessment of human comfort factors, such as thermal insulation, evaporative resistance, and moisture vapor permeability, than small scale sample testing. Functionalizing cotton and polycotton coveralls with their respective measured POM loadings does not significantly impact thermal insulation. More coverall tests need to be performed in future experiments to determine the relationship between evaporative resistance and POM functionalization, but this work suggests that the impact of the POM functionalization on this thermal comfort property may be minimal at these POM loadings. POM functionalization had no significant effect on the measured moisture vapor permeability of the fabrics suggesting that POM functionalization may not impact this quantification of fabric breathability. Fibrous substrates functionalized with POMs via electrostatic binding experience a significant decrease in the percent elongation, while tensile strength of the substrate can vary widely. Overall, this work illustrates that a self-decontaminating coverall can be fabricated without significantly compromising the wearer's breathability and comfort, however some mechanical properties may be diminished.

4.2 Suggestions for Future Work

One crucial piece of work needed is to determine how benign polyoxometalates are for humans with long-term exposure. A method for incorporating the high surface area POM-functionalized grooved nanofibrous membranes into a multilayered protective ensemble that prevents the penetration of threat substances, while enabling the transport of moisture vapor from the skin through the fabric, needs to be developed. Further examination of the

exact mechanism of POM functionalization to a fibrous substrate is needed by determining if a covalent linkage between the POM and substrate can be formed. A decontamination methodology needs to be developed in the gaseous phase in order to assess the ability of polyoxometalates to degrade aerosolized organophosphates, which is a common delivery system for chemical warfare agents in the field. Further examination of the degradation mechanism(s) and degradation products of this POM when in contact with methyl parathion would offer more in-depth insight into whether this technology is viable for commercial use. It would also be helpful to test how many catalytic cycles this POM can undergo when functionalized to a fibrous surface in order to assess its degree of re-usability in protective apparel and other filtration applications. More studies on the effect of POM functionalization on evaporative resistance and moisture vapor permeability as well as determining an optimal amount of POM weight percent add-on for maximized decontamination and maximized breathability would greatly benefit researchers, workers, and consumers seeking to find the balance between protection and comfort.

4.3 References

[1] S.L. Bartelt-Hunt, D.R.U. Knappe, M.A. Barlaz, A Review of chemical warfare agent simulants for the study of environmental behavior, Crit. Rev. Environ. Sci. Technol. 38 (2008) 112–136.

[2] M.T. Pope, Heteropoly and isopoly oxometalates, (1983).

[3] M. Misono, Heterogeneous catalysis by heteropoly compounds of molybdenum and tungsten, Catal. Rev. 29 (1987) 269–321.

[4] C.L. Hill, C.M. Prosser-McCartha, Homogeneous catalysis by transition metal oxygen anion clusters, Coord. Chem. Rev. 143 (1995) 407.

[5] A.M. Khenkin, L. Weiner, Y. Wang, R. Neumann, Electron and oxygen transfer in polyoxometalate, $H_5PV_2Mo_{10}O_{40}$, catalyzed oxidation of aromatic and alkyl aromatic compounds: evidence for aerobic Mars-van Krevelen-type reactions in the liquid homogeneous phase., J. Am. Chem. Soc. 123 (2001) 8531–42.

[6] E.A. Boring, C. Hill, J.T. Rhule, L. Xu, Polyoxometalate materials, metal-containing materials, and methods of use thereof, WO2001034279 A3, 2002.

[7] J.F. Keggin, Structure of the crystals of 12-phosphotungstic acid, Nature. 132 (1933) 351–351.

[8] R.P. Johnson, C.L. Hill, Polyoxometalate oxidation of chemical warfare agent simulants in fluorinated media, JAT J. Appl. Toxicol. 19 (1999) S71–S75.

[9] J. Arichi, M.M. Pereira, P.M. Esteves, B. Louis, Synthesis of Keggin-type polyoxometalate crystals, Solid State Sci. 12 (2010) 1866–1869.

[10] I.V. Kozhevnikov, K.I. Matveev, Homogeneous catalysts based on heteropoly acids (review), Appl. Catal. Appl. Catal. 5 (1983) 135–150.

[11] R. Neumann, I. Assael, Oxybromination catalysed by the heteropolyanion compound $H_5PMo_{10}V_2O_{40}$ in an organic medium: selective para-bromination of phenol, J. Chem. Soc. Chem. Commun. (1988) 1285–1287.

[12] C. Hill, D. Duncan, M. Harrup, Multifunctional Polyoxometalates as catalysts for environmentally benign processes, Comments Inorg. Chem. 14 (1993) 367–384.

[13] R.D. Gall, M. Faraj, C.L. Hill, Role of water in polyoxometalate-catalyzed oxidations in nonaqueous media. Scope, kinetics, and mechanism of oxidation of thioether mustard (HD) analogs by tert-butyl hydroperoxide catalyzed by $H_5PV_2Mo_{10}O_{40}$, Inorg. Chem. 33 (1994) 5015.

[14] I.V. Kozhevnikov, Catalysis by Heteropoly Acids and Multicomponent Polyoxometalates in Liquid-Phase Reactions, Chem. Rev. 98 (1998) 171–198.

[15] R.R. Ozer, J.L. Ferry, Kinetic probes of the mechanism of polyoxometalate-mediated photocatalytic oxidation of chlorinated organics, J. Phys. Chem. B. 104 (2000) 9444–9448.

[16] B.W. Michel, L.D. Steffens, M.S. Sigman, The wacker oxidation, in: Org. React., John Wiley & Sons, Inc., Hoboken, NJ, USA, 2014: pp. 75–414.

[17] C.L. Hill, R.B. Brown, Sustained epoxidation of olefins by oxygen donors catalyzed by transition metal-substituted polyoxometalates, oxidatively resistant inorganic analogs of metalloporphyrins, J. Am. Chem. Soc. 108 (1986) 536–538.

[18] J.R. Morrow, W.C. Trogler, Hydrolysis of phosphate triesters with copper(II) catalysts, Inorg. Chem. - Inorg. Chem. 28 (1989).

[19] M. Sharmila, K. Ramanand, N. Sethunathan, Hydrolysis of methyl parathion in a flooded soil, Bull Env. Contam Toxicol Bull. Environ. Contam. Toxicol. 43 (1989) 45–51.
[20] J. Tian, J. Wang, S. Zhao, C. Jiang, X. Zhang, X. Wang, Hydrolysis of cellulose by the heteropoly acid $H_3PW_{12}O_{40}$, Cellulose. 17 (2010) 587–594.
[21] D.C. Fee, D.R. Gard, C.-H. Yang, Phosphorus compounds, in: Kirk-Othmer Encycl. Chem. Technol., John Wiley & Sons, Inc., 2000.
[22] R.L. Metcalf, Insect control, in: Ullmanns Encycl. Ind. Chem., Wiley-VCH Verlag GmbH & Co. KGaA, 2000.
[23] J. Senthilnathan, L. Philip, Removal of mixed pesticides from drinking water system using surfactant-assisted nano-TiO2, Water. Air. Soil Pollut. 210 (2010) 1–4.
[24] M. Lissel, H. Jansen in de Wal, R. Neumann, Oxidation of activated phenols by dioxygen catalysed by the $H_5PV_2Mo_{10}O_{40}$ heteropolyanion, (1992).
[25] L. Xu, E. Boring, C.L. Hill, Polyoxometalate-modified fabrics: new catalytic materials for low-temperature aerobic oxidation, J. Catal. 195 (2000) 394–405.
[26] C.L. Hill, Metal−oxygen clusters. The surface and catalytic properties of heteropoly oxometalates. From the Series: Fundamental and Applied Catalysis. Kluwer Academic/Plenum Publishers: NY, J. Am. Chem. Soc. 124 (2002) 10935–10936.
[27] J. Walker, H. Schreuder-Gibson, W. Yeomans, D. Ball, F. Hoskin, C. Hill, Development of self-detoxifying materials for chemical protective clothing, Army Natick Soldier Center MA, 2003.
[28] U. Drechsler, W. Singh, A. Sharma, Functionalization of polymers with reactive species having bond-stabilized decontamination activity, (2009). https://www.google.com/patents/US20090012204.
[29] D.M. Mizrahi, S. Saphier, I. Columbus, Efficient heterogeneous and environmentally friendly degradation of nerve agents on a tungsten-based POM, J. Hazard. Mater. 179 (2010) 1–3.
[30] J. Doshi, D.H. Reneker, Electrospinning process and applications of electrospun fibers, in: Conf. Rec. 1993 IEEE Ind. Appl. Soc. Annu. Meet. 1993, 1993: pp. 1698–1703 vol.3.
[31] V. Dixit, J. Tewari, S.K. Obendorf, Fungal growth inhibition of regenerated cellulose nanofibrous membranes containing Quillaja Saponin, Arch. Environ. Contam. Toxicol. 59 (2010) 417–423.
[32] D.J. Woo, S.K. Obendorf, MgO-embedded fibre-based substrate as an effective sorbent for toxic organophosphates, RSC Adv. 4 (2014) 15727–15735.
[33] J.T. McCann, D. Li, Y. Xia, Electrospinning of nanofibers with core-sheath, hollow, or porous structures, J. Mater. Chem. 15 (2005) 735.
[34] C. Tang, P. Chen, H. Liu, Cocontinuous cellulose acetate/polyurethane composite nanofiber fabricated through electrospinning, Polym. Eng. Sci. 48 (2008) 1296–1303.
[35] W. Zhang, D. Yao, Q. Zhang, J.G. Zhou, P.I. Lelkes, Fabrication of interconnected microporous biomaterials with high hydroxyapatite nanoparticle loading, Biofabrication. 2 (2010) 35006.
[36] L. Nguyen, F. Mighri, Y. Deyrail, S. Elkoun, Conductive materials for proton exchange membrane fuel cell bipolar plates made from PVDF, PET and co-

continuous PVDF/PET filled with carbon additives, FUCE Fuel Cells. 10 (2010) 938–948.
[37] M.E. Vallejos, M.S. Peresin, O.J. Rojas, All-Cellulose composite fibers obtained by electrospinning dispersions of cellulose acetate and cellulose nanocrystals, J. Polym. Environ. 20 (2012) 1075–1083.
[38] H. Liu, Y.-L. Hsieh, Ultrafine fibrous cellulose membranes from electrospinning of cellulose acetate, J. Polym. Sci. Part B Polym. Phys. 40 (2002) 2119–2129.
[39] G.A. Tsigdinos, C.J. Hallada, Molybdovanadophosphoric acids and their salts. I. Investigation of methods of preparation and characterization, Inorg. Chem. 7 (1968) 437–441.
[40] L. Pettersson, I. Andersson, J.H. Grate, A. Selling, Multicomponent polyanions. 46. Characterization of the isomeric Keggin decamolybdodivanadophosphate ions in aqueous solution by 31P and 51V NMR, Inorg. Chem. 33 (1994) 982–993.
[41] A. Selling, I. Andersson, L. Pettersson, C.M. Schramm, S.L. Downey, J.H. Grate, Multicomponent polyanions. 47. The aqueous vanadophosphate system, Inorg. Chem. 33 (1994) 3141–3150.
[42] U.G. Nielsen, A. Hazell, J. Skibsted, H.J. Jakobsen, C.J. McKenzie, Solid-state 51V MAS NMR spectroscopy determines component concentration and crystal phase in co-crystallised mixtures of vanadium complexes, CrystEngComm. 12 (2010) 2826–2834.
[43] K. Tan, S.K. Obendorf, Surface modification of microporous polyurethane membrane with poly(ethylene glycol) to develop a novel membrane, J. Membr. Sci. 274 (2006) 150–158.
[44] Y. Guo, C. Hu, C. Jiang, Y. Yang, S. Jiang, X. Li, E. Wang, Preparation and heterogeneous photocatalytic behaviors of the surface-modified porous silica materials impregnated with monosubstituted Keggin units, J. Catal. 217 (2003) 141–151.
[45] H. Kim, J.C. Jung, P. Kim, S.H. Yeom, K.-Y. Lee, I.K. Song, Preparation of $H_3PMo_{12}O_{40}$ catalyst immobilized on surface modified mesostructured cellular foam (SM-MCF) silica and its application to the ethanol conversion reaction, J. Mol. Catal. Chem. 259 (2006) 150–155.
[46] L. Chen, K. Zhu, L.-H. Bi, A. Suchopar, M. Reicke, G. Mathys, H. Jaensch, U. Kortz, R.M. Richards, Solvent-free aerobic oxidation of n-alkane by iron(III)-substituted polyoxotungstates immobilized on SBA-15, Inorg. Chem. 46 (2007) 8457–8459.
[47] M.G. Clerici, O.A. Kholdeeva, Liquid phase oxidation via heterogeneous catalysis: organic synthesis and industrial applications, Wiley, 2013.
[48] M.-C.B. Salon, G. Gerbaud, M. Abdelmouleh, C. Bruzzese, S. Boufi, M.N. Belgacem, Studies of interactions between silane coupling agents and cellulose fibers with liquid and solid-state NMR, Magn. Reson. Chem. 45 (2007) 473–483.
[49] H. Schreuder-Gibson, P. Gibson, K. Senecal, M. Sennett, J. Walker, W. Yeomans, D. Ziegler, P.P. Tsai, Protective textile materials based on electrospun nanofibers, J. Adv. Mater. 34 (2002) 44–55.
[50] R.D. Gall, C.L. Hill, J.E. Walker, Carbon powder and fiber-supported polyoxometalate catalytic materials. Preparation, characterization, and catalytic

oxidation of dialkyl sulfides as mustard (HD) analogues, Chem. Mater. 8 (1996) 2523–2527.
[51] L.E. Lange, S.K. Obendorf, Functionalization of cotton fiber by partial etherification and self-assembly of polyoxometalate encapsulated in $Cu_3(BTC)_2$ metal–organic framework, ACS Appl. Mater. Interfaces. 7 (2015) 3974–3980.
[52] J. Song, Z. Luo, D.K. Britt, H. Furukawa, O.M. Yaghi, K.I. Hardcastle, C.L. Hill, A multiunit catalyst with synergistic stability and reactivity: A polyoxometalate–metal organic framework for aerobic decontamination, J. Am. Chem. Soc. 133 (2011).
[53] R.A. Nyquist, R.O. Kagel, Infrared spectra of inorganic compounds, Academic Press, New York; London (24 Oval Rd, N.W.1), 1971.
[54] J.W. Robinson, Practical handbook of spectroscopy, CRC Press, Boca Raton, 1991.
[55] H.M. Selim, D.L. Sparks, Heavy metals release in soils, CRC Press, 2001.
[56] P. Larkin, Infrared and Raman spectroscopy; Principles and spectral interpretation, Elsevier, 2011.
[57] K. Nakamoto, Infrared and Raman spectra of inorganic and coordination compounds, in: Handb. Vib. Spectrosc., John Wiley & Sons, Ltd, 2006.
[58] M. Misono, T. Solid superacid catalysts, ChemTech U. S. 23:11 (1993).
[59] J.C. Harris, Detergency evaluation. III. Adjustment of Terg-O-Tometer and launderometer wash test methods to produce comparable soil removal data, J. Am. Oil Chem. Soc. 29 (1952) 110–113.
[60] L.L. Ko, S.K. Obendorf, Effect of starch on reducing the retention of methyl parathion by cotton and polyester fabrics in agricultural protective clothing, J. Environ. Sci. Health Part B. 32 (1997) 283–294.
[61] A. Popa, V. Sasca, M. Stefanescu, E. Kis, R. Marinkovic-Neducin, The influence of the nature and textural properties of different supports on the thermal behavior of Keggin type heteropolyacids, J. Serbian Chem. Soc. 71 (2006) 235–249.
[62] J. Arichi, M. Eternot, B. Louis, Synthesis of V-containing Keggin polyoxometalates: Versatile catalysts for the synthesis of fine chemicals, Catal. Today. 138 (2008) 117–122.
[63] L.M. Gratton, S. Paglia, F. Scattaglia, M. Cavallini, Infrared emission spectroscopy applied to the oxidation of molybdenum, Appl. Spectrosc. 32 (1978) 310–316.
[64] M.J. Almond, C.A. Yates, R.H. Orrin, D.A. Rice, Applications of Fourier transform Raman spectroscopy - a tool for inorganic, organometallic and solid state chemists, Spectrochim. Acta Part Mol. Spectrosc. 46 (1990) 177–186.
[65] R. Ramirez, B. Casal, L. Utrera, E. Ruiz-Hitzky, Oxygen reactivity in vanadium pentoxide: electronic structure and infrared spectroscopy studies, J. Phys. Chem. 94 (1990) 8960–8965.
[66] S.J. Hug, A. Johnson, G. Friedl, T. Lichtensteiger, H. Belevi, M. Sturm, Characterization of environmental solids and surfaces, Chim. Int. J. Chem. 51 (1997) 884–892.
[67] M.D. Zidan, A.W. Allaf, The gas-phase on-line production of vanadium oxytrihalides, VOX_3 and their identification by infrared spectroscopy, Spectrochim. Acta. A. Mol. Biomol. Spectrosc. 56 (2000) 2693–2698.
[68] J.B. Moffat, Metal-oxygen clusters : the surface and catalytic properties of heteropolyoxometalates , Kluwer Academic/Plenum Publishers, New York , 2001.

[69] H.S. Blair, M.J. McElroy, The dyeing of secondary cellulose acetate. Investigation of the surfaces of dyed fibers by low-temperature nitrogen adsorption, J. Appl. Polym. Sci. 20 (1976) 2955–2961.
[70] R. Neumann, Polyoxometalate complexes in organic oxidation chemistry, in: K.D. Karlin (Ed.), Prog. Inorg. Chem., John Wiley & Sons, Inc., 1997: pp. 317–370.
[71] G.S. Ahmed, M. Gilbert, S. Mainprize, M. Rogerson, FTIR analysis of silane grafted high density polyethylene, (2009) 13.
[72] J. a. F. Gamelas, D.V. Evtuguin, A.P. Esculcas, Transition metal substituted polyoxometalates supported on amine-functionalized silica, Transit. Met. Chem. 32 (2007) 1061–1067.
[73] Y. Izumi, K. Urabe, M. Onaka, Recent advances in liquid-phase organic reactions using heteropolyacid and clay, Catal. Surv. Asia. 1 (1997) 17–23.
[74] R.C. Schroden, C.F. Blanford, B.J. Melde, B.J.S. Johnson, A. Stein, Direct synthesis of ordered macroporous silica materials functionalized with polyoxometalate Clusters, Chem. Mater. 13 (2001) 1074–1081.
[75] E.A. Castro, R.B. Moodie, P.J. Sansom, The kinetics of hydrolysis of methyl and phenyl isocyanates, J. Chem. Soc. Perkin Trans. 2. (1985) 737–742.
[76] L. Yao, L. Zhang, R. Wang, S. Chou, Z. Dong, A new integrated approach for dye removal from wastewater by polyoxometalate functionalized membranes, J. Hazard. Mater. 301 (2016) 462–470.
[77] S.K. Obendorf, Nanofibrous membranes for enhanced human protection, in: Greenville, SC, 2010.
[78] L. Chen, L. Bromberg, H. Schreuder-Gibson, J. Walker, T.A. Hatton, G.C. Rutledge, Chemical protection fabrics via surface oximation of electrospun polyacrylonitrile fiber mats, J. Mater. Chem. 19 (2009) 2432–2438.
[79] X. Fei, P. Gao, T. Shibamoto, G. Sun, Pesticide detoxifying functions of N-halamine fabrics, Arch. Environ. Contam. Toxicol. 51 (2006) 509–14.
[80] G. Sun, X.J. Xu, Durable and regenerable antibacterial finishing of fabrics: Biocidal Properties, Text. Chem. Color. 30 (1998) 26–30.
[81] L. Bromberg, T.A. Hatton, D. Carney, H. Schreuder-Gibson, W.R. Creasy, D. McGarvey, R.A. Fry, Degradation of nerve agents by polyacrylamidoxime and polyester fabric treated by polyacrylamidoxime as a reactive barrier, (2010).
[82] L. Qian, G. Sun, Durable and regenerable antimicrobial textiles: Chlorine transfer among halamine structures, Ind. Eng. Chem. Res. 44 (2005) 852–856.
[83] ISO 7730: Moderate thermal environments - Determination of the PMV and PPD indices and specification of the conditions for thermal comfort, ISO, 1994.
[84] H. Park, Functional aspects of clothing design, (2012).
[85] J.E. Smith, The comfort of clothing, Textiles. 15 (1986) 23–27.
[86] Y. Li, D.X.-Q. Dai, Biomechanical engineering of textiles and clothing, Woodhead Publishing, 2006.
[87] ANSI/ASHRAE Standard 55-2013, Thermal environmental conditions for human Occupancy.
[88] ISO/FDIS 7730-2005, International Standard, Ergonomics of the thermal environment.
[89] ISO 9920: 2007; Ergonomics of the thermal environment - Estimation of thermal insulation and water vapour resistance of a clothing Ensemble.

[90] M.Y. Beshir, A.S. El-Sabagh1, M.A. El-Nawawi, Time on task effect on tracking performance under heat stress, Ergonomics. 24 (1981) 95–102.
[91] F. Wang, Clothing evaporative resistance: Its measurements and application in prediction of heat strain, (2011).
[92] N.Z. Azer, P.E. Monall, H.C. Leung, Effects of heat stress on performance, Ergonomics. 15 (1972) 681–691.
[93] T. McMorris, J. Swain, M. Smith, J. Corbett, S. Delves, C. Sale, R.C. Harris, J. Potter, Heat stress, plasma concentrations of adrenaline, noradrenaline, 5-hydroxytryptamine and cortisol, mood state and cognitive performance, Int. J. Psychophysiol. 61 (2006) 204–215.
[94] J.P. Knochel, Heat stroke and related heat stress disorders, Dis.--Mon. DM. 35 (1989) 301–377.
[95] K. Parsons, Human thermal environments: The effects of hot, moderate, and cold environments on human health, Comfort and Performance, 2nd ed., Taylor & Francis, Hampshire, 2003.
[96] G. Havenith, Experimental heated, breathing and sweating manikins, (2008).
[97] J. Fan, Y.S. Chen, Measurement of clothing thermal insulation and moisture vapour resistance using a novel perspiring fabric thermal manikin, Meas. Sci. Technol. 13 (2002) 1115–1123.
[98] I. Holmer, Thermal manikins in research and standards, (1999).
[99] US Army Research Institute of Environmental Medicine (USARIEM) Thermal Manikin History. http://www.usariem.army.mil/index.cfm/about/divisions/bbmd/thermal_manikin (accessed April 6, 2016).
[100] J. Fan, X. Qian, New functions and applications of Walter, the sweating fabric manikin, Eur. J. Appl. Physiol. 92 (2004) 641–644.
[101] ASTM D1776 / D1776M - 16 Standard practice for conditioning and testing Textiles.
[102] G. Havenith, I. Holmér, K. Parsons, Personal factors in thermal comfort assessment: clothing properties and metabolic heat production, Energy Build. 34 (2002) 581–591.
[103] ASTM F2370 - 05 Standard test method for measuring the evaporative resistance of clothing using a sweating manikin.